Doctoral Dissertation

Doctoral Program in SUSTAINABLE MATERIALS, PROCESSES AND SYSTEMS FOR ENERGY TRANSITION (38th Cycle)

DM 351 digital transitions - Smart Devices for Energetic, Biomedical and Environmental Applications

Lamyea Yeasmin
* * * * * *

Supervisors

Supervisor: Prof. Barbara Ballarin
Co-Supervisor: Prof. Daniele Caretti
Coordinator: Prof. Andrea Lamberti

Politecnico di Torino
October 31, 2025

I hereby declare that, the contents and organisation of this dissertation constitute my own original work and does not compromise in any way the rights of third parties, including those relating to the security of personal data.

…….....

Lamyea Yeasmin

Bologna, October 31, 2025

Summary

The increasing socioeconomic awareness of environmental impact and sustainability in the production, use, and disposal of goods is driving the adoption of natural fibre and biodegradable composites for developing smart materials for wearable electronics across various industrial applications. In **Chapter 1** of my thesis, I present an overview of the fabrication of natural cellulose-based sensors for monitoring respiration and heart activity through polyaniline (PANI) and poly(2-acrylamido-2-methyl-1-propanesulfonic acid) (PAMPSA) doping. The chapter also introduces the development of a polyvinyl alcohol-based hydrogel supercapacitor and its potential applications in wearable electronic devices. Part of these works has already been published, and the list will be in the appendix section.

In **chapter 2**, I provide a detailed overview of the Li-O_2 battery testing conducted during my industrial research period at *Bettery.srl*. The chapter discusses the preparation methods for both cathode and membrane materials. Additionally, it describes the design and implementation of a customized experimental setup specifically developed for efficient and accurate Li-O_2 battery performance testing.

In **chapter 3**, I present a detailed study on the development of a bio-based sustainable electrolyte for lithium-ion capacitors. This work has been carried out during my research period abroad at *Friedrich Schiller University Jena, Germany.* The section covers the preparation and formulation of the electrolyte, emphasizing

the use of environmentally friendly and renewable materials. Furthermore, it discusses the physicochemical characterization of the electrolyte to evaluate its structural and thermal properties. The chapter also describes the cell assembly process and provides a comprehensive analysis of the electrochemical performance, highlighting the electrolyte's potential for enhancing the sustainability and efficiency of energy storage systems.

Acknowledgment

At the end of my PhD journey, I would like to thank those without whom this journey wouldn't have been successful. Fortunately, I have many people to thank who act as steps of my career ladder.

First of all, I would like to thank **Politecnico di Torino, PNRR** doctoral program in sustainable materials, processes, and systems for energy transition (38^{th} Cycle), and **DM 351** digital transitions - smart devices for energetic, biomedical, and environmental applications fellowship program, and our PhD coordinator **Prof. Andrea Lamberti** for giving me the opportunity to pursue PhD.

I would also like to thank my host university, **Università degli Studi di Bologna,** where I spent most of my time during these three years. I am grateful to my PhD supervisor, **Prof. Barbara Ballarin,** for her constant support, motivation, and travel ideas. I would also like to thank my PhD co-supervisor, **Prof. Daniele Caretti**. I am grateful to **Prof. Maria Cristina Cassani** for her critical research insights and for introducing me to delicious Italian cuisine. I am grateful to my friend and colleague, **Valentina,** for comforting and supporting me; without her, life would have been more difficult in this new country and environment.

I am grateful to **Prof. Francesca Soavi** and **Dr. Alessandro Brilloni** for accepting me as a research intern at their company **Bettery.srl** and allowing me to work with brilliant people and learning more about electrochemistry. I would like

to thank all my colleagues there, especially my friend **Francesco,** for *cornetto al cioccolato*.

I am grateful to **Prof. Andrea Balducci** for giving me the opportunity to spend six months at **Friedrich Schiller University of Jena** and work in his amazing research group. My special thanks to my mentor, **Juan Luis Gómez Urbano,** for teaching and guiding me and sharing his knowledge. It was always fun to work with him. *Juanlu, you're the best, and I'm waiting for the Tapas party*. I would also like to thank my friend and colleague **Bartek**, **Akshaya**, **Urooj** for making me feel at home. Thank you, **Khai** for having the solution of all my kind of problems and delicious cakes. I'm sorry for the manes I missed to write here. Thank you everyone.

I would also like to thank my professor from my master's degree, **Prof. Nikhil Ranjan Jana,** and my teacher **Jagabondhu Nayek** for their constant support and motivation both in personal and professional life.

Thanks to my parents and sisters, **Raisa** and **Sariya,** for making me who I am and always supporting me from the far. Thanks to all my friends, whom I met at different time and remain with me. Thanks to **Sourjya**, **Soham**, **Dibyendu**, **Bipasha**, **Soumendu**, **Tista**, **Sohini**, **Sikta**, **Sayantan**, **Deep**, **Koushik**. I am also grateful to **Kanka.** *Thank you for having my back at my worst. I am, because we are.* ^^

Table of contents

Chapter 1: Preparation and electrochemical characterization of cellulose and polymer hydrogel based flexible devices

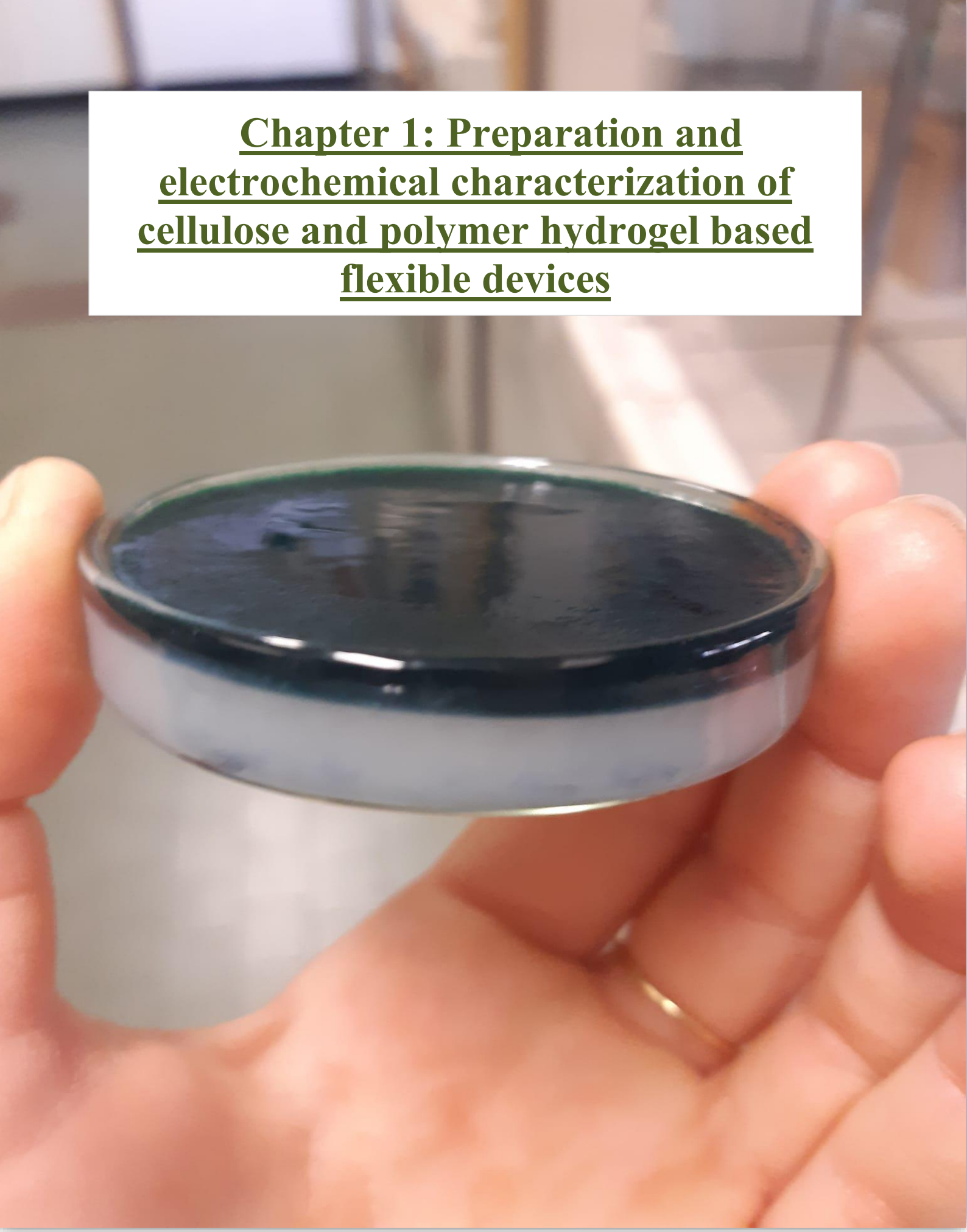

Index

1.1. Introduction

The increasing emphasis on sustainable, biocompatible, and biodegradable materials for electronic applications has driven significant interest in the search for new materials such as cellulose and polymer-based composites.

Cellulose is the most abundant biopolymer on Earth, offering excellent mechanical strength, flexibility, and renewability, and that makes it an attractive substrate for the development of eco-friendly electronic devices.

On the other hand, polyvinyl alcohol (PVA) is biodegradable under certain natural conditions and is cheap. That makes it useful material for device fabrication. The integration of conducting polymers into cellulose and PVA matrices has opened new possibilities for the fabrication of paper-based and hydrogel-based electronics, including sensors, actuators, and wearable devices. Among conducting polymers, polyaniline (PANI) stands out for its unique doping/de-doping behavior, redox versatility, environmental stability, and ease of synthesis. However, traditional acid-doped PANI composites often suffer from limited mechanical strength, poor flexibility, and biocompatibility concerns, largely due to acid leaching over time.

A promising approach to overcome these limitations involves doping PANI with polymeric acids, such as poly(2-acrylamido-2-methyl-1-propanesulfonic acid) (PAMPSA). PAMPSA not only stabilizes PANI's conductive state and heat stability but also introduces additional hydrogen bonding and flexibility, enhancing the mechanical and functional properties of the resulting composites.

This chapter focuses on the synthesis, characterization, and application of a novel composite material: the first based on cellulose doped with PANI-PAMPSA polymer (Cell/PANI-PAMPSA), prepared by in-situ polymerization of aniline in the presence of PAMPSA and cellulose fibers, and the second based on PVA-hydrogels doped with PANI-PAMPSA (PVA/PANI-PAMPSA), prepared by physical crosslinking. The morphological, mechanical, thermal, and electrical properties of the composite have been deeply investigated. Moreover, the applicability of these composites in the fabrication of eco-friendly humidity sensors and biomedical devices has been studied. Finally, the possible application of this system to prepare wearable and disposable diagnostic platforms represents

a significant advancement in the development of sustainable, cost-effective paper-based electronics.

1.2. State-of-the-art of conductive polymers

Conductive polymers (CPs) are a class of organic molecules with particular electrical properties that find a wide range of applications in batteries, supercapacitors, electrochromic devices, solar cells, sensors, and biomedical applications[1-3]. The first study of CPs was reported by Letherby in 1862 with the electrochemical preparation and characterization of polyaniline formed by the oxidation of aniline on a platinum electrode in diluted sulfuric acid. CPs did not receive much interest until the end of 1970, when Shirakawa, together with MacDiarmid and Heeger discovered that the polyacetylene (structure shown in **Scheme 1.1**) can be made conductive after exposing it to the oxidizing agents like chlorine, bromine, or iodine which made polyacetylene 10^9 times more conductive than the pristine polyacetylene for which they were awarded Nobel Prize in 2000[4]. This breakthrough gave rise to the development of new kinds of materials combining the properties of polymers and electrical conductivity. Unlike plastic, conducting polymers have alternating single and double bonds with sp^2 hybridized structure in conjugated sequence along the chain backbone of the polymer, which acquires delocalization of π-electrons and consequently leads to electrical conduction.

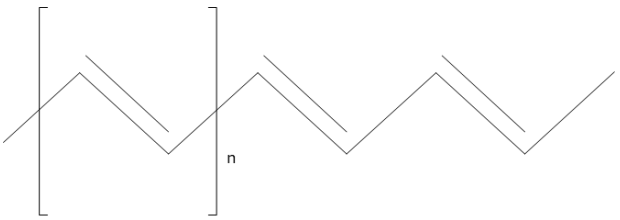

Scheme 1.1: Chemical structure of polyacetylene

Various CPs were studied, such as polypyrrole (PPy), polyazulene, polyfluorene, polythiophene, polyterthiophene, and polyaminonaphthalenes[5].

The CP investigated in this work is Polyaniline (PANI), which has the chemical structure presented in **Scheme 1.2**, where $0 \leq y \leq 1$.

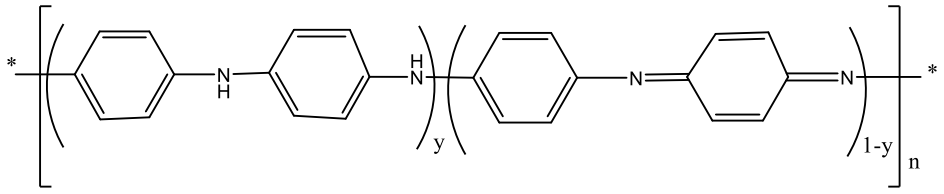

Scheme 1.2: Chemical structure of polyaniline

Depending on the value of y, polyaniline could have different states of oxidation: if $y = 0$, polyaniline is in the fully oxidized state and called *pernigraniline* base, if $y = 1$, polyaniline is in the fully-reduced state called *leucoemeraldine*, and half-oxidized state is gained when $y = 0.5$ and called emeraldine base. By doing the *pernigraniline* and emeraldine bases, the respective salts can be obtained[6-8]. A schematic representation is given in **Scheme 1.3**.

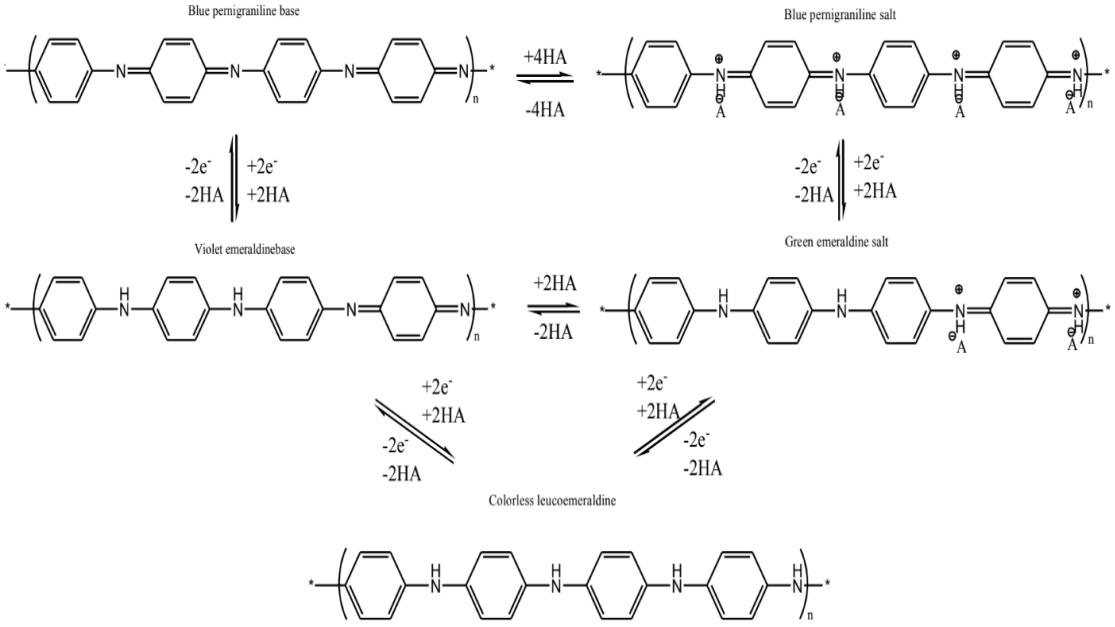

Scheme 1.3: Different states of oxidation of polyaniline

Leucoemeraldine is a colorless form of polyaniline. It is not conductive but can slowly oxidize in air. *Pernigraniline* form is composed of aminobenzene and quinonediimine fragments that rapidly decompose in water and air due to the presence of nucleophiles. *Emeraldine salt* is the most interesting form of PANI because it shows electrical conductivity. It is formed by protonation of the emeraldine base with organic and inorganic acids. This process is conventionally

called *doping* and results in the formation of polycations due to the interaction between protons and imine atoms of nitrogen. Accordingly, electrons undergo redistributions over a certain conjugation length, providing the electrical conductivity of the polymer[9]. Cation radicals in PANI could also be delocalized by an intramolecular mechanism. The so-called π stacking is based on the Van der Waals interactions between benzene and quinoid rings of different chains of PANI oriented in one direction. The electron conductivity of such a structured polyaniline is reported to be about 10^3 S cm^{-1} [10]. Structure, morphology, and oxidation state of polyaniline can be tailored by varying the synthesis conditions in an electrochemical or chemical route.

The *electrochemical polymerization* of aniline is normally conducted on the surface of a conductive working electrode, usually in aqueous solution containing acids. Different methods can be used: i) potentiostatic with a fixed potential around 0.7 – 1.2 V *vs* calomelan reference electrode (SCE); ii) potentiodinamic, varying the potential from -0.2 to 1.2 V *vs* SCE or iii) galvanostatic, with a fixed current density of about 10 mA cm^{-2}. This type of polymerization leads to the formation of PANI with controlled morphology and high purity[11,12]. A schematic representation of the electrochemical polymerization mechanism is given in **Scheme 1.4.**

Aniline anodic oxidation:

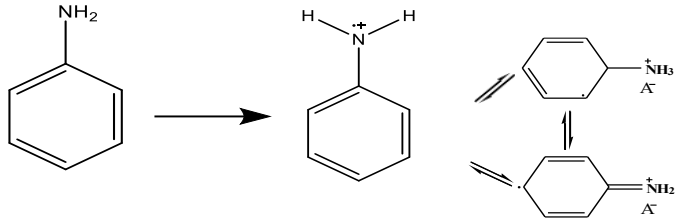

Coupling of radicals:

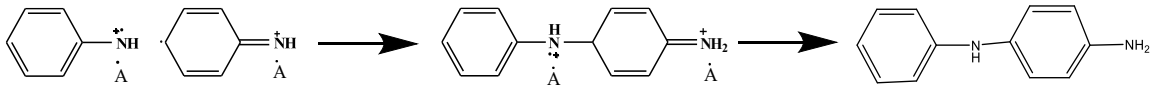

Polyaniline propagation:

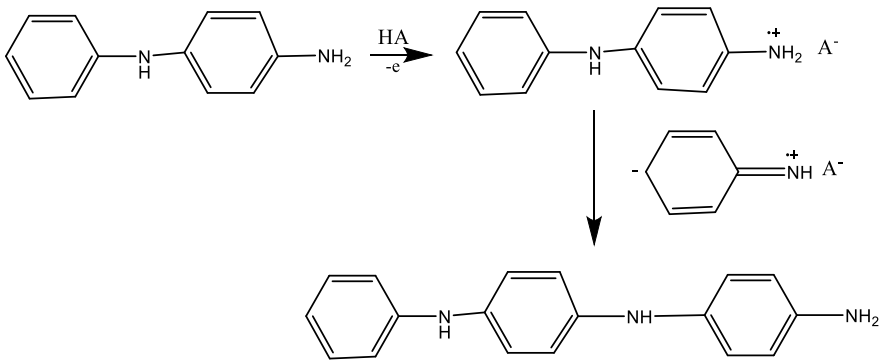

Polyaniline oxidation and doping:

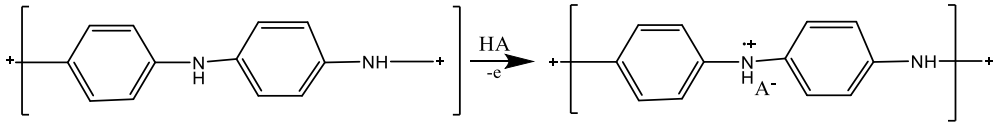

Scheme 1.4: Electrochemical polymerization mechanism of aniline.

The *chemical polymerization* of aniline is possible in the presence of an oxidant, commonly ammonium persulfate (**Scheme 1.5**). Polymerization is conducted in an acidic solution at 1 < pH < 3 to have the emeraldine salt form. Using that method, PANI results in the highest yield (more than 90%) and a conductivity of about 1.2 S cm^{-1} [13]. With this synthesis, a conductive substrate is not needed[14,15].

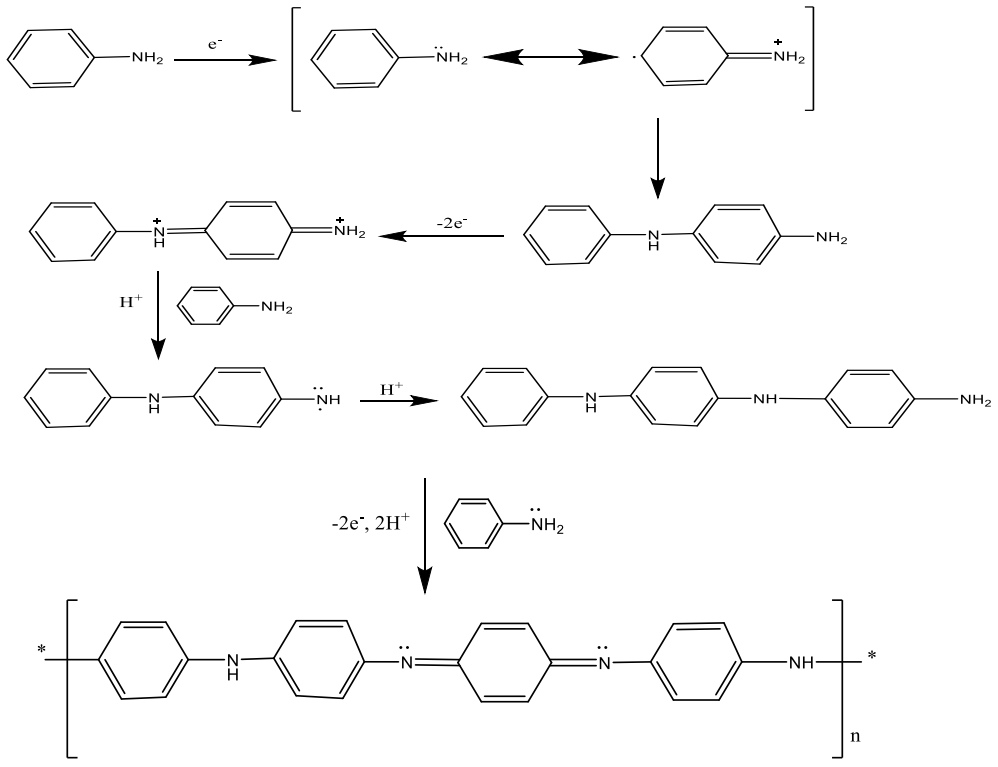

Scheme 1.5: Mechanism of chemical polymerization of aniline

Among the conducting polymers, PANI is known for having probably the best combination of stability, conductivity, and low cost[8]. Despite having versatile use in large-scale industrial applications, many of the potential uses of PANI still need to be explored. One of the major drawbacks of PANI is the lack of its processability, its conductivity is unstable at neutral pH, and its insolubility in water. The most promising approach to overcoming these problems is the formation of a composite using nonconducting polymers as a matrix. Adding water-soluble polymers, for example, hydrogen bonds could be formed, improving not only water dispersibility, but also thermal stability[16]. Polymerization with these template materials is performed, for example, in the presence of strong polyacids, such as poly(4-styrenesulfonic acid) and poly(2-acrylamido-2-methyl-1-propanesulfonic acid), as well as weak polyacids, such as poly(vinylphosphonic acid) and poly(acrylic acid), which stabilize the oxidized state even in less acidic conditions[17].

1.3. Application of conducting polymers as electrochemical sensors

An electrochemical sensor is a material that is able to convert chemical reactions that a target species makes on its surface into an electrical signal that exhibits changes in current, potential, and conductivity. Thus, depending on the type of response, sensors can be divided into voltametric/amperometric, potentiometric, or impedimetric categories[18].

Voltametric/amperometric sensors, in a typical three-electrode cell, measure the current while a potential is applied between the working and the counter electrode. The response is the result of electrochemical reactions that occur on the surface of the electrode and the interface between the electrode and electrolyte. The mass transport of active species on the surface is the rate-determining step in this case[19]. Voltametric methods include linear sweep

voltammetry, cyclic voltammetry, hydrodynamic voltammetry, differential pulse voltammetry, square-wave voltammetry, polarography, and stripping voltammetry[20]. The only difference between voltametric and amperometric sensors is that the second one lacks a potential sweep, instead of using a potential step. The resulting current at a given potential is proportional to the concentration of the electroactive species in the sample, and the current is given by Cottrell's equation[21]:

$$i = \frac{\mathrm{nFAc}_j^0\sqrt{D_j}}{\sqrt{\pi t}} \qquad \text{equation (1.1)}$$

Where i is the current (A), n is the number of electrons to reduce or oxidize one molecule of analyte j, F is the Faraday constant (96485 C/mol), A is the electrode's area in cm^2, c^o is the initial concentration of analyte in mol cm^{-3}, t is the time in s and D_j is the diffusion coefficient for the analyte j in $cm^2\ s^{-1}$. Amperometric sensors are more sensitive and selective because the oxidation or reduction potential used for detection is characteristic of the analyte species[22].

Potentiometric sensors measure the potential difference between the working electrode and the reference electrode when no significant current is flowing. The potential difference is given by the Nerst equation:

$$E_{cell} = E_{cell}^0 - \frac{RT}{nF}\ln Q_r \qquad \text{equation (1.2)}$$

Where E_{cell} is the observed cell potential at zero current, E^0 is the standard potential of the cell, R is the universal gas constant (8,314 J K^{-1} mol^{-1}), T is the temperature in K, z is the number of electrons transferred in the cell reaction, F is the Faraday constant and Q_r is the reaction quotient of the cell in terms of activities of the oxidized and reduced species.

The lowest detection limits of potentiometric devices are currently often realized with ion-selective electrodes (ISE)[23].

Impedimetric sensors are based on surface changes caused by the adsorption

and desorption of target species that cause a modification of the conductivity of the material. The experimental approach is to perturb the cell with a small magnitude alternating potential and to observe the way in which the system reacts to the perturbation in the steady state[24].

In any case, electrochemical methods allow very low detection limits, high selectivity, and a small active area, and consequently a very small volume of analytes. In this framework, polyaniline is widely studied as a material for electrochemical sensors because of its high sensitivity and selectivity to a large number of target molecules, thanks to its easiness to be tailored. For example, a glucose-sensor made of PANI and $NiCo_2O_4$ is reported[25]. The catalytically active sites in $NiCo_2O_4$ with conductive PANI played a synergetic role in the oxidation of glucose and exhibited good sensitivity and a lower detection limit. Moreover, a surface with PANI deposited upon it is used for the sensitive detection of nucleic acids. Gene sensing is a very powerful tool for the diagnosis of a wide variety of diseases, from common viral infections to cardiovascular diseases and cancer. For this purpose, a new method was developed for the sensitive detection of nucleic acids using it. In this case, the polymer was deposited by enzyme-catalyzed formation and template-guided deposition in which a reporter enzyme catalyzed the deposition of PANI onto the analyzed nucleic acid molecules by forming an intramolecular complex[21,22].

1.4. State-of-the-art of conducting cellulose

Cellulose-based materials are valuable owing to their chemical uniqueness, shape flexibility, ease of processing, mechanical strength, and biodegradability[26,27]. Cellulose is found in many plants and is also biosynthesized by certain microorganisms, like the Acetobacter xylinum. In addition, via a simple carbonization process, cellulose can be transformed into electronically conductive carbon materials with high specific surface areas and rich pore structures. These characteristics make cellulose-based materials suitable for use as flexible/transparent substrates, separators, electronic–ionic conductors, electrolytes, and electrochemical electrode materials in flexible circuits or sensors,

conductive transistors, organic light-emitting diodes (OLEDs), organic thin-film transistors (OTFTs), supercapacitors, batteries, triboelectric nanogenerators (TENGs), tissue bioelectronics, and other flexible electronics. At present, different substrates are used for sensors, such as polyimide (PI), polydimethylsiloxane (PDMS), polyester (PE), and polyethylene terephthalate (PET). Despite their excellent flexibility and stability, they are difficult to degrade, resulting in electronic pollutants and that is why paper as substrate represents a valid alternative[27].

The evolution and development of cellulose-based materials, as shown in **Fig. 1.1**, demonstrate their potential for use in emerging sustainable, flexible, and portable intelligent electronics.

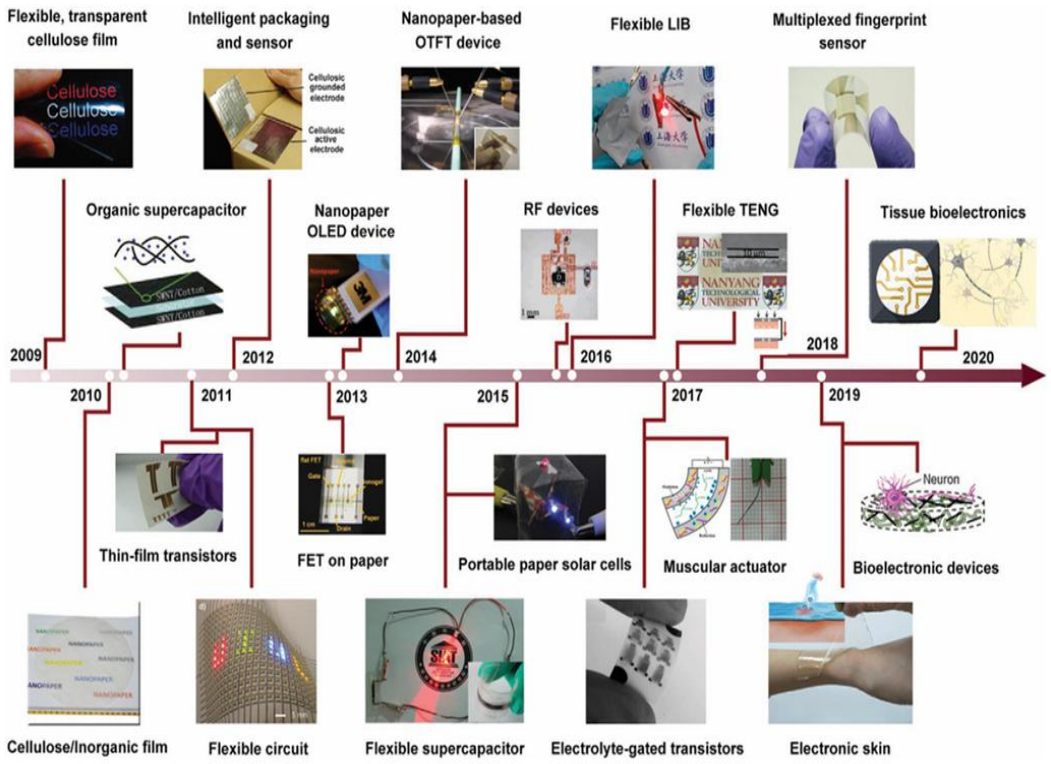

Fig. 1.1: Timeline of cellulosic materials[25]

Cellulose consists of linear β-1,4-linked D-glucose units, and has abundant hydroxyl (–OH) active groups that can form inter- and intramolecular bonds between polymeric chains, resulting in strong hydrogen-bond networks (**Fig. 1.2**).

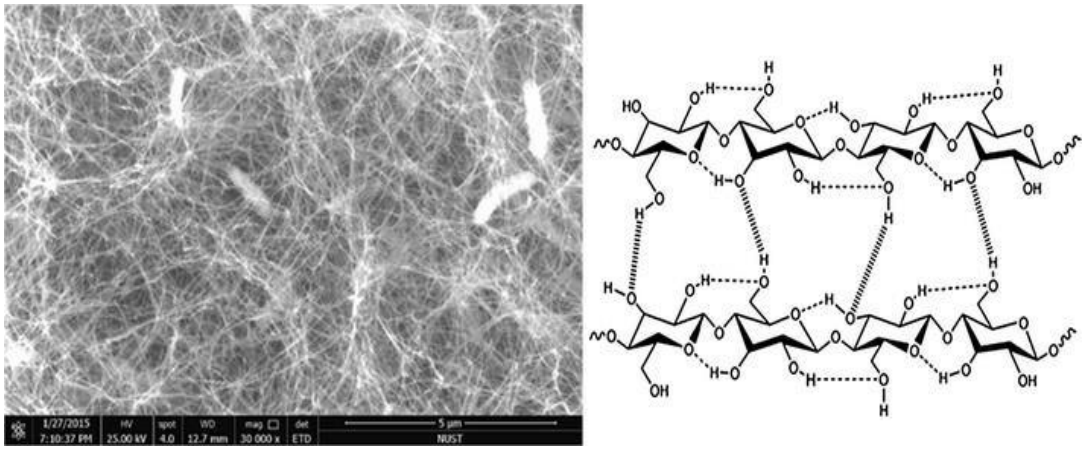

Fig. 1.2: SEM image and scheme of cellulosic network[31]

Purified cellulose can be obtained by removing lignin and hemicellulose from plants via chemical pretreatments[29,30]. Within these cellulose fibers, there are regions where the macromolecular chains are arranged in a highly ordered (crystalline) structure, and regions where the chains are messy and disordered (**Fig. 1.3**). The structure and distribution of these crystalline and disordered domains depend on the raw materials and pretreatment methods. Cellulose can be processed to obtain various morphologies. Cellulose nanofibers (CNFs), for example, exhibit a web-entangled morphology and a high specific modulus, which are obtained through mechanical nanofibrillation methods such as high-pressure homogenization, high-intensity ultrasonication, high-speed stirring, or ultrafine grinding. In contrast, cellulose nanocrystals (CNCs) are obtained by acid hydrolysis of disordered and polycrystalline regions of cellulose[31,32].

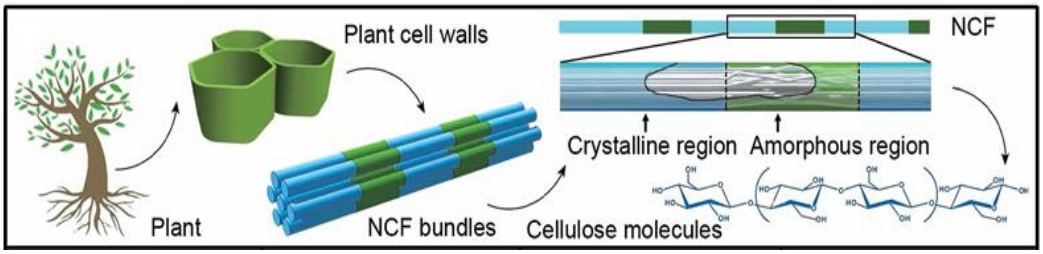

Fig. 1.3: Crystalline and disordered macromolecular structure of cellulose[32]

Flexible sensing devices have received tremendous attention because of their valuable applications in human health monitoring, human-machine interaction, and wearable devices. Unlike synthetic polymers, cellulose materials are biocompatible and renewable, which increases the recyclability of wearable sensors[33]. Functional inorganic and organic materials such as metal oxides, carbon materials, and conductive polymers can be incorporated into cellulose-based materials to develop conductive electrodes and dielectric layers for the fabrication of flexible sensors[34,35]. For example, regenerated cellulose was combined with poly(3,4-ethylene dioxythiophene)–poly(styrene-sulfonate) (PEDOT:PSS) to protect silver nanowires (AgNWs) from oxidizing and falling. Subsequently, a flexible and conductivity-stable hybrid film was fabricated. The synergy of coordination complexation and hydrogen bonding of cellulose and PEDOT:PSS significantly improved the robustness of the interfaces and the structural stability of the hybrid film. The hybrid film had stable conductivity, even when subjected to severe conditions (90% relative ambient humidity and 65 °C for 60 days) and repeated bending and peeling tests. This hybrid film was used to construct a strain-to-electricity sensor that showed excellent flexibility and biocompatibility. The sensor had a high sensitivity of 23.35 kPa^{-1} and could detect different mechanical strains, including pressing, touching, bending, and even breathing airflow[35]. For the fabrication of complicated “bottom-up” nanostructures, CNFs possess distinct advantages, making them ideal electrode components for piezoresistive sensors. Guo’s group assembled a conductive CNF/AgNWs-coated polyurethane (CA@PU) sponge using a dip-coating process. The application of CNFs helped to disperse the AgNWs and provided strong adhesion between the layers. The CA@PU sponge-based sensor exhibited a high piezoresistive effect and could record slight sounds and detect when an object was placed onto its surface[36].

Cellulose-based carbon materials have also been explored for constructing strain sensors. CNF/Ti3C2 MXene hybrid aerogels and their corresponding sintered carbon aerogels exhibited high structural stability and could undergo a high strain of 99% for more than 100 cycles. As sensors, these carbon aerogels showed high sensitivity and very low detection limits for small pressures and strains. Due to the

scalable piezoelectric responses of cellulose, self-standing CNF films can be used as functional sensing layers in piezoelectric sensors, with a high piezoelectric sensitivity of up to 6.4 pC N^{-1} in ambient conditions. This is comparable to that of commercial poly(vinylidene fluoride) (PVDF) piezoelectric polymer sensors. The capacitive sensing of metallized cellulose-based materials provides a low-cost solution for integrating electronic interfaces into "smart" packaging[37]. For example, Whitesides' group developed a paper-based intelligent packaging device that integrated sensing and alarm functions to ensure seal integrity and prevent theft from containers[38].

Finally, a PANI nanorod-based gas sensor via in-situ co-doped with 5-sulfosalicylic acid (SSA) on a 3D interconnected cellulose network substrate was presented as an ammonia sensor with a high response (21.3 for 50 ppm ammonia) and quick response/recovery time (4.1 s/16 s). Furthermore, the sensor also demonstrates excellent ammonia selectivity among different interfering agents, with a lower detection limit (LOD) of 10 ppb at room temperature, and the limit sensing temperature is even below -10 °C[39].

1.5. State-of-the-art of conducting hydrogel

The increasing advancement of wearable electronics and flexible sensors is causing an increasing demand for electrochemical energy storage systems that are not only compact and efficient but also flexible, safe, and biocompatible[40]. Among the various storage solutions, hydrogel-based materials have recently emerged as promising candidates, particularly in the sector of electrochemical sensors[41] and in the energetic field[42,43]. These systems present a unique integration of electrochemical performance with mechanical flexibility, thus offering transformative potential for future applications in wearable health monitoring, soft robotics, and environmental sensing devices[44]. This paragraph provides a comprehensive overview of the state-of-the-art research, specifically focusing on hydrogel-based materials used as supercapacitors of flexible sensors (**Fig. 1.4**).

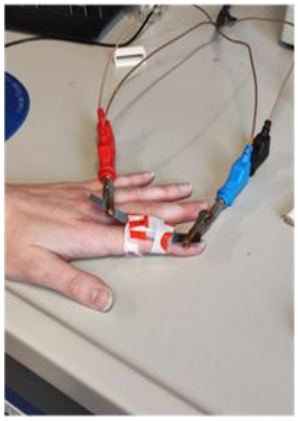

Fig. 1.4: Polymer hydrogel as finger bending sensor[45]

Hydrogel-based materials (Hy) are composed of three-dimensionally cross-linked polymer networks that can trap large quantities of water or ionic solutions, providing ionic conductivity while the material is soft, flexible, and deformable structured[46]. Their structure mimics biological tissues, making them inherently suitable for biointegrated sensors. Moreover, their capacity to accommodate large deformations such as bending, twisting, and stretching without compromising electrochemical functionality distinguishes them from conventional rigid devices[47]. These characteristics are especially critical for electrochemical sensors that must maintain signal integrity while subjected to motion and stress in wearable environments.

Moreover, a crucial advantage of hydrogels in supercapacitor design is their tunable compositions. Hydrogels can be derived from both natural (e.g., polysaccharides, gelatin etc.) and synthetic polymers (e.g., polyvinyl alcohol [PVA], polyacrylamide etc.)[48]. Natural hydrogels offer biocompatibility and biodegradability, but can suffer from limited mechanical strength and variability. Synthetic hydrogels, on the other hand, provide better control over mechanical, chemical, and electrochemical properties, essential for tailoring the performance of energy storage systems and sensors alike. PVA-based hydrogels have attracted significant interest due to their high hydrophilicity, ease of processing, biocompatibility, and possibility of being prepared with a physically cross-linked method via freeze-thaw (F/T) cycles (**Fig. 1.5**). This method eliminates the need for toxic chemical cross-linkers, facilitating the development of non-toxic and

environmentally friendly energy storage materials[49,50].

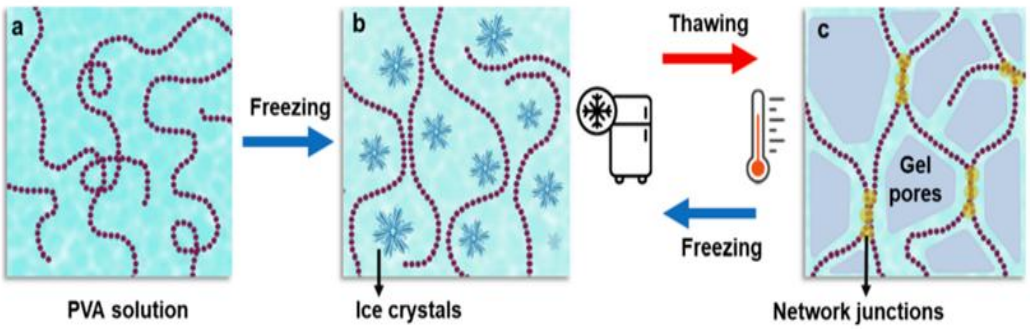

Fig. 1.5: PVA-based hydrogel obtained with a physical crosslinking method through freeze-though cycles.

To enhance the electrical performance of hydrogel-based materials, a hybrid conductivity mechanism can be adopted. For example, the ionic conductivity can be improved through the incorporation of electrolytes such as sulfuric acid (H_2SO_4) or KCl, whereas the electronic conductivity is imparted, for example, by embedding conductive nanofillers or polymers[51,52].

The possibility of modulating this dual-conductivity structure allows the hydrogel to serve both as an electrolyte and an electrode material, consenting the preparation of systems obtained with the same material but with different properties, which is very important, especially in the energy sector.

In this contest, PVA-hydrogels were prepared using a direct acid doping method (H_2SO_4), via a physically crosslinked method, varying PVA molecular weight and composition[53], and their mechanical and electrochemical performances were systematically evaluated. The PVA hydrogels exhibited enhanced tensile strength, high ionic conductivity, and excellent flexibility, making them suitable for wearable supercapacitors and sensing devices applications[54].

The incorporation of polyaniline (PANI) stabilized with poly(2-acrylamido-2-methyl-1-propane sulfonic acid) (PAMPSA) into the PVA-hydrogel was then investigated to increase the conductivity (PVA-PANI_PAMPSA hy). The resulting materials, PVA-hy and PVA-PANI_PAMPSA-hy, were then auto-

assembled via the freeze-thaw method, forming a pseudo-capacitive system with improved electronic conductivity, electrochemical activity, and mechanical compliance. This composite not only maintained the self-healing and stretchable properties of the base hydrogel but also demonstrated electrochromic and redox sensing capabilities, suggesting its dual role as an energy storage material and a real-time electrochemical sensor[55,56].

The fabricated all-in-one symmetric hydrogel supercapacitor (HySC), constructed from layered configurations of PVA-hy (electrolyte) and PVA/PANI_PAMPSA-hy (electrode), exemplified a self-standing, flexible structure. This design eliminates the need for separate electrodes, separators, and liquid electrolytes, greatly simplifying the device architecture while reducing the risk of leakage and toxicity associated with traditional aqueous or organic electrolytes (**Fig. 1.6).** In practical tests, the HySCs showed high capacitance retention after multiple deformation cycles, highlighting their mechanical resilience and potential longevity in wearable or implantable environments.

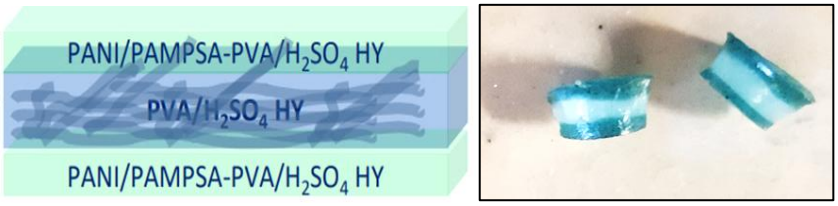

Fig. 1.6: Schematic (left) and visual (right) presentation of an All-in-one symmetric hydrogel supercapacitor[53]

Moreover, from a sensing perspective, hydrogel-based materials are ideal platforms for detecting various physical (e.g., pressure, strain etc.), chemical (e.g., pH, glucose, ions etc.), and biochemical (e.g., sweat, enzymes etc.) stimuli[57]. Their high surface area, porous network, and electrolyte-filled matrix provide a conducive environment for rapid analyte diffusion and electrochemical interaction. When combined with functional nanomaterials or bio-recognition elements, hydrogel-based materials can operate as both power sources and sensor units, enabling compact self-powered sensing platforms[58]. Moreover, their ability to respond to environmental changes via changes in capacitance, resistance, or redox current allows for real-time signal transduction in physiological settings.

Despite recent progress, several challenges remain in optimizing hydrogel-based materials for sensor applications. Achieving simultaneously high mechanical stretchability with efficient ionic/electronic conductivity, and long-term stability remains a complex material design task. Furthermore, interfacing hydrogel-based sensors with electronic circuitry while maintaining flexibility and minimizing signal noise is a critical field yet to be researched further. Long-term durability under continuous wear and exposure to biological fluids must also be addressed through surface engineering or encapsulation strategies. Nevertheless, the modular nature of hydrogel design, enabling control over crosslinking, filler distribution, and functionalization, offers an adaptable platform for future innovation[59,60].

In conclusion, hydrogel-based materials are rapidly evolving into multifunctional components for next-generation electrochemical sensors or energetic applications. Through the intelligent combination of materials like PVA and PANI, and the adoption of physical fabrication techniques such as freeze–thaw crosslinking, researchers are creating devices that not only store energy but also interact intelligently with their environment. The integration of sensing and energy storage functions within a single hydrogel platform marks a significant advancement toward sustainable, safe, and smart wearable systems. As the field progresses, further work is expected to focus on enhancing multifunctionality, developing bio-integrated interfaces, and achieving scalable fabrication strategies. With continued innovation, hydrogel supercapacitors stand at the forefront of wearable electrochemical sensor technology, bridging the gap between soft materials and smart devices[61].

1.6. Synthesis and preparation of materials

1.6.1. Synthesis of cellulose/polyaniline-poly (2-acrylamido-2-methyl-1-propanesulfonic acid) (Cell/PANI_PAMPSA)

In a 1.0 L round-bottom flask, 2.5 g of bare cellulose fibers were dispersed in demineralized water (300 mL) for 30 min, then 2.54 mL of aniline and 58.0 g of PAMPSA were added to the fiber suspension and stirred for 1 hour at room temperature[62]. 5.8 g of APS was dissolved in 25 mL of distilled water, with a fixed aniline to APS molar ratio of 1:1[63]. The APS solution was slowly added

dropwise to the stirred suspension containing aniline, PAMSA, and cellulose. The flask was kept at 0 °C in an ice bath for 6 h. After 24 h, the coated fibers were filtered in a Buchner funnel and washed several times with 1.0 M citric acid solution. The conductive fibers (Cell/PANI-PAMPSA) were dried in an air atmosphere for 24 h. To obtain a 0.20 mm thickness sheet, 5.0 g of conductive fibers were added to 1.0 L of demineralized water and stirred for 5 min, and then the fibers were partially dried in a square sieve (21.0 cm ×14.8 cm size, typical A5 paper format). Finally, the sheet was pressed at 50 bar pressures (P50 AXA manual hydraulic press) for 10 s. The thickness of the sheet is different and can be varied by changing the amount of modified cellulose that is used (i.e., 10 g for 0.40 mm, etc.). For comparison, Cell/PANI sheets were prepared in the same way[64].

1.6.2. Preparation of single-layer PVA hydrogel

Commercial PVA powders of different molecular weights (**Table 1.1**) were purchased from Merck KGaA, Darmstadt, Germany; 1.0 M H_2SO_4 solution was prepared from the dilution of 95−98% H_2SO_4 (Sigma-Aldrich).

PVA	Molecular Weight	Degree of Hydrolysis	Hydrogel Obtained
A-PVA	13,000-23,000	98.0-98.8 %	HyA
B-PVA	31,000-50,000	98.0-98.8 %	HyB
C-PVA	146,000-186,000	> 99 %	HyC
D-PVA	89,000-90,000	> 99 %	HyD

Table 1.1: PVA employed

A typical hydrogel preparation via the freezing-thawing method is reported[64,65]. 2.6g of PVA powder was added to 15 mL of aqueous 1.0 M H_2SO_4 solution (PVA/H_2SO_4 weight ratio equal to1/5.8) and heated in a water bath at 70-90 °C under vigorous stirring to obtain a transparent solution. The time for dissolution and temperature strictly depended on the polymer molecular weight (MW). The solution was then ultrasonically treated to remove bubbles and poured into a Petri

dish (8 cm in diameter). The Petri dish was placed inside the refrigerator at -18 °C for 3 hours and then was kept at room temperature to thaw the hydrogel for 1 hour (one freeze-thaw cycle). After three freeze-thaw cycles, the PVA-hydrogel was obtained (**Fig. 1.7**). This procedure was changed appropriately (PVA/H_2SO_4 weight ratio) depending on the PVA molecular weight used (**Table 1.2**).

Hydrogel sample	PVA molecular weight	PVA/H_2SO_4 ratio (w/w)	% of PVA	Hydrogel formation
HyA#1	13,000-23,000	1/5.8	17	no
HyB#1	31,000-50,000	1/5.8	17	yes
HyC#1	146,000-186,000	1/5.8	17	No
HyA#2	13,000-23,000	1/3	33	Yes
HyB#2	31,000-50,000	1/3	33	Yes
HyC#2	146,000-186,000	1/10	9	yes
HyD#1	31,000-50,000	1/4	25	yes
HyD#2	89,000-90,000	1/4	9	yes

Table 1.2: Properties of obtained hydrogels

Samples HyA#1, HyB#1, and HyC#1 were prepared starting from PVAs of different molecular weights (A-PVA, B-PVA, and C-PVA) using a fixed PVA/H_2SO_4 weight ratio of 1/5.80. In acidic solution, A-PVA and B-PVA dissolved to form clear solutions within 10-15 min, whereas C-PVA agglomerated, producing a gelatinous, sticky suspension with residual solids. After three freeze-thaw cycles, a whitish, opaque PVA-hydrogel was obtained only from B-PVA (HyB#1). For C-PVA, hydrogel formation (HyC#2) was achieved only by lowering the PVA/H_2SO_4 ratio to 1/10, while for low- and medium-molecular weight PVA (HyA#2 and HyB#2), a ratio of 1/3 was sufficient[45].

HyB#1 and HyB#2, prepared from PVA of the same MW but different PVA/H_2SO_4 ratios, formed hydrogels with no phase separation and a denser, more compact structure. Conversely, HyA#2 and HyB#2 shared the same PVA/H_2SO_4 ratio but differed in molecular weight. HyD#1 and HyD#2 were prepared as optimized hydrogels for semi-cell (S_1 and S_2) and full-cell (**Hy_1SC and Hy_2SC)**

semiconductor preparation and will be discussed in Paragraph **1.7.3.**

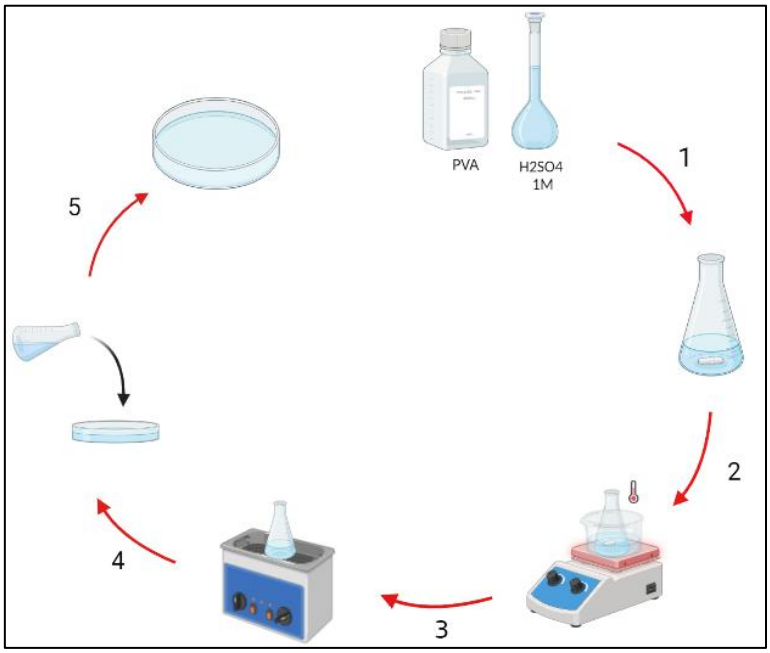

Fig. 1.7: Main stages of preparation of PVA-based hydrogels in 1 M H_2SO_4

1.6.3. Synthesis of PANI_PAMPSA

PAMPSA (5.8 g, 0.028 mol) was dissolved in 375 mL of deionized water. Aniline monomer (2.6 g, 0.028 mol), at a 1:1 monomer-to-acid molar ratio, was then added to the PAMPSA solution and stirred at room temperature for 1 h. The oxidizing agent, ammonium peroxydisulfate (5.8 g, 0.025 mol), at a 1:0.9 monomer-to-oxidizing-agent molar ratio, was dissolved separately in 25 mL of deionized water. Both solutions were sparged with nitrogen for 30 min. The PAMPSA-aniline solution was then cooled in an ice–water bath before the ammonium peroxydisulfate solution was added dropwise at approximately 1.25 mL min^{-1}. The reaction medium was maintained at ice-water temperature for the first 6 h and was vigorously stirred throughout the polymerization. The reaction was allowed to proceed overnight to ensure complete conversion.

Before the addition of ammonium peroxydisulfate, the PAMPSA-aniline solution was colorless. Upon addition, the solution turned yellow, then gradually changed to brown and blue over time. Finally, the polymerization medium turned green. This final color change indicates the formation of the conductive emeraldine salts of PANI_PAMPSA. After 24 hours, the resulting material was a polymer complex

of PANI and PAMPSA that is ionically associated.

1.6.4. Preparation of all-in-one PVA hydrogel-based supercapacitor (HySC)

The layer of PVA-PANI_PAMPSA hydrogel (HyPVA-PANI_PAMPSA) was prepared from a pre-synthesized PANI_PAMPSA polymeric suspension obtained via an oxidative polymerization process[65,66,67] and from PVA. PVA with two different molecular weights was used in this case: the 31,000-50,000 and 89,000-98,000, respectively. Briefly, 1.3 g of PVA was dissolved in 7.6 mL of 1.0 M H_2SO_4 solution at 80° C under stirring at 350 rpm (solution A). Then, 1.3 g of PANI_PAMPSA suspension (3.5% w/w PANI_PAMPSA) was added to solution A after turning off the heating, and kept under vigorous stirring until a homogeneous green solution was obtained, and then the mixture was placed in an ultrasonic bath at 70° C for 6 min.

Semi-cell	Hydrogel used	Full-cell Integrated Hydrogel Supercapacitor	PVA/H_2SO_4 (w/w)	PVA (%)	PVA Molecular weight
S_1	**HyD#1**	**Hy_1SC**	1/4	25	31,000-50,000
S_2	**HyD#2**	**Hy_2SC**	1/4	9	89,000-98,000

Table 1.3: Semi-cell and Integrated Hydrogel Supercapacitor composition with PANI_PAMPSA suspension/PVA (w/w) ratio of 0.5

To obtain the double-layer hydrogel semi-cell (**S_1 and S_2, Table 1.3**), a layer of HyPVA (electrolyte) was first poured into a Petri dish of 8 cm diameter and subjected to 30 min of freezing. Afterward, a layer of HyPVA/PANI_PAMPSA (electrode) was deposited on it. Finally, the double-layer hydrogel configuration was subjected to 6 freeze-thaw cycles. The amount of conductive polymer inside the hydrogel layer is 0.023 g.

To obtain the all-in-one HySC, three hydrogel solutions were prepared in three

different flasks, one containing only PVA and two also containing the PANI_PAMPSA. The two Petri dishes containing the HyPVA-PANI_PAMPSA were placed in the freezer at −18 °C for 30 min to ensure a semi-solid consistency. Then, without waiting for its thawing, the electrolyte solution (HyPVA), kept at room temperature, was poured onto the layer of HyPVA-PANI_PAMPSA prepared before. Finally, the second layer of HyPVA-PANI_PAMPSA was gently overlapped as shown in **Fig. 1.8**. After 6 freeze–thaw cycles, the final compact integrated system (HySC) was obtained.

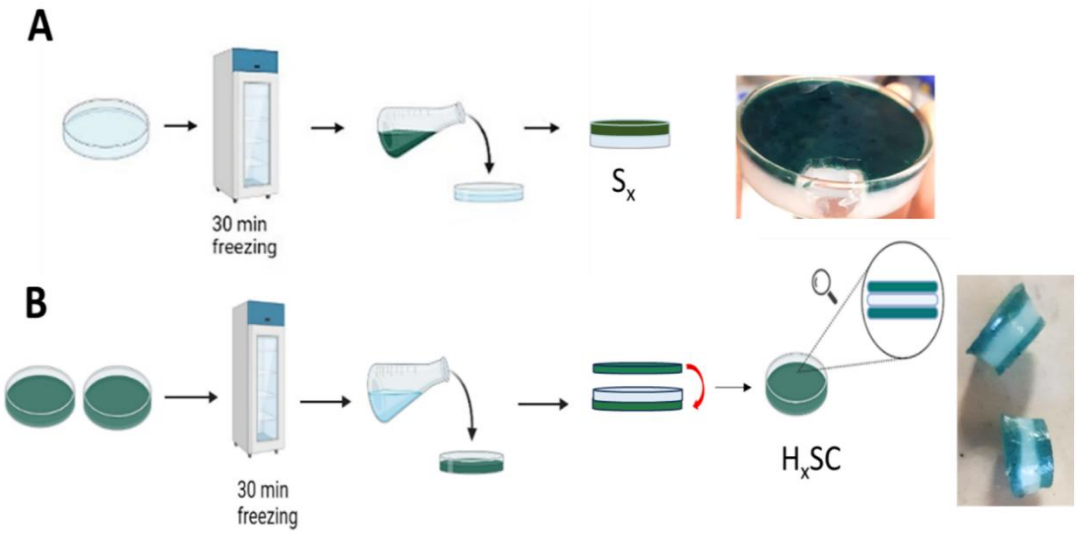

Fig. 1.8: Assembly schemes of (**A**) semi-cell & (**B**) full-cell hydrogel supercapacitor

1.7. Characterization of materials

1.7.1. Characterization of PANI-modified cellulose fibers and sheets

Scanning electron microscopy (SEM) was used to examine the surface morphology of the samples. The pristine cellulose fibers (Cell-F) exhibited a smooth and clean appearance (**Fig. 1.9A**). In contrast, the PANI-modified fibers (Cell/PANI-F) showed a rougher texture (**Fig. 1.9B**), indicative of the polymer coating. The deposited PANI layer formed a relatively compact structure, uniformly covering the fiber surface, with an estimated thickness of approximately 4.4 μm [64]. **Fig. 1.9C** reports the SEM images of the PANI_PAMSA modified fibers.

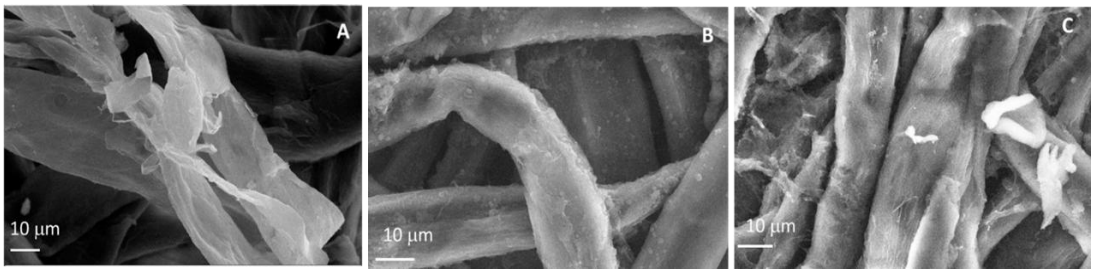

Fig. 1.9: SEM images of bare Cell-F (A) and Cell/PANI-F (B) and Cell/PANI_PANSA-F (C)[64]

The ATR-FTIR spectra (**Fig. 1.10**) provide clear evidence of the functional groups associated with PAMPSA and the Cell/PANI_PAMPSA composites. Distinct absorption bands were observed near 1650 cm^{-1} and 1032 cm^{-1}, which can be assigned to the carbonyl (C=O) vibration and the symmetric stretching of the sulfonic group (O=S=O), respectively, characteristic of PAMPSA[69,70]. Additional signals at 1296 cm^{-1} and 1148 cm^{-1} correspond to protonated amine and protonated imine functionalities[71]. Other relevant peaks include those at 923 cm^{-1} (S-O stretching) and 795 cm^{-1} (C-S stretching and C-H out-of-plane bending)61[71], as well as features between 1302-1304 cm^{-1}, 1243-1245 cm^{-1}, and 1108-1119 cm^{-1}, which are consistent with PANI emeraldine salts[63,71,72]. The presence of bands at 1546 cm^{-1} and 1440 cm^{-1}, assigned to quinoid and benzenoid structures, indicates interactions between the PANI backbone and PAMPSA, likely facilitated by protonation-induced π-electron delocalization[69]. Overall, these IR results, in combination with SEM observations, confirm that the in-situ synthesis yields a uniform PANI_PAMPSA coating over the cellulose fibrils.

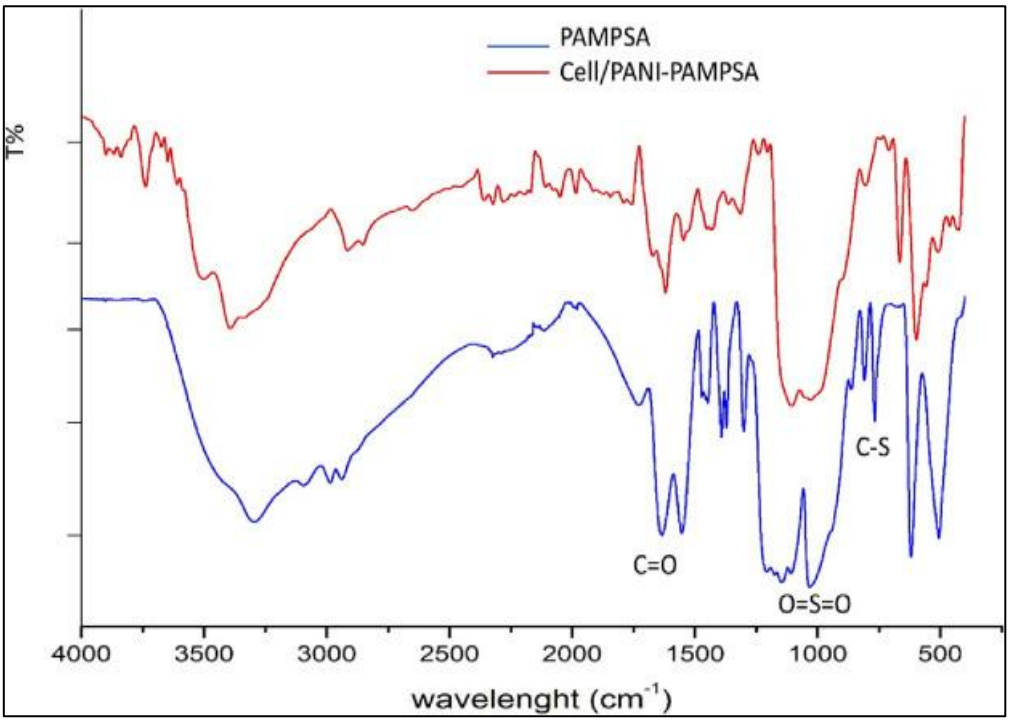

Fig. 1.10: ATR-FTR spectra of Cell/PANI_PAMPSA and PAMPSA[64].

The thermogravimetric analysis (TGA) profiles of pristine cellulose, Cell/PANI, and Cell/PANI_PAMPSA are presented in **Fig. 1.11**. The initial weight loss of approximately 5%, occurring up to 160–180 °C, is attributed to the evaporation of adsorbed water, reflecting the hygroscopic character of both cellulose and polyaniline. A second degradation stage begins around 160 °C. In this region, the Cell/PANI sample shows a larger mass loss (65.2%) compared to Cell/PANI-PAMPSA (57.6%), which can be assigned to the release of dopant molecules, low-molecular-weight oligomers, crosslinked fragments, and the onset of polymer backbone decomposition. A third stage, observed near 500 °C, corresponds to the complete breakdown of the cellulose and polyaniline frameworks, along with the evolution of smaller molecular fragments and gaseous by-products. At 900 °C, the Cell/PANI_PAMPSA retains a residue of 24.3%, composed mainly of inert, carbonized chain fragments[73].

Interestingly, the larger weight change in Cell/PANI at around 160 °C suggests a more pronounced loss of dopant species. Since hydrochloric acid is the primary dopant, acid release tests were performed by placing both composites in sealed chambers with pH indicator paper for 72 h. For Cell/PANI, the indicator turned

red within 48 h, confirming acid release. In contrast, no color change was observed for Cell/PANI_PAMPSA under identical conditions. These results demonstrate that the PAMPSA-based system exhibits greater stability and improved biocompatibility compared to the HCl-doped Cell/PANI.

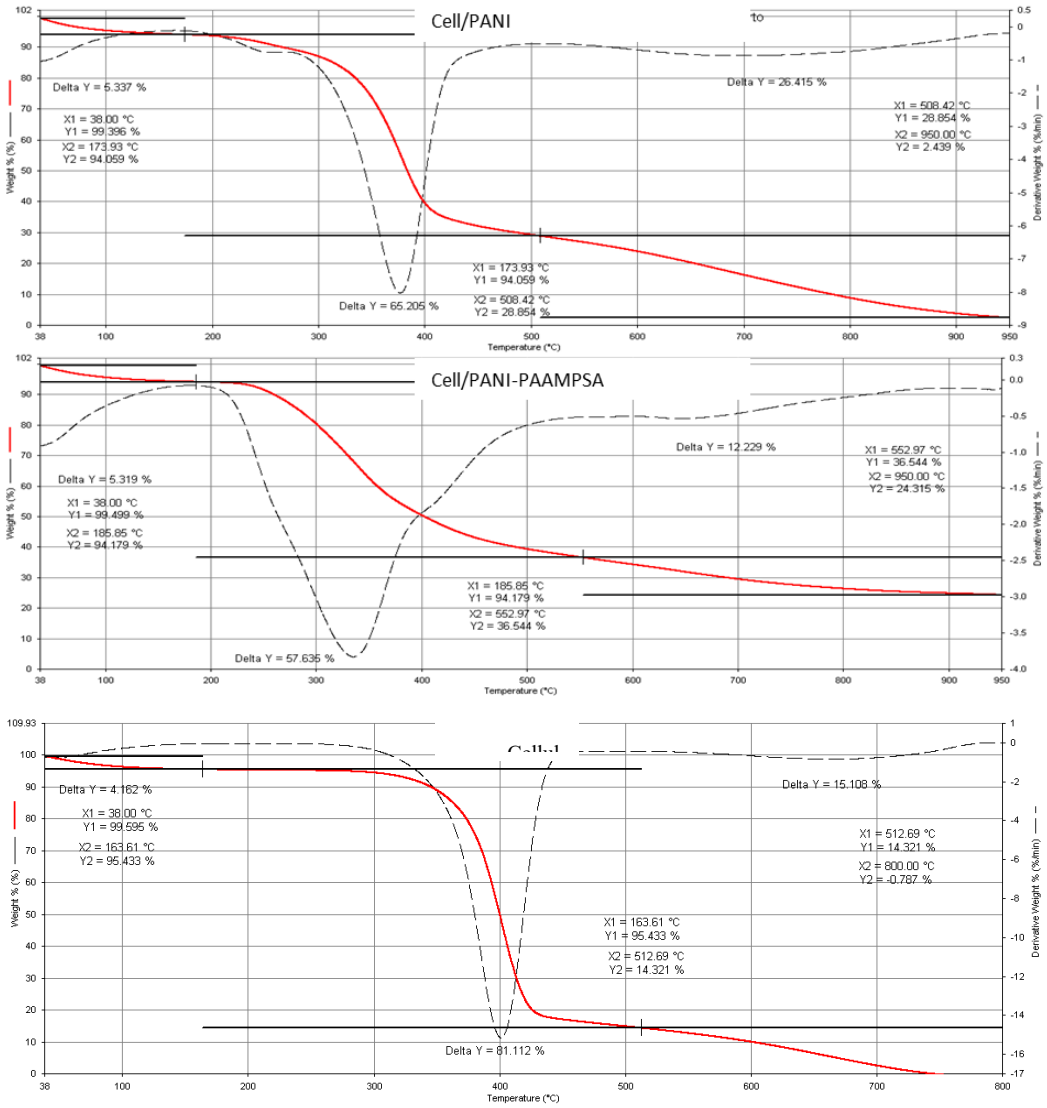

Fig. 1.11: TGA of Cell/PANI and Cell/PANI_PAMPSA and bare cellulose[64]

Tensile testing (**Table 1.4** and **Fig. 1.12**) demonstrated that incorporating PANI adds stiffness, while the addition of PAMPSA helps preserve flexibility. The Young's modulus of the Cell/PANI_PAMPSA composite was higher than that of pristine cellulose but lower than that of Cell/PANI, indicating that PAMPSA contributes to a more compliant network. Similarly, elongation-at-break values

were higher for Cell/PANI_PAMPSA than for Cell/PANI, underscoring improved ductility.

Sample	Stress at break (MPa)	Strain at break (%)
Cellulose	0.0094 ± 0.0008	20 ± 5
Cell/PANI	0.0040 ± 0.0009	9.8 ± 0.5
Cell/PANI_PAMPSA	0.016 ± 0.003	52 ± 5

Table 1.4: Tensile strength values obtained from mechanical tests for pristine Cell/PANI and Cell/PANI_PAMPSA[64]

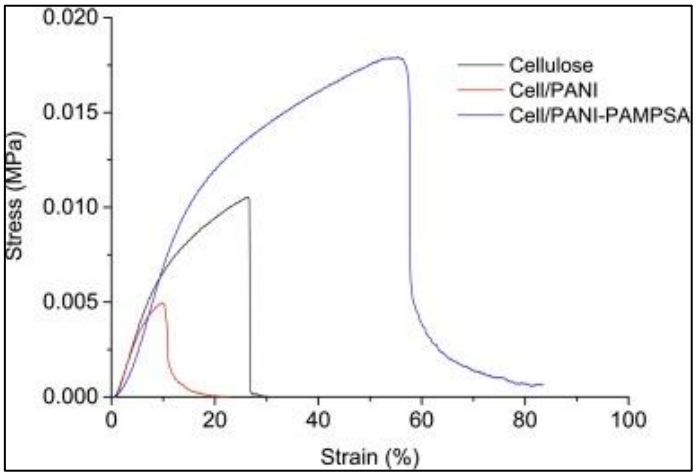

Fig. 1.12: Stress-strain curves obtained for pristine Cellulose (black line), Cell/ PANI (red line) and Cell/PANI_PAMPSA (blue line)[64]

The electrical conductivity of the cellulose composites was measured using the four-probe method (**Fig. 1.13**). The measurements were performed at different current values (100, 200, 300 μA), and a line passing from the origin was always obtained. The resistance (R) was calculated with Ohm's law, and the sheet resistance ($R_{\blacksquare}$) is equal to:

$$R_{\blacksquare} = R\,\frac{W}{L} \qquad \text{equation (1.3)}$$

where W and L are the width and the length, respectively.

The specific resistance (ρ) can be calculated by:

$$\rho = R_{\blacksquare}\, t$$ equation (1.4)

where *t* is the thickness.

The specific conductance (κ) is calculated by:

$$\kappa = \frac{1}{\rho}$$ equation (1.5)

The Cell/PANI-PAMPSA samples exhibited significantly enhanced conductivity compared to pristine cellulose, reaching values on the order of 10^{-2} S cm^{-1}, whereas the unmodified cellulose remained insulating (below 10^{-7} S cm^{-1}). The improved conductivity is attributed to the formation of a continuous PANI conductive network facilitated by the PAMPSA dopant, which enhances charge delocalization and connectivity among fibrils[74,75,76].

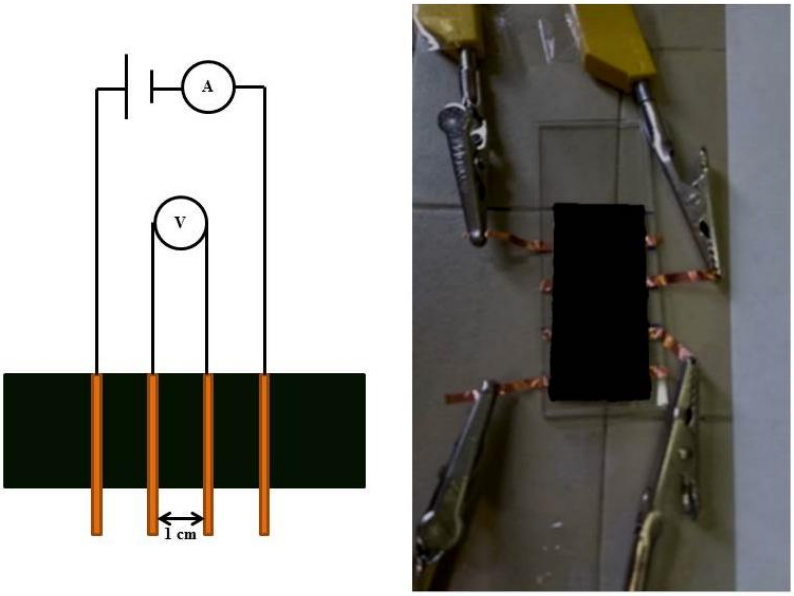

Fig. 1.13: Sample holder for resistance measurements[64]

Electrochemical impedance spectroscopy (EIS) revealed that Cell/PANI-PAMPSA has a lower charge-transfer resistance than Cell/PANI alone (**Table 1.5**).

Sample	Conductivity (S cm^{-1}) (*10^{-1})
Cell/PANI	3.45 ± 0.01
Cell/PANI_PAMPSA	0.537 ± 0.001

Table 1.5: Conductivity values for Cell/PANI and Cell/PANI_PAMPSA

As shown in (**Fig. 1.14**), the conductivity of Cell/PANI decreased steadily by about 39% during folding, and the material ultimately failed after 200 cycles (**Fig. 1.15**). In contrast, Cell/PANI_PAMPSA retained better stability, with conductivity reduced by only 16%, and visible damage appearing only after 500 folding.

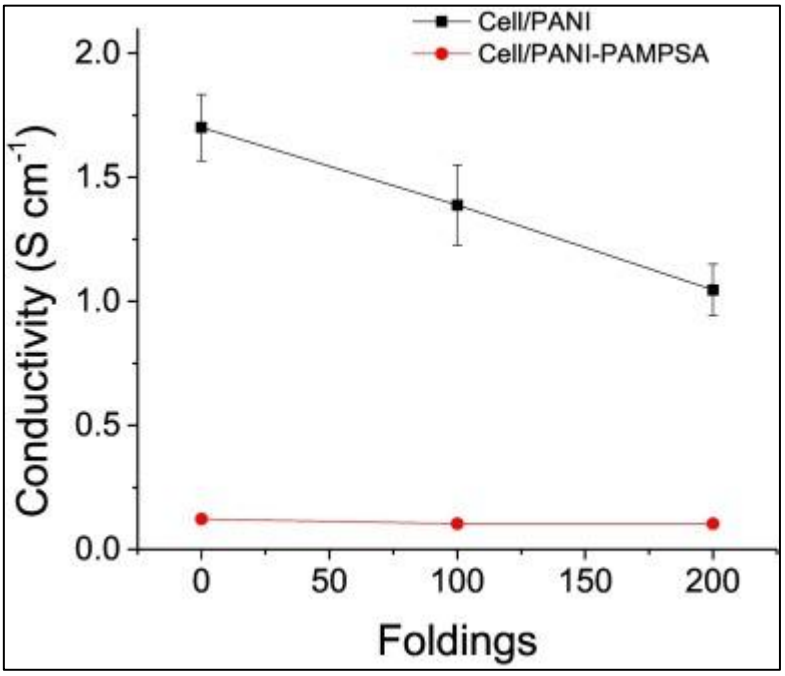

Fig. 1.14: Conductivity graphs vs folding number for Cell/PANI and Cell/PANI_PAMPSA during the bending test. (Error bars for Cell/PANI_PAMPSA are negligible)

Overall, the incorporation of PAMPSA enhances the mechanical durability of the paper while helping to maintain its electrical performance under repeated

mechanical stress. However, since PAMPSA is an insulating polyelectrolyte, its addition results in lower electrical conductivity compared to sheets made solely from Cell/PANI.

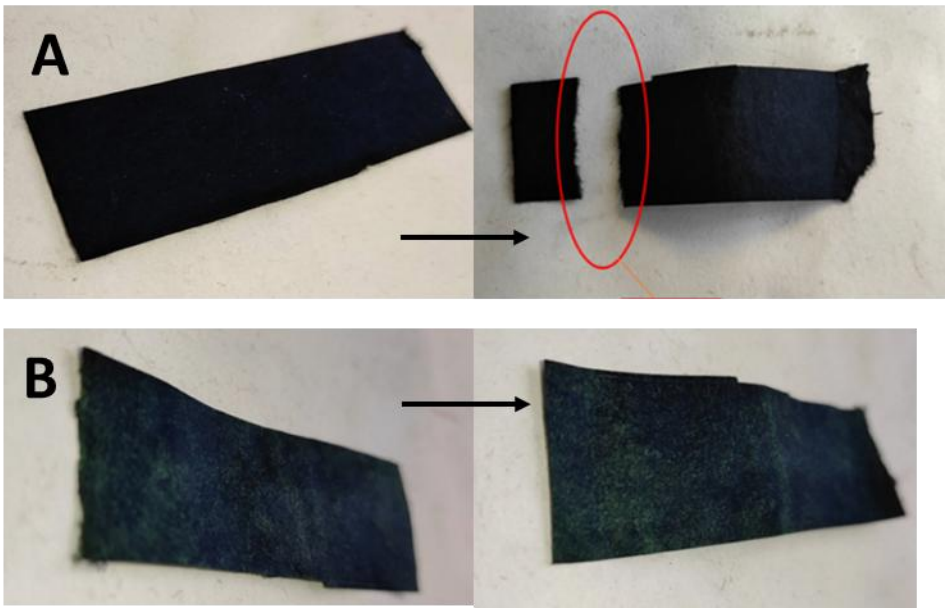

Fig. 1.15: Cell/PANI (A) and Cell/PANI_PAMPSA (B) before and after 200 folding

1.7.2. Characterization of monolayer PVA hydrogels

Before ATR-FTIR spectroscopy and scanning electron microscopy (SEM) characterization, the PVA-hydrogels were subjected to lyophilization to eliminate residual water. To prevent acid contamination of the freeze-dryer, hydrogels prepared from low, medium, and high-molecular-weight PVA (HyA, HyB and HyC) were thoroughly rinsed with distilled water to remove any remaining H_2SO_4. After washing, the pH of the sample was monitored using litmus paper, and washing was discontinued once neutrality (pH 7) was reached. The washed samples were frozen at -19 °C overnight, followed by freeze-drying in a Labconco unit operated at -50 °C and 0.850 mbar for 24 h.

Thermal properties were assessed using differential scanning calorimetry (DSC), which was employed to determine both crystallinity and glass transition temperature (Tg) after each freeze-thaw cycle. The degree of crystallinity was calculated as the ratio of the fusion enthalpy (ΔHm) of the hydrogel sample,

normalized to the polymer content, to the reference enthalpy of melting for fully crystalline PVA (ΔH_m° = 150 J g^{-1}). Wide-angle X-ray diffraction (WAXD) measurements were also performed to evaluate crystallinity[77]. Data were collected using a Philips X'Celerator diffractometer equipped with a graphite monochromator, employing CuKα radiation (λ = 1.54 Å, 40 mA, 40 kV). Scans were recorded from 10° to 60° (2θ) with a step size of 0.3° and a time step of 10 s. Relative crystallinity was calculated as the ratio between the crystalline peak area centered around 19.4° and the total scattering area within the measured range, using X'Pert HighScore Plus software. This value is comparative across samples but does not correspond to an absolute crystallinity percentage.

For additional thermal analysis, thermogravimetric analysis (TGA) and differential scanning calorimetry (DSC) were conducted on hydrogels that had been pre-dried in an oven at 50 °C for 48 h. TGA was performed under a nitrogen atmosphere using a Netzsch TG209F1 Libra instrument, heating from 25 to 600 °C at a rate of 20 °C min^{-1}. DSC thermograms were obtained with a TA Instruments Q2000 using unsealed aluminum pans containing 3-5 mg of crude sample. Two successive heating-cooling cycles between 0 and 250 °C were applied at a rate of 10 °C min^{-1}.

$$\text{DSC crystallinity} = \frac{\Delta H_m}{\Delta H_m^0} \qquad \text{equation (1.6)}$$

$$\text{Relative crystallinity} = \frac{PVA\ crystalline\ peak\ are}{total\ area} * 100 \qquad \text{equation (1.7)}$$

The DSC curves corresponding to the first heating and cooling ramps of the PVA-H_2SO_4 hydrogels are shown in (**Fig. 1.16A**) within the temperature range of 150-250 °C. All thermograms displayed an endothermic peak between 210 and 240 °C during the heating cycle, attributed to the melting of crystalline domains formed during the freeze–thaw process, followed by a recrystallization event upon cooling. As expected, a slight shift of the melting peak was observed with increasing PVA molecular weight, whereas in the case of HyB, no significant variation was detected upon changing the polymer content. The degree of crystallinity was determined from the melting enthalpy according to equation 6 [78], with the corresponding data reported in (**Fig. 1.16B**). The analysis revealed that the final hydrogels possessed a relatively low crystallinity, in the range of 7–9%.

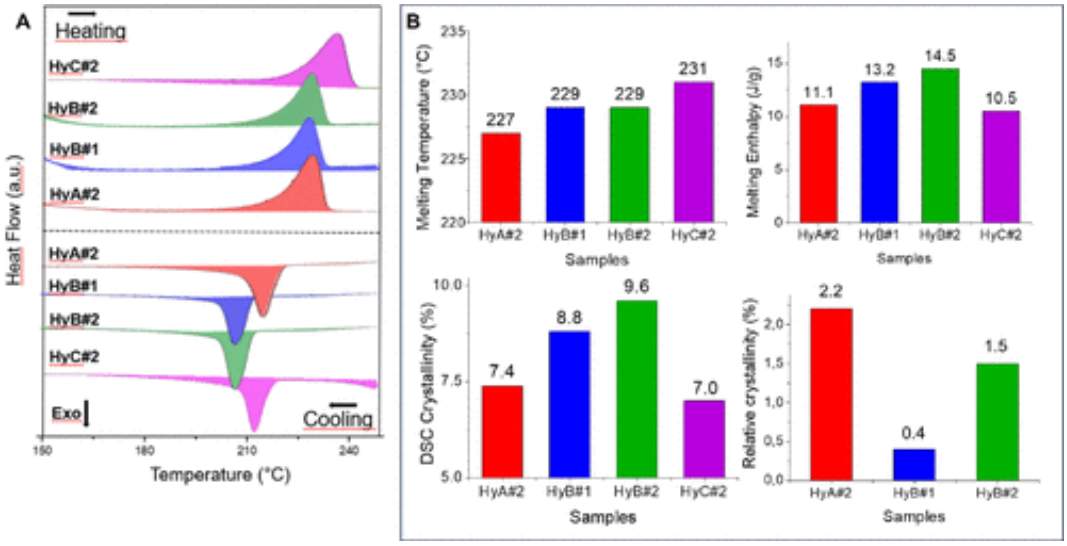

Fig. 1.16: (A) DSC thermograms in the range 150-250 °C for each prepared hydrogel; (B) melting temperature (°C), melting enthalpy (J/g), and crystallinity (%) of different gels obtained by DSC and WAXD.[44]

The relative crystallinity of the hydrogels was further evaluated by WAXD, following established methodologies[79]. During gelation, a porous polymeric network is formed in which microcrystalline PVA domains act as junction points; however, these crystallites are typically very small, and their extent increases with the number of freeze-thaw cycles, hydrogel aging, and solvent content. The WAXD spectra, reported in (**Fig. 1.17**), consistently display two broad halos centered at approximately 25° and 42° (2θ). Minor variations in the diffraction profiles are evident, attributable to differences in PVA molecular weight. A weak diffraction peak at 19.5 ± 0.1° (2θ), consistent with literature reports, indicates the presence of a small fraction of crystalline PVA aggregates. This feature is clearly distinguishable in HyA#2 and HyB#2, whereas in HyB#1 it appears only as a faint reflection, highlighting the dependence of crystallinity on both polymer concentration and molecular weight. As noted by Ricciardi et al.[80], distinct crystalline patterns detectable by XRD are generally observed only in hydrogels containing >10-15% (w/w) PVA when the polymer MW is ~115,000. The absence of the crystalline PVA reflection in HyC#2 and the broad diffraction pattern of HyB#1 corroborate this trend, as these samples were derived from a 9% (w/w) polymer solution and from a more concentrated but lower-MW polymer,

respectively (**Table 1.2**). The relative crystallinity, calculated according to equation 7, is reported in (**Fig. 1.16B**) and falls within the range previously described in the literature[81] (0.03-5.3, depending on polymer concentration and number of cycles). No relative crystallinity value was determined for HyC#2. Furthermore, the higher amorphous content observed in HyB#1 and HyC#2 can be attributed to the increased sulfuric acid content in these systems, corresponding to PVA/H_2SO_4 weight ratios of 1/5.8 and 1/10, respectively[76].

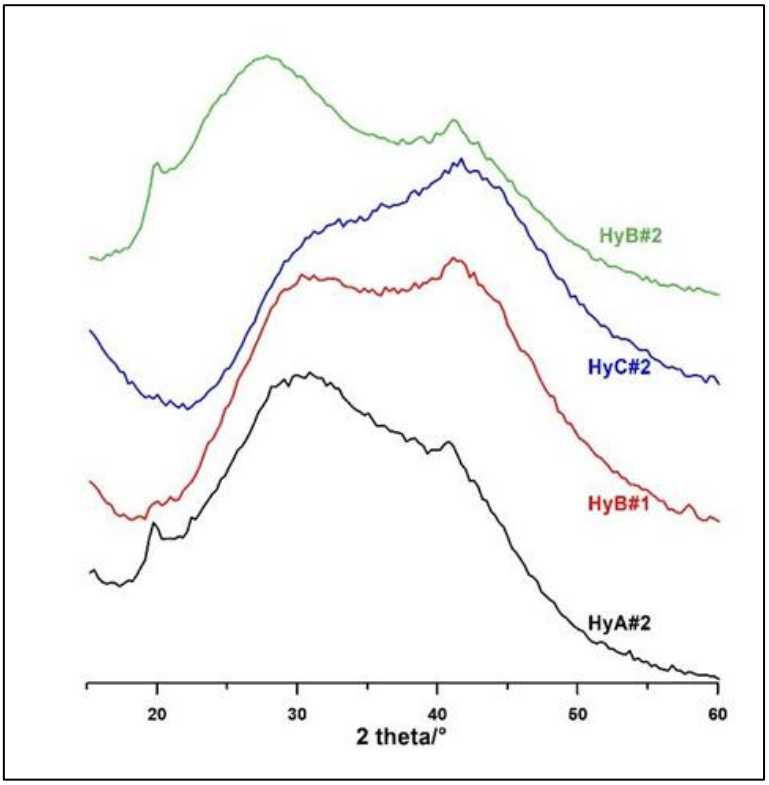

Fig. 1.17: X-Rays diffraction patterns of the investigated samples[44].

The thermal stability of the freeze-thaw hydrogels was assessed by thermogravimetric analysis TGA (**Fig. 1.18**). Within PVA hydrogels, water exists in different states: weakly bound (absorbed) water, which remains on the external or internal surfaces without significant interaction with the matrix, and strongly bound water, which interacts with hydroxyl groups. The TGA curves of PVA-hydrogels under a nitrogen atmosphere reveal three distinct weight-loss regions, consistent with those previously reported[82,83]. The first region, observed between

50 and 200 °C, corresponds to the release of absorbed water. The second region, between 200 and 340 °C, is associated with the loss of strongly bound water. Finally, the third region, occurring between 340 and 450 °C, corresponds to the thermal decomposition of the polymer backbone[84].

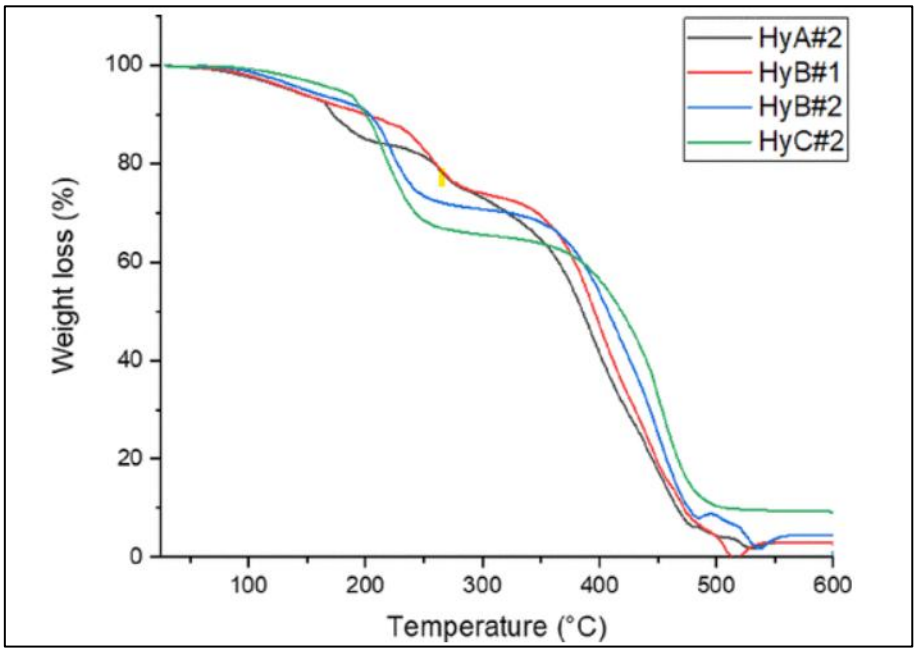

Fig. 1.18: TGA curves of the prepared hydrogels[44].

ATR–FTIR spectra were recorded on a PerkinElmer Spectrum Two spectrophotometer equipped with a Universal ATR accessory, with a resolution of 0.5 cm^{-1} over the range 4000-400 cm^{-1}, averaging 40 scans. Surface morphology was observed using a Renishaw field-emission scanning electron microscope with an InLens detector, operating at 10 kV and 80 pA.

The presence of crystalline domains resulting from the freeze–thaw process, as confirmed by DSC and WAXD, is consistent with observations reported in the literature.

The ATR–FTIR spectra of the lyophilized hydrogel samples and pristine PVA are presented in (**Fig. 1.19**). Characteristic absorption bands of PVA are evident at 3400 cm^{-1} (−OH stretching), 2950 cm^{-1} (−CH_2 stretching), and 1090 cm^{-1} (C–O stretching), confirming the formation of the hydrogel network. In addition, a distinct band at 1142 cm^{-1}, attributed to the crystalline domains of PVA, is also observed[85].

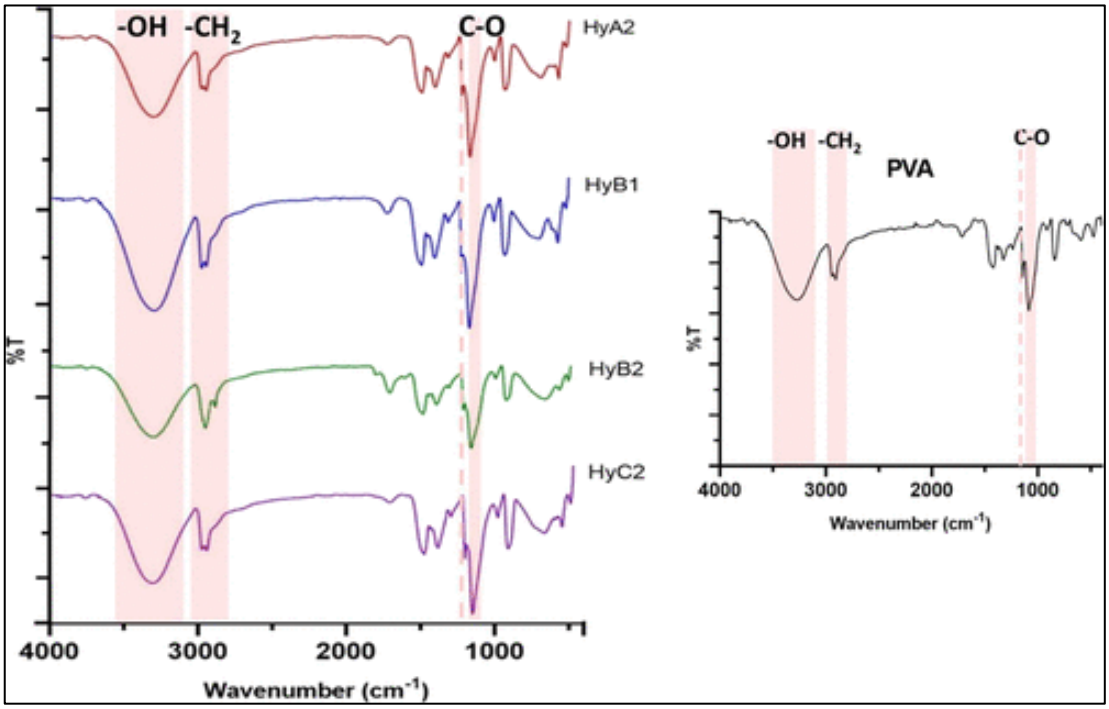

Fig. 1.19: ATR-FTIR spectra of HyA#2, HyB#1, HyB#2, and HyC#2. Inset: spectrum of PVA[44].

The mechanical tensile properties of the PVA hydrogel were measured using an LBG UDI24 Pro instrument equipped with a 1 kN load cell at room temperature. The hydrogels were cut into strips measuring 40 mm × 10 mm, and tensile tests were performed by uniaxially stretching the strips at a rate of 10 mm min^{-1} (**Fig. 1.20**). Stress (σ) and strain (ε) were calculated according to standard equations, where L_o represents the initial gauge length and L the elongated length of the specimen. Young's modulus was determined from the average slope of the linear region (1-5% strain) of the stress-strain curve (**Fig.1. 21** and **Table 1.6**)[41].

$$\sigma = \frac{F}{A}; \qquad \text{equation (1.8)}$$

where F = force in kN and A = cross-section area in mm^2

$$\varepsilon = \frac{L - L_0}{L_0}; \qquad \text{equation (1.9)}$$

where L_0 = initial length in mm and L = final length in mm

Fig. 1.20: The mechanical tensile strength test.

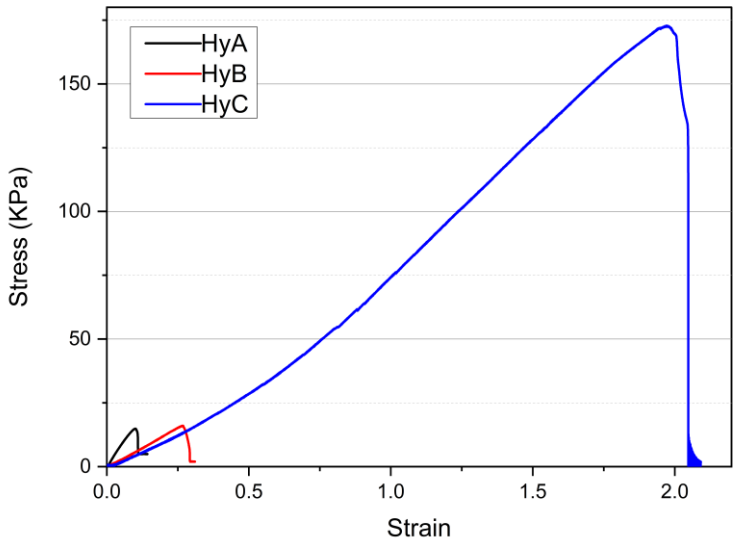

Fig. 1.21: Stress Vs. strain curve of hydrogels (each curve was the average of three measurements) [44].

Hydrogel name	HyA	HyB	HyC
Tensile strength (Kpa m^{-3})	0.10 ± 0.44	2.39 ± 0.40	113 ± 0.73
Elongation at break (%)	8	24	167
Young modulus (KPa)	175.10 ± 0.44	60.09 ± 0.44	40.72 ± 0.05
Stress at break (MPa)	0.014	0.014	0.14

Table 1.6: Tensile strength test results of hydrogel samples.

Compression tests were conducted on the same instrument, this time using a 10 kN load cell, also at room temperature. For compression, cylindrical hydrogel specimens with a diameter of approximately 15 mm and a height of 3 or 5 mm were tested. Each measurement was repeated on three independent samples for each hydrogel formulation.

Water content (Wc%) and swelling percentage (Sw%) were measured for all hydrogel samples. The water content (Wc%) of the PVA hydrogels was determined by measuring the sample weight before drying (Wi) and after oven-drying at 40 °C for 27 h (Wd). The water content was then calculated as follows[86,87]:

$$Wc\% = \frac{Wi-Wd}{Wd} * 100\% \qquad \text{equation (1.10)}$$

where Wi is the initial weight of the hydrogel and Wd is the weight after drying.

The degree of swelling was determined by immersing dried samples in distilled water at 25 °C for 72 h to reach swelling equilibrium. After removal from the water bath, excess surface water was gently blotted with filter paper, and the swollen samples were weighed using an analytical balance. The swelling ratio (Sw%) was then calculated using the following equation[86,88]:

$$Sw\% = \frac{Ws-Wd}{Ws} * 100\% \qquad \text{equation (1.11)}$$

where Ws is the weight of the swollen gel and Wd is the weight of the dry gel.

To evaluate the contribution of PVA content (S_{PVA}%), the swelling data were normalized with respect to the polymer fraction (f) in the hydrogel, according to the following equation:

$$S_{PVA}\% = \frac{Sw\%}{f} \qquad \text{equation (1.12)}$$

The porosity of the dried samples was determined by measuring the adsorbed

volume of cyclohexane versus the total volume of each sample using a pycnometer. Equation 1.13 was used for the calculation [89]:

$$Porosity\% = \frac{V_{porous}}{V_{sample}} * 100\% = \frac{m_w - m_d}{m_1 - w_2 - m_w} * 100\% \qquad \text{equation (1.13)}$$

where m_d is the mass of the dry gel, m_w is the mass of the wet hydrogel in cyclohexane, m_1 is the mass of the apparatus filled with cyclohexane, and m_2 is the mass of the apparatus with cyclohexane and hydrogel.

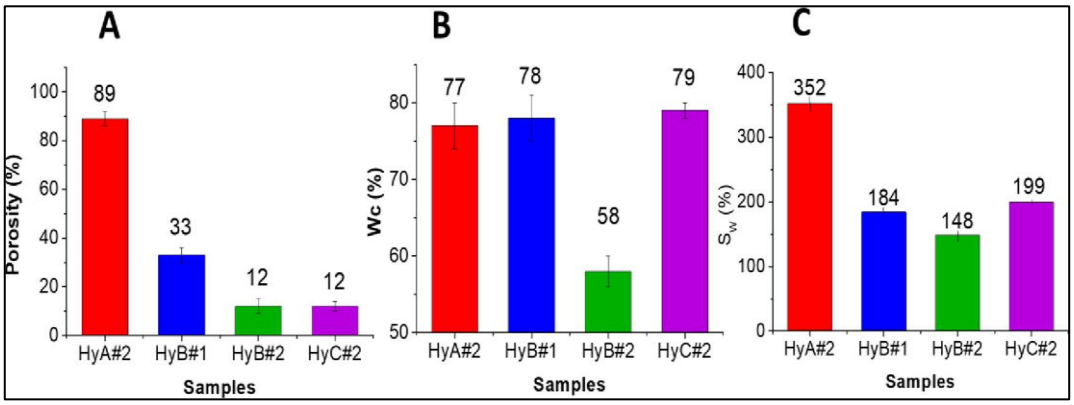

Fig. 1.22: (A) Porosity, (B) water content (Wc), and (C) swelling ratio (Sw) results[44].

Gel porosity and pore size depend strongly on the number of freeze-thaw cycles, the PVA concentration, and the PVA molecular weight (MW)[75]. Since the number of cycles was kept constant, the variations observed in the samples can be attributed either to the PVA/H_2SO_4 weight ratio or to the PVA MW. As shown in **Fig. 1.22A**, decreasing the PVA/H_2SO_4 ratio from 1/5.8 to 1/3 at constant MW reduces the porosity (compare HyB#1 and HyB#2), while increasing the PVA MW at a fixed weight ratio also decreases porosity (compare HyA#2 and HyB#2). Similar porosity values were obtained for HyB#2 and HyC#2.

The water content (Wc%) and swelling percentage (SW%), calculated using equations 10 and 11[82], are reported in **Fig. 1.22 B** and **C**. The swelling percentage normalized to the polymer fraction (SPVA%), calculated with equation 12[82], yielded values of 10, 11, 3, and 22 for HyA#2, HyB#1, HyB#2, and HyC#2, respectively. During swelling, water molecules diffuse into the polymer network and interact with the hydroxyl groups of the polymer chains, leading to an

expansion of the hydrogel volume. This expansion occurs primarily in the amorphous regions of PVA[82].

Taken together, the data in **Fig. 1.22** and **Fig. 1.23** indicate that SPVA decreases with increasing crystallinity. The highest SPVA value was observed for HyC#2, prepared with a PVA/ H_2SO_4 weight ratio of 1/10 and a higher PVA molecular weight.

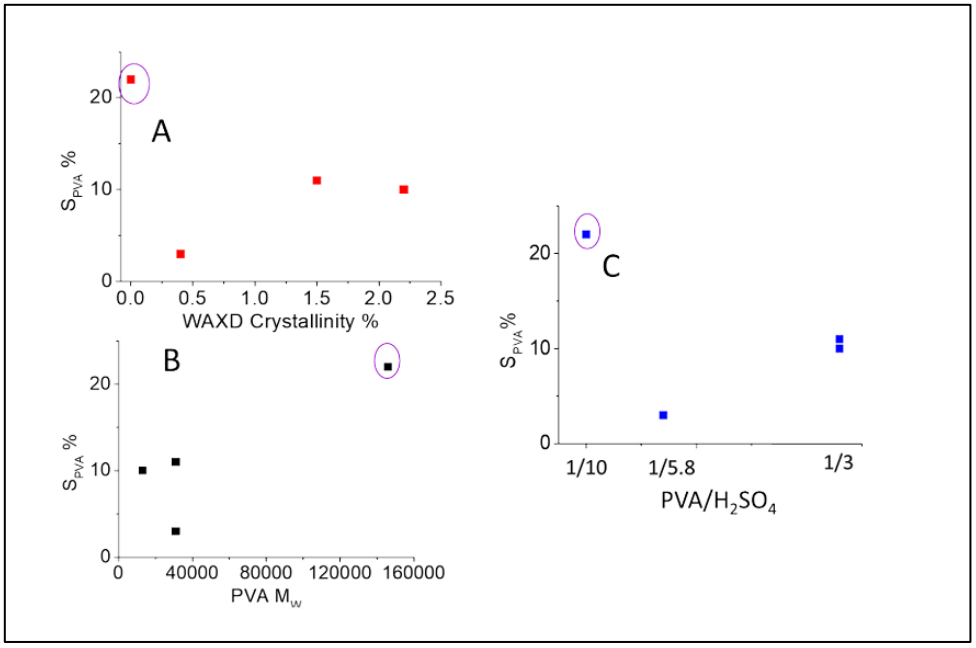

Fig. 1.23: SPVA as a function of: A) WAXD Crystallinity % and B) PVA Mw and C) PVA/H_2SO_4 w/w ratio[42].

The rheological behavior of PVA hydrogels was analyzed using an MCR 102 parallel-plate rheometer (Anton Paar, Graz, Austria) equipped with a 25 mm plate–plate geometry (PP-25) and a 1.2 mm gap. Hydrogel disks (25 mm diameter, 1.2 mm thickness) were placed on the lower plate, and the upper plate was lowered until it contacted the sample surface. Excess material was carefully removed with a spatula, and the solvent trap was filled with distilled water to prevent evaporation during testing.

Oscillatory frequency sweep measurements were performed at 25 °C with a frequency range of 500 to 0.1 rad·s^{-1} and a fixed strain of 1% to evaluate the self-healing properties of the hydrogels. In addition, oscillatory amplitude sweep tests were carried out at 25 °C to determine the stress threshold at which polymer chain

flow occurred, and network interactions were disrupted. For this analysis, the frequency was kept constant at 1 rad·s^{-1} while the applied shear strain amplitude varied from 0.01% to 1000%.

Finally, the thixotropic response was assessed using a three-interval thixotropy test (3ITT) under controlled shear rate (CSR) mode. The hydrogel was first subjected to a low shear rate (0.1 s^{-1} at 25 °C) to simulate resting conditions, followed by application of a high shear rate (100 s^{-1}) to induce structural breakdown, and then returned to the initial low shear rate to evaluate recovery of material properties. The applied high shear rate of 100 s^{-1} was selected based on the results of the amplitude sweep test.

The ionic conductivity of the hydrogels was evaluated using electrochemical impedance spectroscopy (EIS) on an Autolab GSTAT128 N potentiostat/galvanostat (Metrohm-Autolab) controlled by NOVA 2.10 software. Measurements were performed in a two-electrode Swagelok-type cell, where the samples were sandwiched between two 316 stainless steel electrodes with a testing diameter of 1.0 cm (electrode area = 0.785 cm^2, (**Fig. 1.24**). EIS was conducted with an applied AC amplitude of 10 mV over a frequency range of 0.01-10^5 Hz. The impedance data were obtained from Nyquist plots of the hydrogels, and the ionic conductivity (σ_c, S·cm^{-1}) was calculated using the equation below[41]:

$$\sigma_c = \frac{s}{RA} \qquad \text{equation (1.14)}$$

where s is the thickness of the sample (cm), R is the ionic resistance (Ω), and A (cm^2) is the surface of the analyzed sample that is in contact with the electrodes.

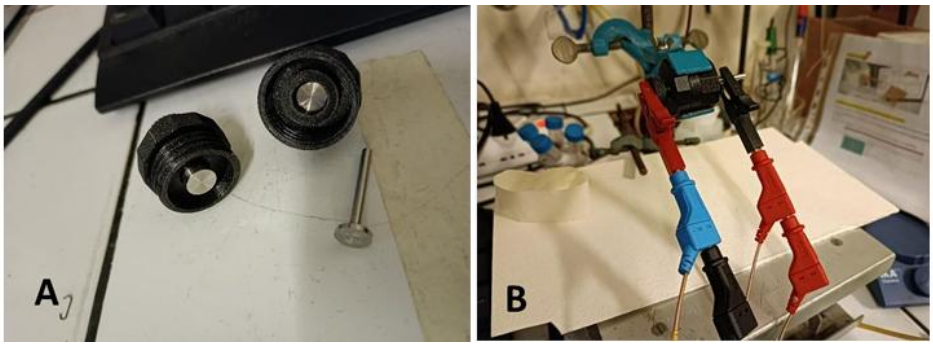

Fig. 1.24: (A) Swagelok type cell with a 316 stainless steel caps of 1.0 cm diameter and (B) configuration for electrochemical measurements[44].

Ionic conductivity is a key parameter for the potential application of hydrogels in all-in-one supercapacitors. The ionic conductivity of PVA hydrogels was measured at room temperature, with resistance values determined from Nyquist plots[83]. As shown in **Fig. 1.25A**, the bulk resistance (R) corresponds to the interception of the real axis (Z′) in the high-frequency region. Ionic conductivity was then calculated for each sample using the respective R values (equation 1.14). The conductivity and porosity values (obtained from equations 1.14, 1.13) are summarized in **Fig. 1.25 B** and **C**. For comparison, literature reports a conductivity of 580 mS cm^{-1} for similar PVA/H_2SO_4 (1 M) hydrogels[41].

When the PVA molecular weight (MW) increases at a fixed PVA/H_2SO_4 weight ratio (e.g., HyA#2 vs HyB#2), stronger physical interactions between polymer chains and higher hydrogel resistance are observed. Although high MW correlates with increased viscosity, it also reduces the number of chains ends and the available free volume, which restricts ionic mobility and lowers conductivity[81]. Conversely, at constant MW but lower polymer concentration (HyB#1 vs HyB#2), ionic conductivity improves, consistent with the "breathing polymeric chain model"[81]. In this model, a gel electrolyte comprises polymer chains, solvent, and dissociated or aggregated ions. At low PVA concentrations, the system behaves more like a liquid electrolyte: polymer chains actively participate in charge transport, contributing to enhanced conductivity[81].

The PVA/H_2SO_4 weight ratio also influences ion mobility by altering viscosity, thereby controlling the number and size of channels available for ion transport. In dilute polymer solutions, chains remain isolated, whereas in concentrated solutions, overlapping coils promote entanglements. High-MW PVA introduces more chain entanglements, retaining a greater amount of water molecules. This higher water content increases the number of free dissociated ions, which enhances conductivity[81].

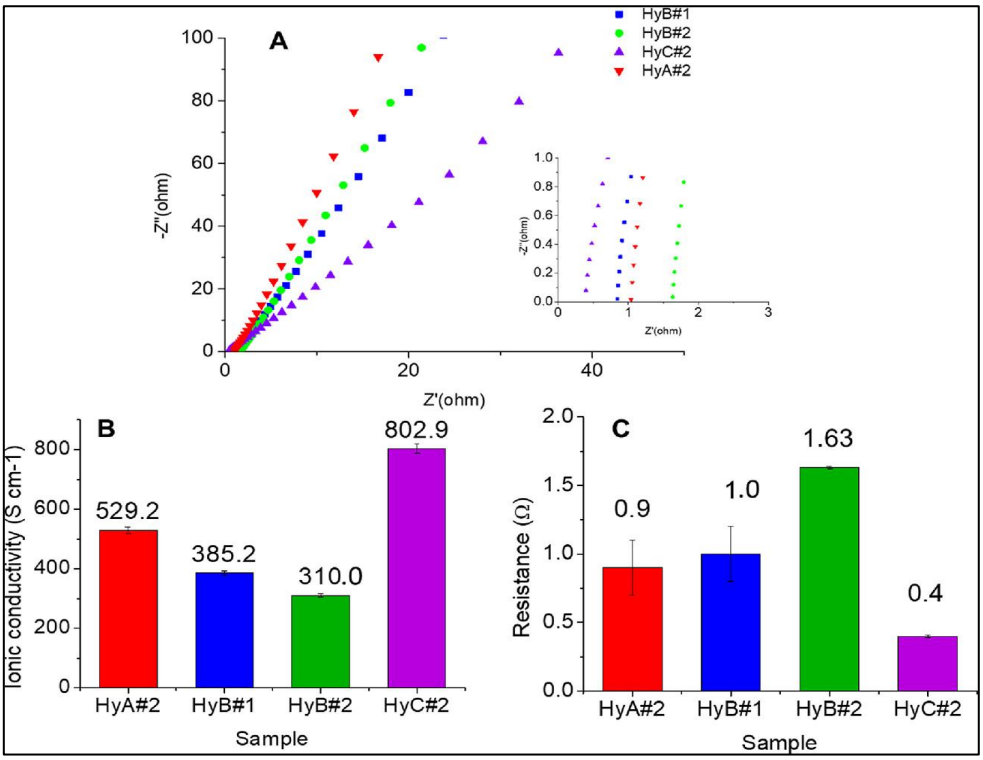

Fig. 1.25: (A) Nyquist plots; inset: enlargement of the high-frequency region. (B) Ionic conductivity (σ_c) and (C) resistance values of HyA#2, HyB#1, HyB#2, and HyC#2[44].

The highest conductivity was observed for HyC#2 (PVA/H_2SO_4 = 1/10), despite its lower porosity. This behavior can be explained by two proton transport mechanisms[78]: (i) the hopping (Grotthuss) mechanism, where protons transfer between hydrolyzed ionic sites, making porosity less critical, and (ii) the vehicle mechanism, where ions are transported via water molecules forming H_3O^+. In the latter case, hydronium ions diffuse through the aqueous medium within the free volumes of the hydrogel, driven by the electrochemical potential gradient.

Galvanostatic charge-discharge (GCD) measurements were performed on the self-healing double-layer hydrogel at a current density of 0.025 mA cm^{-2} within a voltage window of 0-0.9 V. The specific capacitance (Cp) of HyPVA-PANI_PAMPSA)/HyD semi-cell was calculated from the GCD curves using the following equation:

$$C_p = \frac{I}{A}\frac{\Delta t}{\Delta v} \qquad \text{equation (1.15)}$$

where I (A) is the discharge current, A (cm^2) is the surface of the hydrogel of the

half-cell, Δt is the difference between the end-of-discharge time and the end-of-charge time, and ΔV is the difference between the end-of-charge potential and the end-of-dischargepotential[81].

The morphology of the synthesized hydrogels was examined by SEM analysis of lyophilized samples (**Fig. 1.26**). Distinct pores, cracks, and droplet-like features were observed in HyA#2, HyB#1, and HyB#2 (**Table 1.2:** Properties of obtained hydrogels). During the freeze-thaw cycles, the freezing of water induces remodeling of the PVA phase, resulting in localized regions with higher polymer concentration. As water expands upon freezing, the PVA chains are forced into closer proximity, thereby reducing intermolecular distances and promoting physical cross-linking through hydrogen bonding as well as the formation of crystalline domains[80]. In contrast, the incorporation of a higher concentration of H_2SO_4 (HyC#2) enhances the structural integrity of the hydrogel, minimizing phase separation and yielding a more compact and homogeneous morphology.

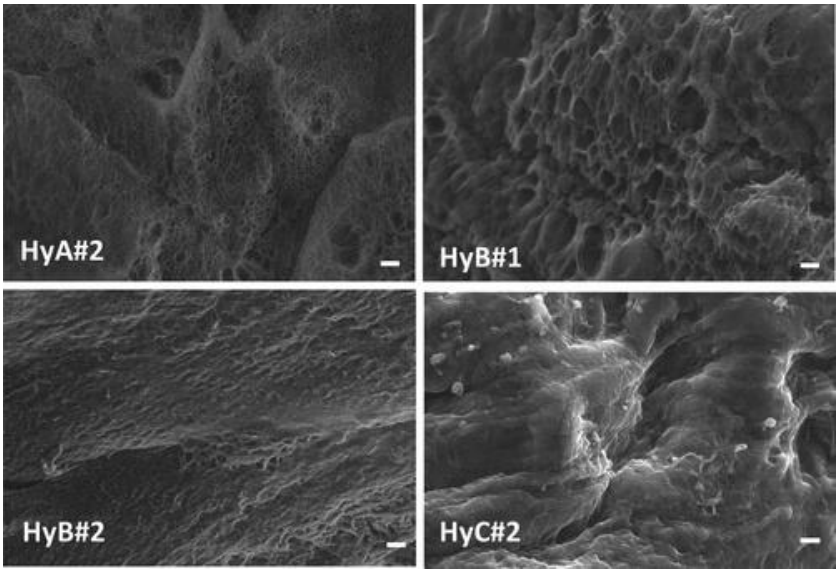

Fig. 1.26: Scanning electron micrographs of the lyophilized hydrogels, with a scale bar corresponding to 2 μm[44].

Maintaining the long-term stability of hydrogel properties: mechanical strength, hydration, and conductivity is essential for their integration into devices. All hydrogel samples were wrapped in food-grade cling film and stored at room

temperature in sealed bags until testing. As shown in **Fig. 1.27,** under these conditions, the hydrogels lost approximately 70% of their initial moisture within the first week and became nearly dry (~25% water content) after four weeks. The physical appearance of HyA#2 and HyC#2 after three months of storage is reported in **Fig. 1.28**.

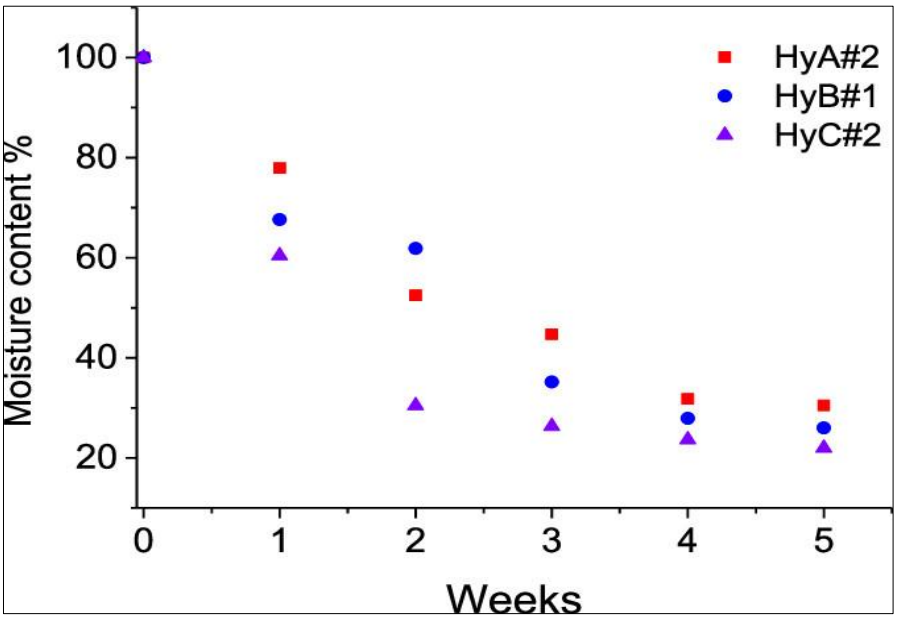

Fig. 1.27: Moisture % loss profiles of hydrogels with respect to aging time[44].

Hydrogel stability was found to depend strongly on both PVA content and molecular weight.

After four weeks, the ionic conductivity decreased to ~57% of the initial values, with measured conductivities of 302.2, 219.3, and 458.2 mS cm–1 for HyA#2, HyB#1, and HyC#2, respectively. To evaluate the possibility of regenerating the hydrogels, HyB#1 was immersed in 1.0 M H_2SO_4 for 24 h. Following this treatment, its conductivity increased from 219.3 to 306.6 mS cm^{-1}, corresponding to 79% of the original value (385.2 mS cm^{-1}).

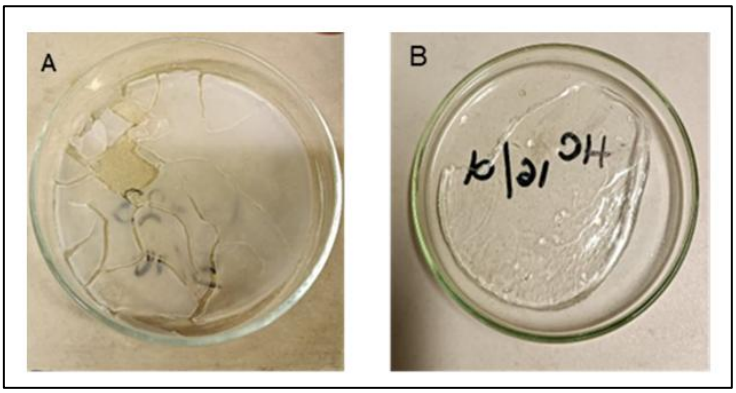

Fig. 1.28: Pictures of the hydrogels after 3 months of storage in cling film for food at room temperature: A) HyA#2 and B) HyC#2[44].

1.7.3. Characterization of semi-cell and full-cell (integrated hydrogel supercapacitor)

A sandwiched all-in-one electrode/electrolyte hydrogel was fabricated by combining the self-healing capability of PVA hydrogels with the freeze-thaw method. Self-healing PVA hydrogels prepared by this approach are well documented in the literature[89,90,91]. Both hydrogel layers were prepared under HyB#1 conditions (**Table 1.1**). The first layer consisted of pure PVA (HyD#1, or HyD#2), while the second incorporated PVA and the conductive PANI_PAMPSA polymer (50% w/w), giving the material a deep green color due to the emeraldine form of PANI[92]. After six freeze–thaw cycles, the double-layer HyPVA-PANI_PAMPSA/HyD was obtained with a total thickness of 9 mm: ~3 mm for the green HyPVA-PANI_PAMPSA layer and ~6 mm for the white HyPVA layer (**Fig. 1.29A**).

The self-healing ability of this system was confirmed through multiple tests. Visually distinct green and white hydrogel layers merged seamlessly upon contact. Optical and SEM microscopy (**Fig. 1.29B**) showed a continuous interface between the layers, confirming efficient self-healing. Mechanical testing demonstrated that the double-layer hydrogel could be stretched to a maximum tensile strain of 53 ± 4% without fracture.

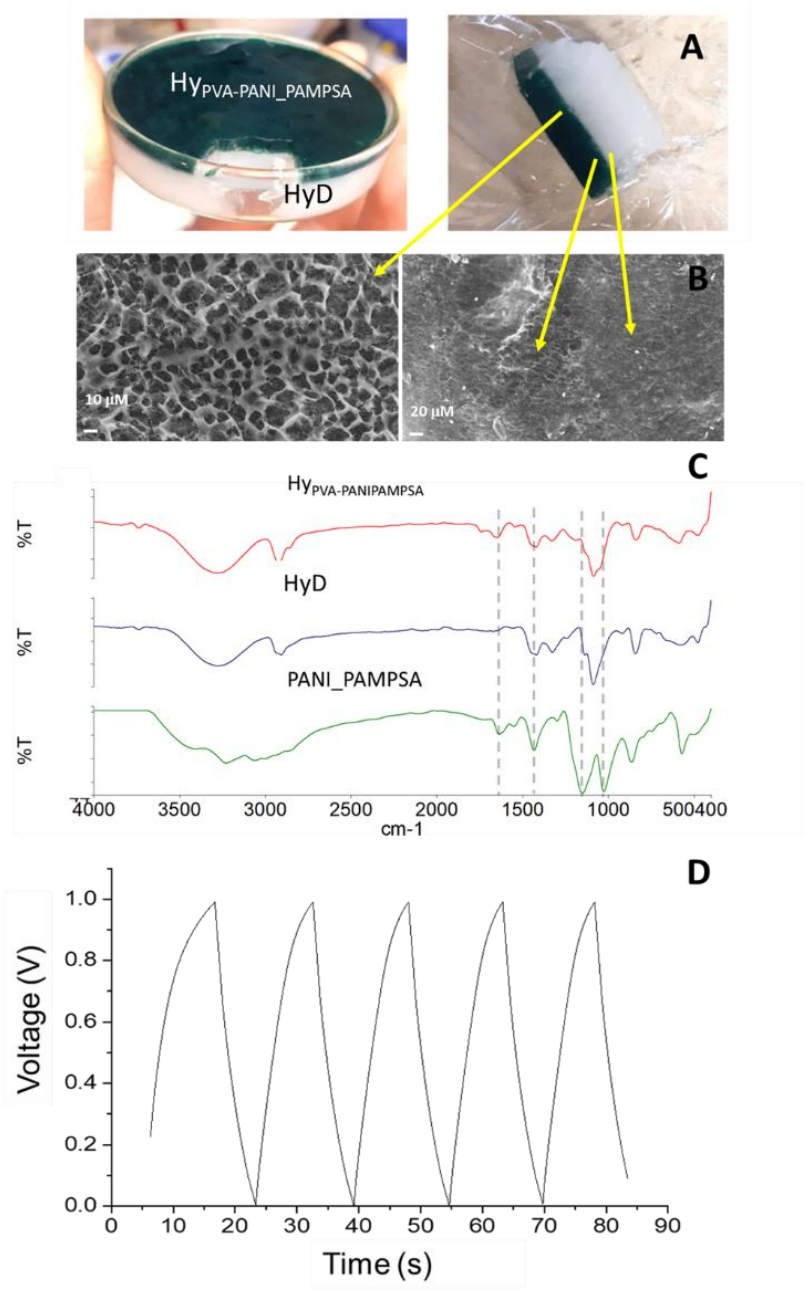

Fig. 1.29: (A) Self-healing double-layer hydrogel HyPVA–PANI_PAMPSA/HyD. (B) Micrographic images of lyophilized hydrogel recorded using SEM (magnification of 1000×). (C) ATR–FTIR spectra of HyPVA–PANI_PAMPSA, HyD, and PANI_PAMPSA. (D) GCD curves[53].

From a rheological perspective, self-healing hydrogels are expected to: (i) exhibit terminal flow pseudoplastic behavior, (ii) display a finite chain relaxation time (τf), and (iii) behave as viscous fluids at low frequencies[93]. Frequency sweep experiments at 25 °C confirmed these features. The dynamic viscosity (η′) plateaued at low frequencies with an initial slope of 0.07, indicating Newtonian flow behavior characteristic of self-healing systems (**Fig. 1.30A**) Storage and loss

modulus data (G′ and G″, **Fig. 1.30B**) revealed a crossover point (G′ = G″) at low frequencies, with G″ exceeding G′, consistent with liquid-like behavior and dynamic bond exchange. The calculated τf was 0.03 s, confirming that chain relaxation occurs on a reasonable timescale for self-healing.

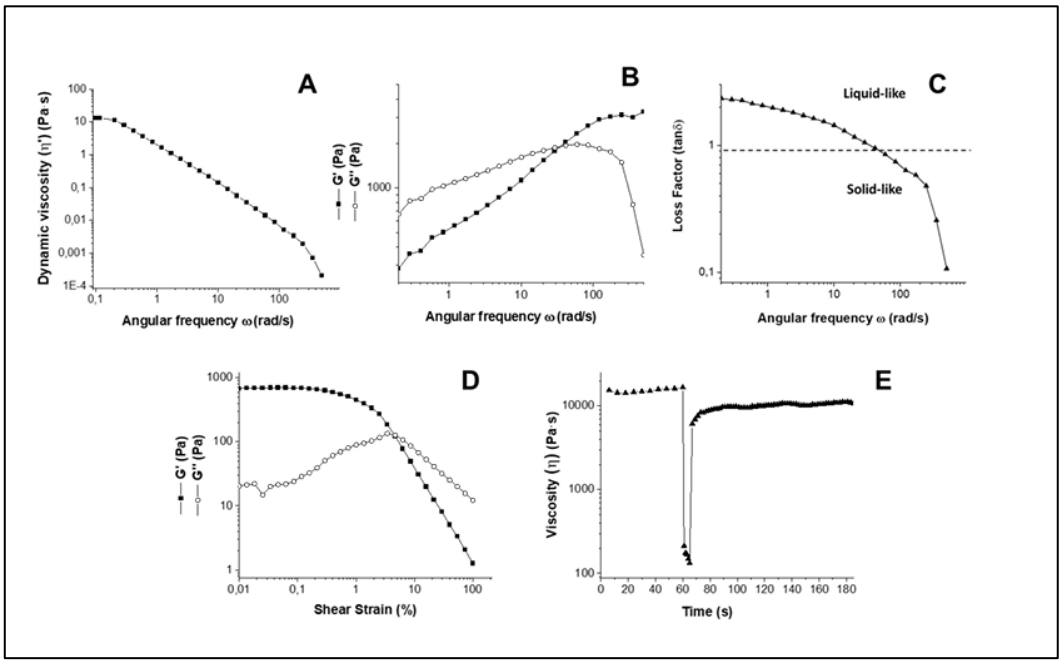

Fig. 1.30: A) Dynamic viscosity (η') versus angular frequency curve; B) Frequency sweep of PVA hydrogel; C) Tanδ versus angular frequency curve; D) Amplitude sweep curves of PVA-based hydrogels; E) 3ITT test[53].

Further characterization involved monitoring the loss factor (tan δ) as a function of angular frequency (**Fig. 1.30C**). The upward trend of tan δ at low frequencies indicated a liquid-like character dominated by chain mobility and bond exchange, further validating the self-healing mechanism. Amplitude sweeps tests revealed a crossover between G′ and G″ at 4.7% strain and 8.2 Pa stress (**Fig. 1.30D**). Using this information, a 3ITT test was performed (**Fig. 1.30D**): following bond disruption under high shear (100 s^{-1}), the hydrogel recovered 64% of its initial viscosity within 2 min, confirming robust structural recovery.

The ATR–FTIR spectrum of lyophilized HyPVA-PANI_PAMPSA (**Fig. 1.29C**) displayed characteristic PVA bands alongside signals at 1641 and 1032 cm^{-1} (C=O and symmetric O=S=O stretching of PAMPSA), and at 1546 and 1440 cm^{-1} corresponding to quinoid and benzenoid groups of PANI[94].

Finally, the self-healing double-layer hydrogel (HyPVA-PANI_PAMPSA/HyD was evaluated as a semi-cell for flexible energy storage. GCD curves (**Fig. 1.29D**) showed symmetric triangular profiles with low charge-discharge times, consistent with capacitive behavior. The specific capacitance (Cp) of HyPVA-PANI_PAMPSA/HyD#1, calculated from GCD curves (**equation 1.15**), was 0.297 ± 0.002 mF cm^{-2} at a current density of 0.025 mA cm^{-2}. The corresponding conductivities from EIS measurements are listed in **Table 1.7**.

sample	porosity (%)	ionic conductivity, σ_c (mS cm^{-1})
HyPVA-PANI_PAMPSA	17	676.0 ± 0.1
HyD	17	261.2 ± 0.2
HyPVA-PANI_PAMPSA/HyD#1	-----	439.7 ± 0.1

Table 1.7: Ionic Conductivity Values of HyPVA–PANI_PAMPSA and HyPVA–PANI_PAMPSA/HyD#1

The mechanical properties of the semi-cells were evaluated by uniaxial tensile tests, with the results summarized in **Table 1.8** and **Fig. 1.31**. A clear correlation was observed between the molecular weight of PVA and its mechanical performance: as the molecular weight increases, Young's modulus decreases while the maximum tensile strain increases. This trend is attributed to the greater tendency of longer macromolecular chains to form entanglement-type interactions with neighboring chains[95].

Semi-cell	Young's Modulus (MPa)	Strain (%)
S_1	0.18±0.03	53±4
S_2	0.05±0.02	170±1

Table 1.8: Mechanical properties of semi-cells (S_x).

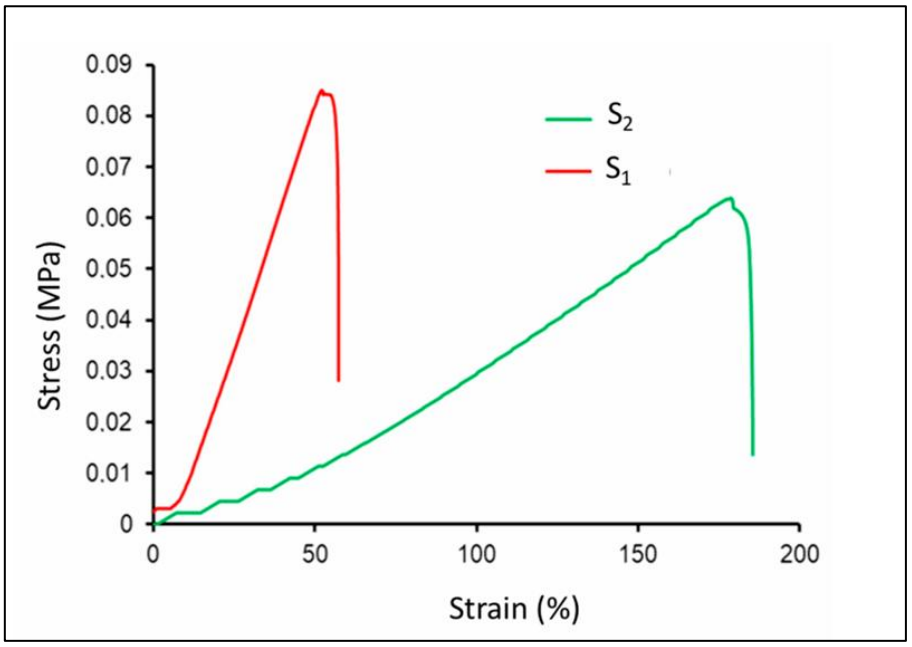

Fig. 1.31: Tensile stress/strain curves of S1 and S2[53].

The water content (Wc%), swelling ratio (S_W%), and swelling ratio normalized to the polymer fraction (S_{PVA}%) were reported in **Table 1.9**. Both PVA hydrogels (HyD) demonstrated good swelling capacity, with HyD#2, prepared using a higher molecular weight of PVA, showing the highest swelling, consistent with its greater porosity. The symmetric cells (Hy_xSC) exhibited swelling behavior closely correlated with the water content and swelling ratios of their respective hydrogel layers (**Table 1.9**).

Sample	Wc%	S_W%	S_{PVA}%
HyD#1	71 ±2	245 ± 1	10
HyD#2	77 ±1	345 ± 9	38
Hy_1SC	65 ±2	191 ± 23	8
Hy_2SC	72 ±2	264 ± 20	29

Table 1.9: W_c%, S_w%, and S_{PVA}% results.

To evaluate the electrochemical performance, 4-point conductivity, electrochemical impedance spectroscopy (EIS), and galvanostatic charge-discharge (GCD) measurements were carried out first on the semi-cells and then

on the integrated hydrogel supercapacitors, following the procedure previously described. All experiments were performed in triplicate on three independent samples under ambient conditions (25 °C).

The conductivity of the semi-cells was influenced by two factors: the specific conductance (κ) of the Sx-GL samples, and the ionic conductivity obtained from EIS analysis of the Sx-WL samples (**Fig. 1.30**). The specific conductance is attributed to electron mobility within the conductive polymer-containing hydrogel, while the ionic conductivity (σ_c) reflects ion transport through the network. As shown in **Table 1.10**, S_1 displayed higher specific conductance than S_2. The σ_c values from EIS (**Fig. 1.30**) were consistent with the previously discussed porosity data, confirming that higher porosity enhances ion mobility. Semi-cell S_2 exhibited greater porosity and correspondingly higher ionic conductivity. Overall, the high conductivity of these gels supports efficient current flow within the electrolyte, with the three-dimensional porous architecture being key to facilitating ionic charge transport.

Semi-cell	PANI_PAMPSA amount (g)	Specific conductance κ (mS cm^{-1})	R (Ohm)	Ionic conductivity σ_c (S cm^{-1})	Specific capacitance Cp (mF g^{-1})
S_1	0.065	13.9 ± 0.4	4.41 ±0.04	0.130 ±0.001	242 ± 3
S_2	0.023	5.5 ± 0.9	1.25 ± 0.01	0.408 ±0.002	398.0 ± 0.9

Table 1.10: Electrochemical parameters of semi-cells.

The primary parameter used to assess the performance of the supercapacitor devices was the specific capacitance (Cp). Cp values for the semi-cells were determined from GCD tests conducted at a constant current density of 0.025 mA cm^{-2}, within a potential window of 0.00-0.90 V vs. SCE, over five cycles. Cp was then calculated using **equation 1.17** and summarized in **Table 1.10**. **Fig. 1.32** illustrates representative GCD profiles: **Fig. 1.32A** for S_1 and **Fig. 1.32B** comparing the third cycle of S_1 and S_2.

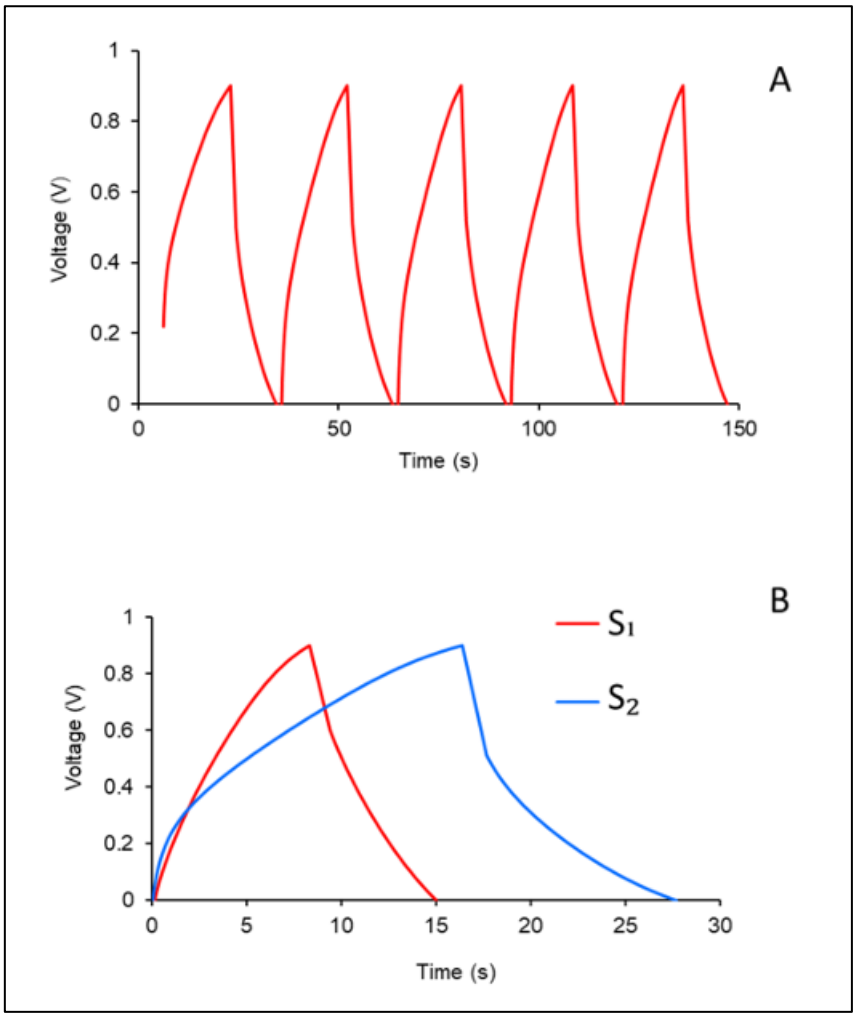

Fig. 1.32: (A) GCD curves of S1; (B) third GCD cycle comparison for S1 and S2[53].

For the Hy_xSC, the system can be modeled as two capacitances in series (**Fig. 1.33A**). The equivalent specific capacitance was derived from the reciprocal relationship of the component capacitances, with *m* representing the mass of conductive polymer incorporated into each electrode layer. Among the tested devices, Hy_2SC-fabricated using PVA of molecular weight 89,000-98,000 exhibited the most efficient interfacial charge storage, achieving the highest Cp.

$$\frac{1}{C_{eq}} = \frac{1}{C_1} + \frac{1}{C_2} + \cdots + \frac{1}{Cn} \quad \text{(where C1 = C2 = C)} \qquad \text{(equation 1.16)}$$

$$\frac{1}{C_{eq}} = \frac{2C}{C^2} = \frac{2}{C} \qquad \text{(equation 1.17)}$$

$$C_{eq} = \frac{C}{2} = C_{device}$$ (equation 1.18)

$$C_p = \frac{C_{device}}{m}$$ (equation 19)

The cycling performance (**Fig. 33B**) demonstrated stable operation, with the specific capacitance retaining 78% of its initial value after 500 cycles.

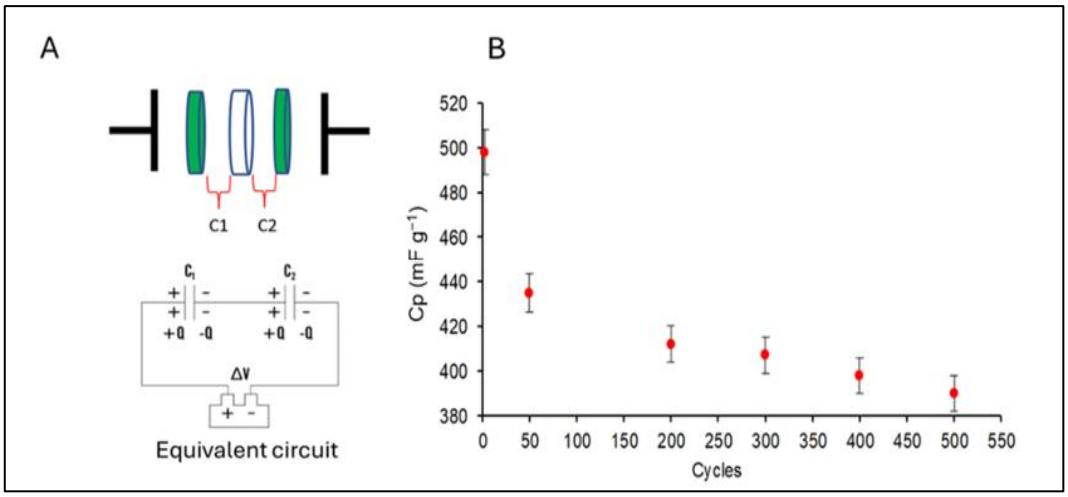

Fig. 1.33: (A) Symmetric cell assembly and equivalent circuit; (B) specific capacities vs. consecutive cycles (n = 3 tested; error bars are reported)[53].

To further improve device performance, an alternative symmetric cell was assembled using flexible Grafoil current collectors positioned on the outer electrode surfaces. In preliminary tests, two 3.0 mm Grafoil disks were inserted between the symmetric cell and the Swagelok-type electrodes (**Fig. 1.34A**). Incorporation of Grafoil increased Cp values (**Table 1.11**) and reduced the IR drop in the GCD curves (**Fig. 1.34B**). Charge–discharge measurements were also performed at higher current densities (0.1 and 0.3 mA). As summarized in **Table 1.11**, Cp decreased with increasing current density due to kinetic limitations: higher currents shorten the relaxation time available for ion redistribution, leading to reduced charge accumulation despite unchanged internal resistance.

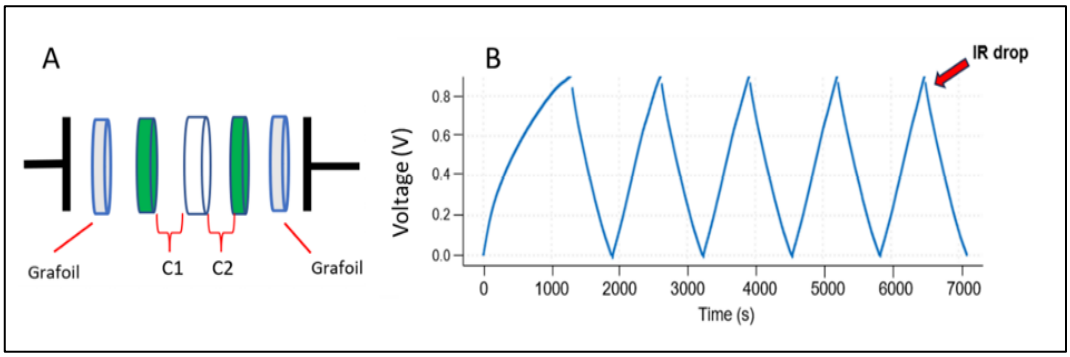

Fig. 1.34: (A) Symmetric cell assembly with Grafoil collectors; (B) GCD curves[53].

Symmetric cell	Applied current density (mA)	C_p (mF g^{-1})
	Swagelok type cell without Grafoil	
Hy_1SC	0.025	94±1
Hy_2SC	0.025	466±2
	Swagelok type cell with Grafoil	
Hy_1SC	0.025	13±3
Hy_2SC	0.025	73±1
Hy_2SC	0.1	65±1
Hy_2SC	0.3	48±2

Table 1.11: C_p values were obtained with symmetric cells with and without Grafoil.

1.8. Applications in sensor and energetic fields

1.8.1. Bio-medical sensors fabrication with PANI-modified cellulose fibers and sheets

Cell/PANI_PAMPSA devices were employed to monitor physiological signals, including heart rate and respiratory activity.

For electrocardiogram (ECG) measurements, two square Cell/PANI_PAMPSA electrodes (2.0 cm^2 each) were cut from the original A5 sheet and connected to the potentiostat using copper wires with alligator clips (**Scheme 1.6B**). Before use, the electrodes were moistened and positioned as illustrated in **Scheme 1.6A**. The ECG signal was recorded by measuring the potential difference between the electrodes over time. Care was taken to prevent direct contact between the

metallic connectors and the skin. Each measurement was repeated three times with three different electrode pairs. A representative ECG graph is reported in **Fig. 1.35**.

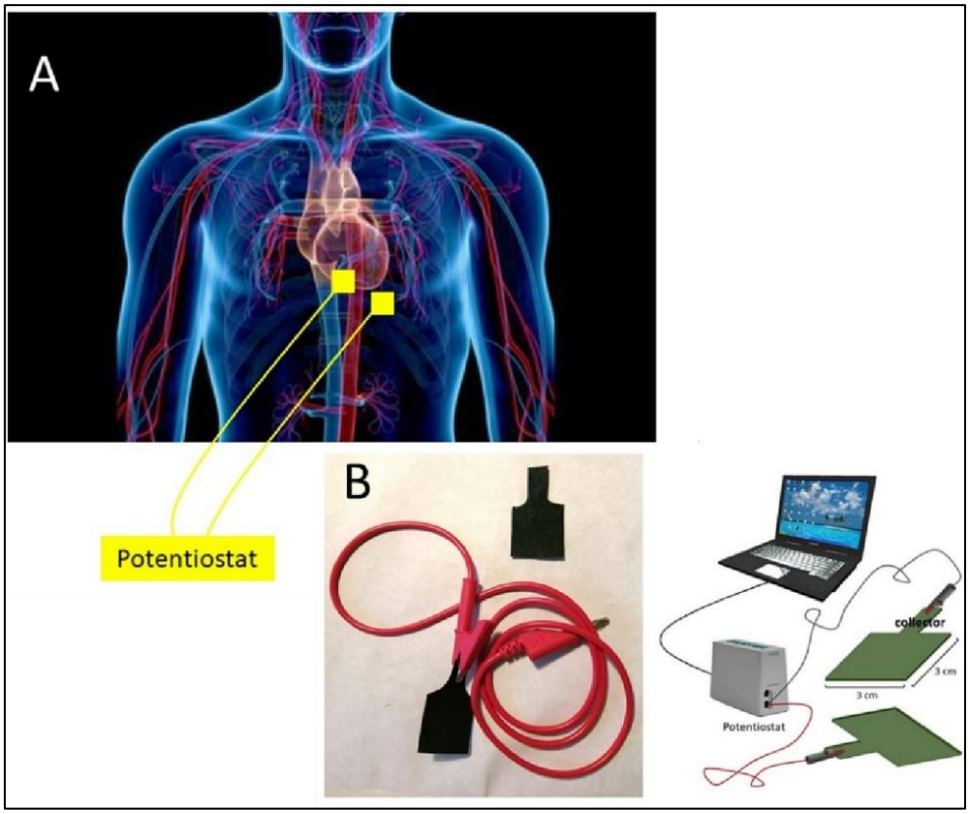

Scheme 1.6: A) Cell/PANI_PAAMPSA sensors position for EGC measurements; B) Cell/PANI_PAMPSA sensors and potentiostat connection[64].

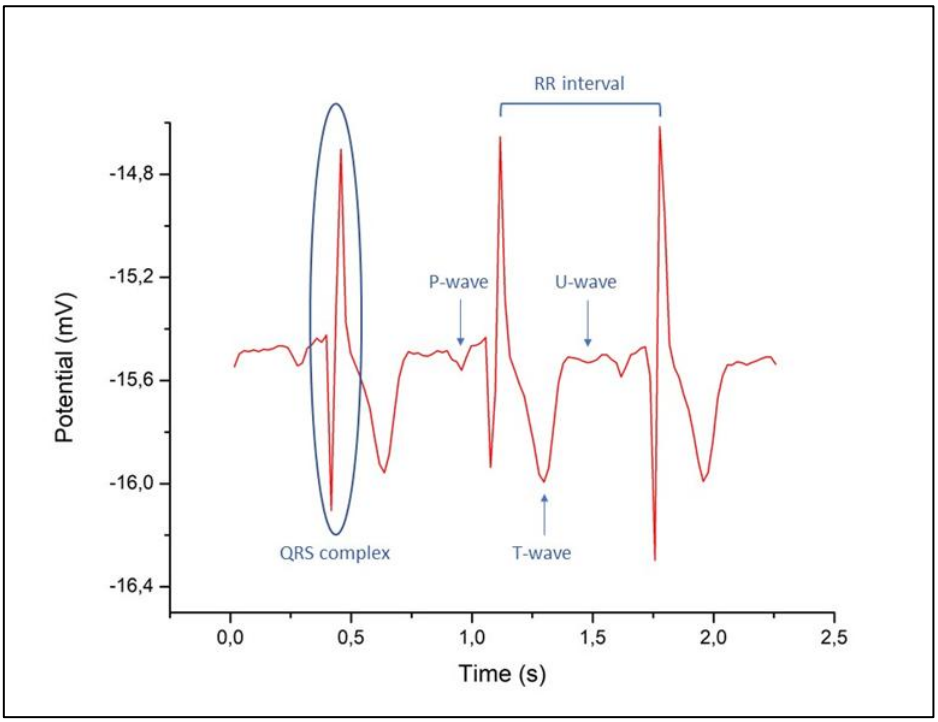

Fig. 1.34: Output ECG obtained with the Cell/PANI-PAMPSA electrodes; P wave = depolarization of the atria, QRS complex = depolarization of the ventricles, T wave = repolarization of the ventricles, RR interval = time elapsed between two successive R-waves of the QRS signal, and U wave = the last phase of ventricular repolarization[64].

For respiratory monitoring, a rectangular Cell/PANI_PAMPSA sensor (5 cm^2, 1 × 5 cm) was cut from the same A5 sheet and placed between an FFP2 and an FFP1 face mask, as shown in **Scheme 1.7**. The sensor was connected to the potentiostat via copper wires with alligator clips. Current–time responses were recorded during normal breathing while a fixed potential of 0.1 V was applied across the two ends of the sensor, with data collected at 0.1 s intervals. Each experiment was performed in triplicate using separate sensors for reproducibility **Fig. 1.35**.

Scheme 1.7: Respiratory behaviour measurements set-up**;** one of the co-workers (VDM) showing the device set-up and electronic connection for respiratory behavior[64].

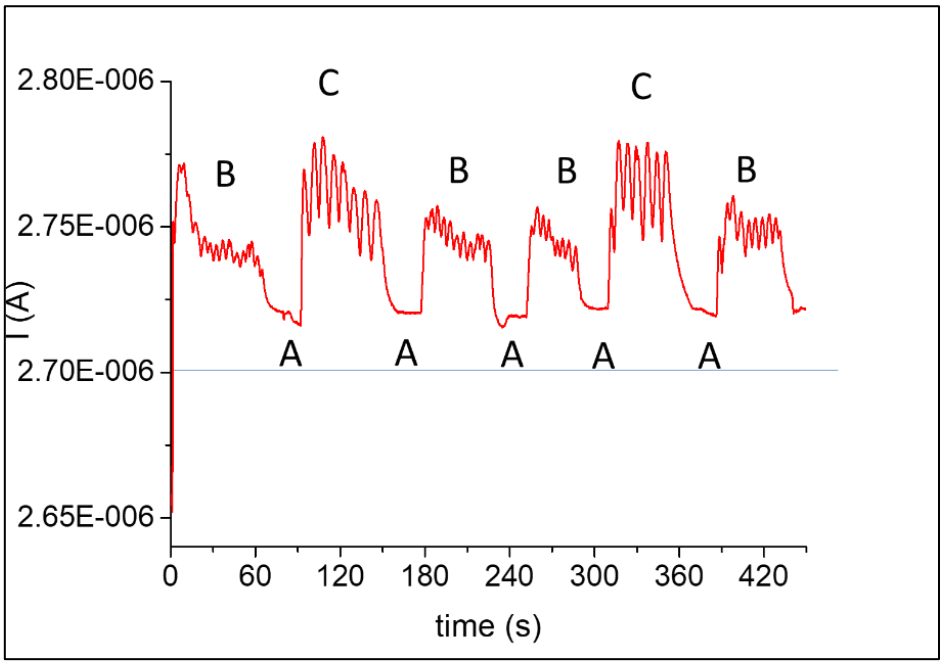

Fig. 1.35: Response curve for noise breathing rate; A) 30 s without breath; B) 60 s normal breath; C) 60 s fast breath.

1.8.2. Flexible symmetric integrated hydrogel supercapacitor

Flexible symmetric integrated hydrogel supercapacitors (FIHSC) were fabricated by interposing a 1 cm² square of symmetric hydrogel cell (previously described) between two 1.0 cm-wide Grafoil strips, as illustrated in **Fig. 1.36**. Grafoil served as the flexible current collector owing to its high conductivity. The assembly was first reinforced with transparent inert adhesive tape to improve interlayer adhesion and subsequently sealed within a transparent LDPE (low-density polyethylene) film for protection.

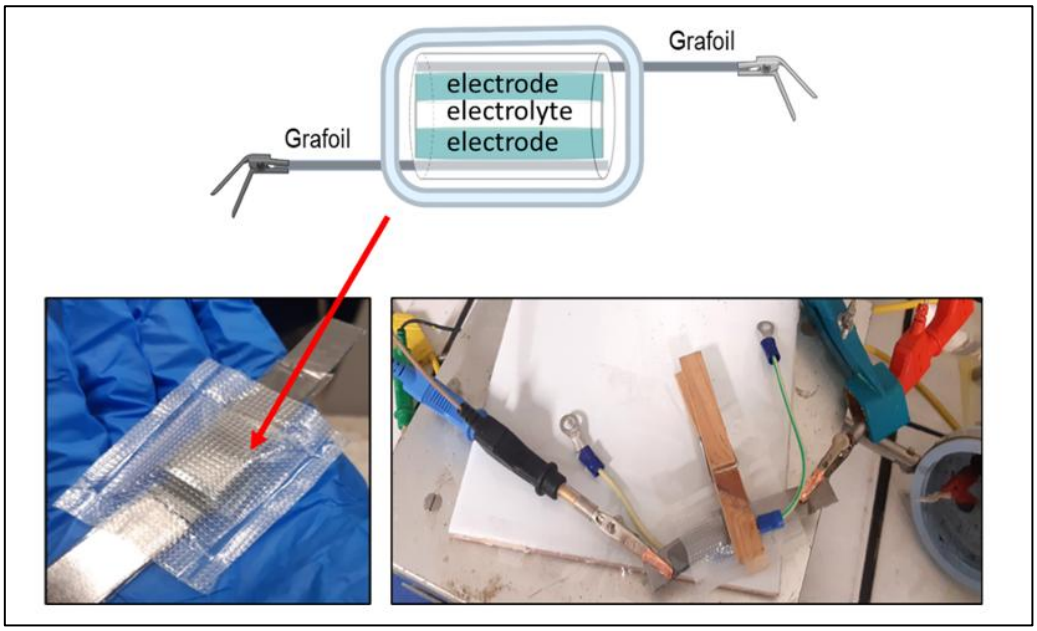

Fig. 1.36: Flexible symmetric integrated hydrogel supercapacitors (HySCs) with corresponding scheme and assembly for GCD measurements[53].

The specific capacitance (Cp) values of the FIHSC are reported in **Table 1.12** and benchmarked against PANI-based composite thin films used in both flexible and traditional supercapacitor applications[96-99]. Among the tested devices, Hy_2SC displayed higher capacitance values than Hy_1SC, consistent with selected literature reports. Although the specific capacitance of the PANI_PAMPSA composite is roughly four times lower than the best-performing traditional PANI-based supercapacitors, it should be emphasized that C_p was calculated here based on the total mass of the composite, including non-electroactive PAMPSA. This inherently lowers the apparent specific capacitance. Moreover, the gradual decrease in capacitance during cycling aligns with trends reported in recent studies. Importantly, the results in **Table 1.12** underscore that the development of all-in-one supercapacitors with electrode/electrolyte hydrogel composites represent a promising strategy for wearable energy storage devices. The hydrogel framework not only imparts high ionic conductivity and flexibility but also reduces manufacturing complexity compared to multi-component assemblies. Furthermore, the gel electrolyte mitigates risks of electrolyte leakage common in liquid-based systems, thereby improving device safety and reliability.

Symmetric cell	Capacitance (F g-1)	Retention of specific capacitance/ number of cycles	Device	Electro lyte	Refere nce
Hy1Sc	26±3	-	Flexible SC	1 M H_2SO_4	This work
Hy2SC	156±38	78%/500	Flexible SC	1 M H_2SO_4	This work
PANI	150–606	55%/1000	Traditional SC	10^{-3} M HCl[a]	92
PANI + Carbon	144–160	90%/1000	Traditional SC	1 M H_2SO_4 *	93
BP/PANI	347–424	70%/1000	Flexible electrodes	1 M H_2SO_4 *	94
PVA/PANI	571	75%/2000	Traditional SC	1 M H_2SO_4 *	91
PVA/PANI	420	93%/2000	Flexible hydrogel electrode	ATMP	95

Table 1.12: Comparison of capacitance value with data reported in the literature (* from CCD measures; BP=PANI-coated bucky paper; ATMP = trimethylene phosphonic acid.)

To demonstrate the practical applicability of Hy_xSC devices, three FIHSC were assembled and connected to power a red LED. Due to Ohmic losses in the circuit, four 100 Ω resistors were connected in series with the three Hy_2SC assemblies to achieve the operating potential required for the LED. The equivalent circuit and serially connected supercapacitors are shown in **Fig. 1.37**. The LED illumination time increased linearly with charging time up to ~80 s, after which it plateaued at the maximum storage capacity. In an alternative configuration, three FSCs were stacked in series, yielding a linear charging trend with an extended maximum

storage time of ~150 s. This stacked design required fewer resistors, highlighting its potential as a practical approach for wearable systems.

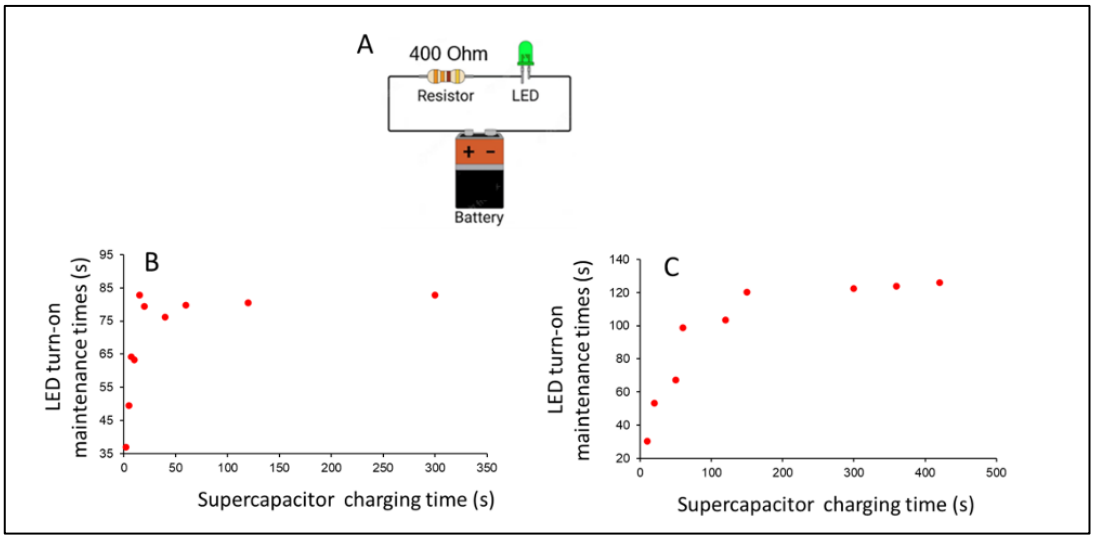

Fig. 1.37: Equivalent circuit for LED power on; (B) LED turn-on maintenance time vs. supercapacitor charging time curve obtained with three supercapacitors in series one after the other configuration; (C) LED turn-on maintenance time vs. supercapacitor charging time curve with three supercapacitors Figure 6. (A) Equivalent circuit for LED power on; (B) LED turn-on maintenance time vs. supercapacitor charging time curve obtained with three supercapacitors in series one after the other configuration; (C) LED turn-on maintenance time vs. supercapacitor charging time curve with three supercapacitors in series in overlapped[53].

The performance of Hy_2SC under mechanical deformation was further investigated by encapsulating the FIHSC in a silicone shell and evaluating capacitance during finger bending tests. Charge-discharge curves were recorded under relaxed (0°) and bent (90°) finger positions (**Fig. 1.38A**) over a voltage window of 0-0.8 V, with five cycles at 25 μA cm^{-2}. Capacitance retention after 0, 25, and 50 bending cycles is summarized in **Fig. 1.38B**. Remarkably, the device exhibited higher capacitance in the bent state, and capacitance values continued to increase with repeated bending, even after 50 cycles.

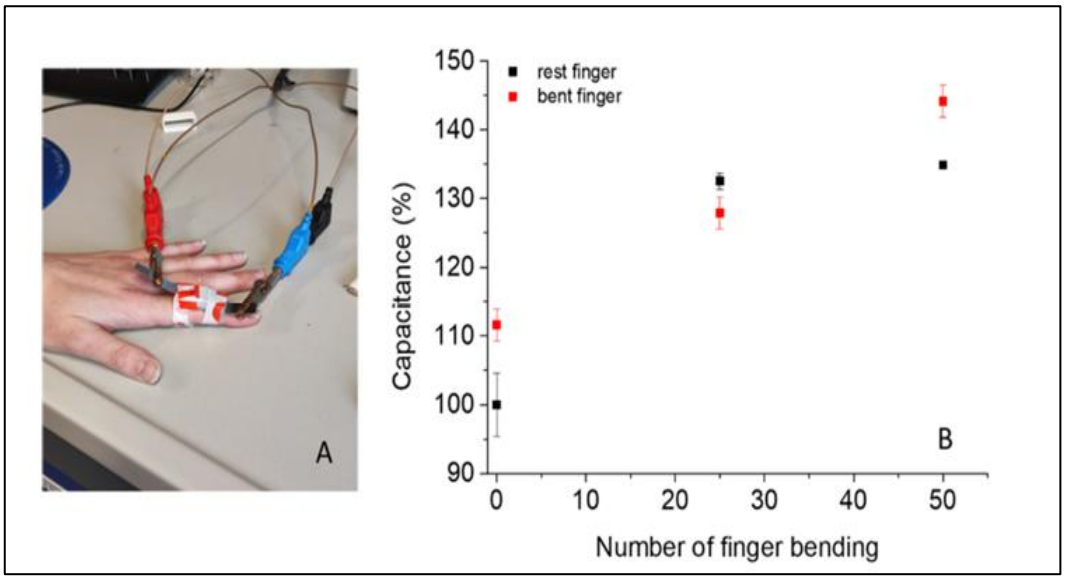

Fig. 1.38: (A) Digital image of flexible Hy_2SC attached to a resting finger and subjected to bending; (B) variation of the percentage capacitance of Hy_2SC before and after 25 and 50 repetitive and consecutive bending stimuli on a finger. Data was obtained in triplicate from three different samples[53].

This counterintuitive performance enhancement can be attributed to improved electrical contact at the electrode-gel interface during mechanical deformation. Bending compresses the hydrogel layer, reducing ion transport pathways while simultaneously increasing contact between the PANI gel and Grafoil collectors. Additionally, mechanical stress may exfoliate the flaky Grafoil structure, creating deeper and more effective electrical contacts with the PANI phase. Both effects collectively enhance charge transfer, explaining the improved electrochemical performance under deformation.

1.9. Conclusion

This Chapter highlights the potential of newly engineered paper and hydrogel-based materials for the development of biocompatible, eco-friendly, and low-cost electronic devices with broad applicability in sensing and energy storage.

The intimate modification of cellulose fibrils with polyaniline (PANI) and subsequent doping with PAMPSA proved to be an attractive strategy for producing conductive, metal-free paper sheets with enhanced mechanical resistance and biocompatibility. These Cell/PANI_PAMPSA sheets were

successfully exploited in proof-of-concept biomedical devices, including gel-free electrocardiogram electrodes and humidity sensors, the latter enabled monitoring of respiratory activity when integrated into a face mask.

Complementing these findings, PVA hydrogels were synthesized via a simple one-pot freeze-thaw method. Systematic variation of PVA molecular weight and PVA/H_2SO_4 ratio demonstrated that ionic conductivity and mechanical performance could be finely tuned, with higher PVA molecular weight promoting enhanced cross-linking, toughness, and elasticity. The self-healing properties and facile functionalization of these hydrogels further underline their suitability for flexible and durable device architectures.

Building upon this, physically cross-linked PVA hydrogels integrated with PANI_PAMPSA were employed to fabricate symmetric supercapacitor cells. The self-healing nature of PVA ensured robust interfacial contact between electrode and electrolyte layers, minimizing charge-transfer resistance. Devices incorporating Grafoil current collectors achieved specific capacitances in the order of hundreds of F g^{-1}, comparable with state-of-the-art systems. Electrochemical tests confirmed stable energy storage performance, including powering a red LED, while mechanical deformation experiments (bending and stretching) demonstrated linear and reliable capacitance responses, underscoring their versatility for wearable and biomedical applications.

Overall, the results presented here demonstrate that Cell/PANI_PAMPSA conductive sheets and PVA-based hydrogels provide complementary, sustainable platforms for the design of next-generation paper electronics, flexible supercapacitors, and biomedical sensors. Their combination of biocompatibility, recyclability, tunable conductivity, self-healing ability, and mechanical adaptability paves the way for multifunctional devices and innovative applications not yet commercially available.

1.10. Reference:

[1] J. Mort, Science, **1980**, 208, 819–825.

[2] T.A. Skotheim, R. Lelsenbaumer, J.R. Reynolds, Handbook of Conducting Polymers, Conjugated Polymers: Processing and Applications,

CRS Press, **2006**.

[3] M.J. Sailor, F.L. Klavetter, R.H. Grubbs, N.S. Lewis, Nature, **1990**, 346, 155–157.

[4] H. Shirakawa, E.J. Louis, A.G. MacDiarmid, C.K. Chiang, A.J. Heeger, J. Chem.Soc. Chem. Commun. London**, 1977**, 20, 578-580.

[5] A. G. MacDiarmid, Angew. Chem. Int. Ed**, 2001**, 40, 2581-2590.

[6] J. G. Masters, Y. Sun, A. G. MacDiarmid, and A. J. Epstein, Synth. Met., **1991**, 41, 715.

[7] A. G. MacDiarmid and A. J. Epstein, Faraday Discuss. Chem. Soc., **1989**, 88, 317.

[8] J. C. Chiang and A. G. MacDiarmid, Synth. Met., **1986**, 13, 193.

[9] W. W. Focke, G. E. Wnek, and Y. J. Wei, Phys. Chem.,**1987**, 91, 5813.

[10] K. Lee, S. Cho, S. H. Park, A. J. Heeger, C.W. Lee, and S.H. Lee, Nature (London), **2006**, 441, 65.

[11] T. Lindfors and L. Harju, Synth. Met., **2008**, 158, 233.

[12] S. K. Mondal, K. R. Prasad, and N. Munichandraiah, Synth. Met., **2005**, 148, 275.

[13] Kausor, M. A., Dhruba Chakrabortty, D., Surfaces and interfaces, **2022**, 31, 102079.

[14] O. L. Gribkova, A. A. Nekrasov, A. A. Isakova, V. F. Ivanov, A. V. Vannikov, Elektrokhimiya, **2006**, 42, 1208.

[15] T. Kobayashi, H. Yoneyama, and H. Tamura, J. Elec troanal. Chem., **1984**, 177, 293.

[16] S. Polowinski, Prog. Polym. Sci., **2002**, 27, 537.

[17] M. Gonzalez, B. G. Soares, M. Magioli, J. A. Marins, and J. Rieumont, J. SolGel Sci. Technol., **2012**, 63, 373.

[18] T. Ahuja, I.A. Mir, D. Kumar, Rajesh, Biomaterials, **2007**, 28, 791–805.

[19] H. Yao, S.H. Jenkins, A.J. Pesce, H.B. Halsall, W.R. Heineman, Clin. Chem., **1993**, 39, 1432.

[20] P.T. Kissinger, W.R. Heineman, Laboratory Techniques in Electroanalytical Chemistry, Marcel Dekker Inc, New York, NY, USA, **1996**.

[21] B.R. Eggins, Chemical Sensors and Biosensors, John Wiley & Sons, West

Sussex, England, **2002**.

[22] J. Wang, M. Musameh, Y. Lin, J. Am. Chem. Soc., **2003**, 125, 2408–2409.

[23] J. Bobacka, A. Ivaska, A. Lewenstam, Chem. Rev., **2008**, 108, 329–351.

[24] C. Chen, L. Hu, Acc. Chem. Res., **2018**, 51, 3154.

[25] H. Yuk, B. Lu, X. Zhao, Chem. Soc. Rev. **2019**, 48, 1642.

[26] S. Ling, W. Chen, Y. Fan, K. Zheng, K. Jin, H. Yu, M. J. Buehler, D. L. Kaplan, Prog. Polym. Sci. **2018**, 85, 1.

[27] C. Chen, L. Hu, Acc. Chem. Res., **2018**, 51, 3154.

[28] H. Fukuzumi, T. Saito, T. Iwata, Y. Kumamoto, A. Isogai, Biomacromolecules, **2009**, 10, 162.

[29] S. Ling, W. Chen, Y. Fan, K. Zheng, K. Jin, H. Yu, M. J. Buehler, D. L. Kaplan, Prog. Polym. Sci. **2018**, 85, 1.

[30] J. Qi, Y. Xie, H. Liang, Y. Wang, T. Ge, Y. Song, M. Wang, Q. Li, H. Yu, Z. Fan, S. Liu, Q. Wang, Y. Liu, J. Li, P. Lu, W. Chen, ACS Sustainable Chem. Eng., **2019**, 7, 9202.

[31] L. Chen, J. Y. Zhu, C. Baez, P. Kitin, T. Elder, Green Chem. **2016**, 18, 3835;

[32] W. Chen, Q. Li, Y. Wang, X. Yi, J. Zeng, H. Yu, Y. Liu, J. Li, Chem Sus Chem **2014**, 7, 154.

[33] X. Jing, H. Li, H. Y. Mi, Y. J. Liu, P. Y. Feng, Y. M. Tan, L. S. Turng, Sens. Actuator B Chem. **2019**, 295, 159.

[34] S. Chen, Y. Song, F. Xu, ACS Appl. Mater. Interfaces, **2018**, 10, 34646.

[35] X. Wang, J. Zhou, Y. Zhu, W. Cheng, D. Zhao, G. Xu, H. Yu, Chem. Eng. J., **2019,** 10, 123644.

[36] L. Zhu, X. Zhou, Y. Liu, Q. Fu, ACS Appl. Mater. Interfaces, **2019**, 11, 12968.

[37] N. Sriplai, R. Mangayil, A. Pammo, V. Santala, S. Tuukkanen, S. Pinitsoontorn, Carbohydr. Polym. **2020**, 231, 115730.

[38] S. Rajala, T. Siponkoski, E. Sarlin, M. Mettänen, M. Vuoriluoto, A. Pammo, J. Juuti, O. J. Rojas, S. Franssila, S. Tuukkanen, ACS Appl. Mater. Interfaces, **2016**, 8, 15607.

[39] L. Yang, X. Xu, M. Liu, C. Chen, J. Cui, X. Chen, K. Wu, D. Sun, Sens. Actuators B Chem., **2021**, 334, 129647.

[40] Kim, D. H., Lu, N., Ma, R., Kim, Y. S., Kim, R. H., Wang, S., Wu,

J., Won, S. M., Tao, H., Islam, A., Ki Jun Yu, K. J., Kim, T., Chowdhury, R., Ying, M., Xu, L., Li, M., Chung, H. J., Keum, H., McCormick, M., Liu, P., Zhang, Y. W., Omenetto, F. G., Huang, Y., Coleman, T., Rogers, J. A., Science, **2011,** 333(6044), 838-843.

[41] Rogers, J. A., Someya, T., Huang, Y., Science, **2010,** 327(5973), 1603-1607.

[42] Wang, K., Zhang, X., Li, C., Zhang, H., Sun, X., Xu, N., Ma, Y., J. Mater. Chem. A, **2014**,2, 19726-19732.

[43] Chen, J., Song, J., Feng, X., Polym. Bull. **2017,** 74, 27-37.

[44] Trung, T. Q., & Lee, N. E. Advanced Materials, **2016,** 28(22), 4338–4372.

[45] D'Altri, G., Yeasmin, L., Di Matteo, V., Scurti, S., Giovagnoli, A., Di Filippo, M. F., Gualandi, I., Cassani, M. C., Caretti**,** D., Panzavolta, S., Scavetta, E., Rea, M., Ballarin**,** B., . **2024,** 9, 6, 6391-6402.

[46] Liu, Y., Yang, T., Zhang, B., Williams, T., Lin, Y. T., Li, L., Zhou, Y., Lu, W., Kim, S. H., Chen, L. Q., Bernholc, J., Wang, Q., Advanced Materials, **2020** 32(15), 1906716.

[47] Zang, Y., Yang, T., Ke, H., Zhu, A., Wang, Y., Wang, J., Shen, J., Liu, G., Chen, C., Zhao, Y., Chen, H., Advanced Materials, **2015,** 27(26), 4031-4060.

[48] Lu, Y., Yang, T., Ke, H.; Zhu, A., Wang, Y., Wang, J., Shen, J., Liu, G., Chen, C., Zhao, Y., Chen, H., Applied Materials & Interfaces, **2019,** 11(42), 39524–39534.

[49] Yuan, Y., Wang, Y. Q., Zhuang, G., Li, Q., Yang, F. L., Wang, X., Journal of Materials Chemistry A, **2021** 9(22), 13047–13068.

[50] Stoppa, M., & Chiolerio, A. Sensors, **2014,** 14(7), 11957-11992.

[51] Shin, Y., Lee, H. S., Jeong, H., Kim, D. H., Wearable Electronics, **2024,** 1, 255-280.

[52] Mo, F., Lin, Y., Liu, Y., Zhou, P., Yang, J., Ji, Z., Wang, Y., Materials Science & Engineering R, **2025,** 165, 100989.

[53] Giovagnoli, A., et. el. Gels, **2024,** 10(7), 458.

[54] Simon, P., & Gogotsi, Y. Nature Materials, **2008,** 7(11), 845–854.

[55] Miller, J. R., & Simon, P. Science, **2008,** 321(5889), 651–652.

[56] Wang, K., Qin, K., Wang, T., Luo, G., RSC Advances, **2015,** 5(65), 51218–51224.

[57] Pandey, G. P., Rastogi, A. C., Westgate, C. R., Journal of Power Sources, **2014,** 245, 857–865.

[58] Sun, J. Y., Zhao, X., Illeperuma, W. R. K, Chaudhuri, O., Oh, K. H., Mooney, D. J., Vlassak, J. j., Suo, Z., Nature, **2012,** 489(7414), 133–136.

[59] Li, J., Celiz, A. D., Yang, J., Yang, Q., Wamala, I., Whyte, W., Seo, B. R., Vasilyev, N. V., Vlassak, J. J., Suo, Z., Mooney, D. J., Science, **2016,** 357(6349), 378–381.

[60] Calo, E., & Khutoryanskiy, V. V. European Polymer Journal, **2015,** 65, 252–267.

[61] Hoffman, A. S. Advanced Drug Delivery Reviews, **2012,** 64, 18–23.

[62] Yoo, J. E., Cross, J. C., Bucholz, T. L., Lee, K. S., Espe, M. P. and Loo, Y. L., J. Mater. Chem., **2007**, 17, 1268-1275.

[63] Yoo, J. E., and Bae, J., Bull. Korean Chem. Soc. **2013**, Vol. 34, No. 12.

[64] Ragazzini I. et al., Carbohydrate Polymers, **2023,** 316, 121079.

[65] Ma, W. B.; Zhu, K. H.; Ye, S. F.; Wang, Y.; Guo, L.; Tao, X. Y.; Guo, L. T.; Fan, H. L.; Liu, Z. S.; Zhu, Y. B.; Wei, X. Y., J. Mater. Sci. Mater. Electron. **2021**, 32, 20445-20460.

[66] Qin, T.; Liao, W.; Yu, L.; Zhu, J.; Wu, M.; Peng, Q.; Han, L.; Zeng, H., J. Polym. Sci. **2022**, 60, 2607-2634.

[67] Angelopoulos, M., Patel, N., Shaw, J. M., Labianca, N. C., Rishton, S. A. J. Vac. Sci. Technol., B, **1993**, 11, 2794-2797.

[68] Sun, L., Liu, H., Clark R., Yang, S. C., Synth. Met., **1997**, 84, 67-68.

[69] Gribkova, O., Omelchenko, O., Trchová, M., Nekrasov, A., Ivanov, V., Tverskoy,V., Vannikov, A., Chemical Papers, **2013,** 67 (8) 952-960.

[70] Shen, J., Xie, Y., Liu, Z., Zhang, S., Wang, Y., Jia, L., Wang, Y., Cai, Z., Ma, H., Xiang, M., Journal of Molecular and Cellular Cardiology, **2018,** 122, 140-151.

[71] Heller, A., Feldman, B. J., Mano, N., Loo, Y. L.,(**2016**). Lawyer electron conducting crosslinked polyaniline based redox hydrogel, and method of making (Patent, US 9,303.279 B2).

[72] Pang, Z., Yildirim, E., Pasquinelli, M. A., Wei, Q., Colloids and Surfaces A: Physicochemical and Engineering Aspects, **2016,** 494, 248–255.

[73] Rahayu, I., Eddy, D. R., Novianty, A. R., Rukiah, Anggreni, A., Bahti, H.,

Hidayat, S., IOP Conference Series: Materials Science and Engineering, **2019,** 509(1)

[74] Nepomuceno, N. C., et al., Journal of Solid State Chemistry, **2021,** 302(June), 122372.

[75] Wang, J., Su, W., Zhang, J., Zhou, A., Bai, H., & Zhang, T. Science China Materials, **2021,** 64(3), 571-580.

[76] Seshadri, D. R., Li, R. T., Voos, J. E., Rowbottom, J. R., Alfes, C. M., Zorman, C. A., Drummond, C. K., Npj Digital Medicine, **2019,** 2(1).

[77] Heikenfeld, J., Jajack, A., Rogers, J., Gutruf, P., Tian, L., Pan, T., Li, R., Khine, M., Kim, J., Wang, J., & Kim, J., Lab on a Chip, **2018,** 18(2), 217-248.

[78] Ricciardi, R.; Auriemma, F.; Gaillet, C.; De Rosa, C.; Lauprêtre, F., Macromolecules **2004**, 37, 9510-9516.

[78] Hassan, C. M.; Peppas, N. A., Macromolecules **2000**, 33, 2472-2479.

[79] Ricciardi, R.; Auriemma, F.; De Rosa, C.; Lauprêtre, F., Macromolecules **2004**, 37, 1921-1927.

[80] Holloway, J. L.; Lowman, A. M.; Palmese, G. R., Soft Matter **2013**, 9, 826-833.

[81] Alipoori, S.; Torkzadeh, M. M.; Mazinani, S.; Aboutalebi, S. H.; Sharif, F., *Appl. Sci.* **2021**, 3, 1-13.

[82] Reguieg, F.; Ricci, L.; Bouyacoub, N.; Belbachir, M.; Bertoldo, M., *Polym. Bull.* **2020**, 77, 929-948.

[83] Gomaa, M. M.; Hugenschmidt, C.; Dickmann, M.; Abdel-Hady, E. E.; Mohamed, H. F. M.; Abdel-Hamed, M. O., *Phys. Chem. Chem. Phys.* **2018**, 20, 28287-28299.

[84] Scurti, S.; Ortolani, J.; Ghirri, A.; Maccaferri, E.; Caretti, D.; Mazzocchetti, L., *Prog. Org. Coatings* **2023**, 177, 107457.

[85] Paranhos, C. M.; Soares, B. G.; Oliveira, R. N.; Pessan, L. A., Macromol. Mater. Eng. **2007**, 292, 620– 626

[86] Zhang, L.; Wang, Z.; Xu, C.; Li, Y.; Gao, J.; Wang, W.; Liu, Y., J. Mater. Chem. **2011**, 21, 10399– 10406.

[87] Tanpichai, S.; Oksman, K., Compos. Part A Appl. Sci. Manuf. **2016**, 88, 226– 233.

[88] Mecca, T.; Ussia, M.; Caretti, D.; Cunsolo, F.; Dattilo, S.; Scurti, S.; Privitera, V.; Carroccio, S. C., Chem. Eng. J. **2020**, 399, 125753.

[89] Liu, Y.; Hsu, S. H., Front. Chem. **2018**, 6, 1-10.

[90] Wang, W.; Xiang, L.; Gong, L.; Hu, W.; Huang, W.; Chen, Y.; Asha, A. B.; Srinivas, S.; Chen, L.; Narain, R.; Zeng, H. Injectable, Chem. Mater. **2019**, 31, 2366-2376.

[91] Anupama Devi, V. K.; Shyam, R.; Palaniappan, A.; Jaiswal, A. K.; Oh, T. H.; Nathanael, A. J., Polymers **2021**, 13, 3782.

[91] Liu, C.; Li, F.; Ma, L.-P.; Cheng, H.-M., Adv. Mater. **2010**, 22, E28-E62.

[92] Shin, M.; Shin, S. H.; Lee, M.; Kim, H. J.; Jeong, J. H.; Choi, Y. H.; Oh, D. X.; Park, J.; Jeon, H.; Eom, Y., Polymer. **2021**, 229, 123969.

[93] Shen, J.; Shahid, S.; Amura, I.; Sarihan, A.; Tian, M.; Emanuelsson, E. A., Synth. Met. **2018**, 245, 151-159.

[94] Nunes, R. W.; Martin, J. R.; Johnson, J. F., Polym. Eng. Sci. **1982**, 22, 205-228.

[95] Patil, D.S.; Shaikh, J.S.; Dalavi, D.S.; Kalagi, S.S.; Patil, P.S., Mater. Chem. Phys. **2011**, 128, 449-455.

[96] Ghenaatian, H.R.; Mousavi, M.F.; Kazemi, S.H.; Shamsipur, M., Synth. Met. **2009**, 159, 1717-1722.

[97] Chen, W.C.; Wen, T.C., J. Power Sources **2003**, 117, 273-282.

[98] Meng, C.; Liu, C.; Fan, S., *Electrochem. Commun* **2009**, 11, 186-189.

[99] Dou, P.; Liu, Z.; Cao, Z.; Zheng, J.; Wang, C.; Xu, X., J. Mater. Sci. **2016**, 51, 4274-4282.

Chapter 2: Activated carbon-based cathode and polymeric membrane for Li-O_2 battery

Index

2.1. Introduction

Li-O_2 batteries belongs to the broad range of metal-oxygen batteries, where metal electrodes (e.g. Li, Na, Zn) are used as anode and atmospheric air is the cathode material. Although significant progress has been achieved in the last years, there are still many challenges to overcome in order to reach the final commercialization of Li-O_2 batteries. Lithium-oxygen (Li-O_2) batteries have extremely high theoretical energy density, potentially rivalling that of gasoline (up to 3500 Wh/kg)[1]. This surpasses the energy density of conventional lithium-ion batteries by an order of magnitude, making Li-O_2 systems ideal candidates for electric vehicles (EVs), portable electronics, and grid storage. Li-O_2 batteries operate through the reversible redox reaction of lithium metal with atmospheric oxygen, forming lithium peroxide (Li_2O_2) during discharge and decomposing it during charge[2]. However, practical implementation remains hindered by several critical challenges, including poor cycle life, low round-trip efficiency, electrode degradation, and instability of electrolytes and air cathodes in the presence of oxygen and its reactive intermediates such as superoxide and peroxide species[3].

Li-O_2 batteries are categorized into four types based on their electrolyte phase: aqueous, aprotic, hybrid, and solid-state. Among these, aprotic systems are the most extensively studied due to their relatively higher energy densities and the feasibility of Li_2O_2 formation[4]. Yet, there are issues such as dendrite growth on lithium metal anodes, parasitic side reactions, limited oxygen solubility, and clogging of the porous cathode with discharge products persist. Strategies to address these challenges include the development of stable solid or gel polymer electrolytes, bifunctional oxygen catalysts, protective anode coatings, and cathodes with high porosity and catalytic activity. Additionally, understanding the reaction mechanism-whether the Li_2O_2 forms via a solution-mediated or surface-mediated pathway-is vital for optimizing performance and design[5].

Recent advances in in-situ characterization methods, such as X-ray diffraction (XRD), transmission electron microscopy (TEM) and Raman spectroscopy have provided new insights into the morphology and crystallinity of discharge products and degradation pathways[6]. Furthermore, novel cathode architectures employing graphene, carbon nanotubes, and transition metal oxides have demonstrated improvised capacity and cyclability. However, significant progress is still required

to make Li-O_2 batteries commercially viable. Breakthroughs in stable, non-volatile, and oxygen-permeable electrolytes as well as protective lithium hosts that suppress dendrite formation are key to unlocking their potential[7,8].

On the other hand, membranes play a critical role in Li-O_2 batteries, serving functions that extend beyond simple ionic conduction to include protection of the lithium anode, control of gaseous species ingress (such as H_2O or CO_2), and mitigation of parasitic reactions. Oxygen-selective membranes (OSMs) have been studied to allow O_2 diffusion while blocking water vapor, thereby reducing anode corrosion under ambient air exposure[9]. The membranes can be divided into two categories: passive membranes, which have a physical barrier effect, and the active membranes that hinder the passage of molecules providing a chemical barrier. The former feature barrier to the diffusion process, while the latter have a direct interaction with the molecules. It is essential to define the positioning of this membrane in the cell also according to the purpose for which they are intended. Composite single-ion conductor membranes have also been developed (e.g. modified PVDF membranes doped with inorganic fillers) which permit Li^+ transfer while preventing undesired species from crossing, significantly improving cycle life and rate performance in Li-O_2 cells[10]. Key membrane design parameters include ionic conductivity, thickness, chemical stability in both oxidizing and reducing environments, permeability (to O_2, moisture, electrolyte solvents), mechanical robustness, and interfacial compatibility with electrodes. Strategies such as tailoring pore structure, using ceramic or glass-ceramic layers, and integrating selective functional groups have shown promise. Despite progress, challenges remain in balancing O_2 selectivity with Li^+ transport, suppressing side-reactions at the membrane interface, and ensuring membrane durability over many cycles. Advances in membrane materials could thus be pivotal in realizing high-energy, stable, and practical Li-O_2 battery systems.

In conclusion, while Li-O_2 (**Fig. 2.1 & 2.2**) batteries present an attractive energy storage solution due to their high theoretical energy density, realizing a practical, long-life, and safe battery requires overcoming formidable technical barriers. Multidisciplinary research efforts focusing on materials science, electrochemistry, and system engineering are essential for bringing Li-O_2 technology closer to commercialization[11].

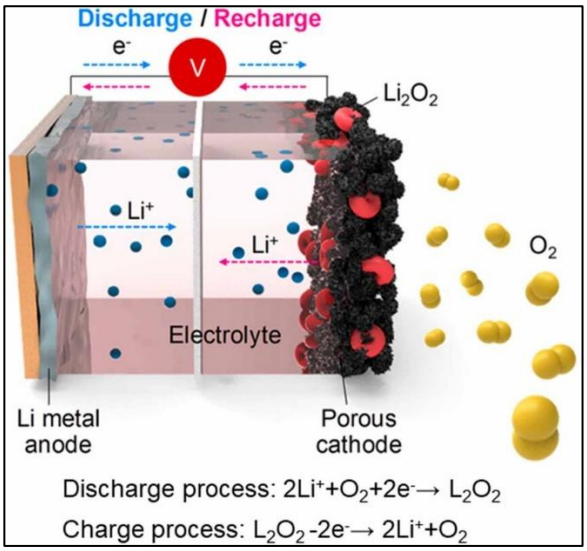

Fig. 2.1: Schematic presentation of Li-O_2 battery[12].

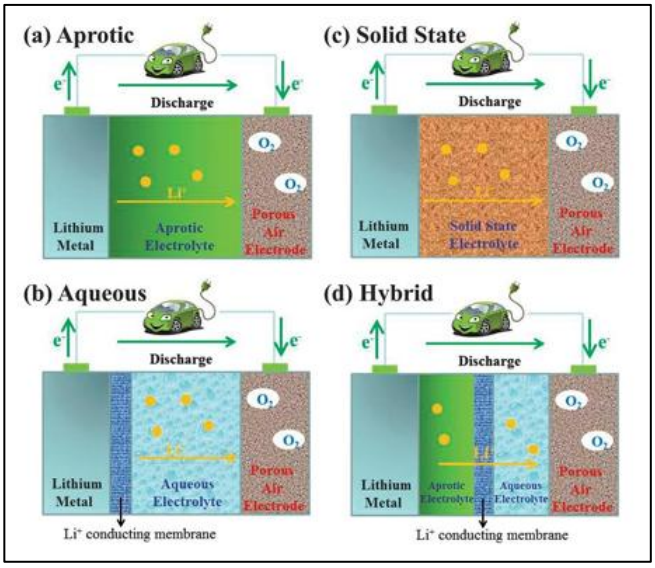

Fig. 2.2: Classification of Li-O 2 batteries.

2.2. State-of-the-art of Li-O_2 battery

The Li-O_2 battery, consisting of metallic lithium as the anode (negative electrode), oxygen from air as the cathode active material, and a Li^+-Li-containing electrolyte, is among the most extensively studied metal-air battery systems. In these cells, the cathode is typically a porous, electronically conductive matrix that allows electrochemical interaction between gaseous O_2 and Li^+ ions in the electrolyte[13].

During discharge and charge, the battery operates through lithium dissolution/deposition at the anode and the oxygen reduction (ORR) and oxygen evolution (OER) reactions at the cathode, as illustrated in **Fig. 2.1**. On discharge, lithium metal at the anode is oxidized, releasing Li^+ into the electrolyte. This process reverses upon charging. At the cathode, O_2 from the atmosphere diffuses into the porous structure, dissolves in the electrolyte, and undergoes reduction. In the presence of a suitable non-aqueous electrolyte, superoxide (O_2^{2-}) is formed, which reacts with Li^+ to produce lithium peroxide (Li_2O_2). This Li_2O_2 precipitates on the cathode surface as the main discharge product and is decomposed back into O_2 during charging[14]:

$$2Li^+ + O_2 + 2e^- \leftrightarrow Li_2O_2 \qquad \Delta E^0 = 2.96\ V \qquad \text{(equation 2.1)}$$

Some studies suggest that discharge can proceed further to lithium oxide (Li_2O), increasing energy storage capacity, though this reaction is much harder to reverse during charging.

In the simplest model of a non-aqueous Li-O_2 cell, assuming the cathode consists solely of Li_2O_2 (with no carbon, binder, or porosity) and a stoichiometric amount of Li at the anode, the theoretical specific energy and energy density reach 3,505 Wh kg^{-1} and 3,436 Wh L^{-1}, respectively[15]. Introducing excess lithium metal at the anode to account for cycling losses lowers these values; for example, with a threefold excess (n = 4), the specific energy and energy density become 1,800 Wh kg^{-1} and 1,290 Wh L^{-1}.

Accounting for cathode porosity, let us consider a structure where 20% of the volume is carbon, 20% is electrolyte, and 60% is Li_2O_2 at the end of discharge. In this case, a porous cathode coupled with a stoichiometric Li anode provides a benchmark for the maximum theoretical energy storage, assuming an electrolyte thickness of 10 μm[16]. A comparison with Li-ion batteries is also shown. Bars outlined in green represent values for Li_2O_2, while those in orange correspond to Li_2O. These results demonstrate that, even when considering lithium excess and cathode porosity, the energy performance of Li-O_2 batteries significantly surpasses that of today's Li-ion systems.

2.3. Activated carbon-based aerogels as Li-O_2 cathode

Activated carbon-based aerogels have emerged as promising cathode materials for non-aqueous Li-O_2 batteries due to their high surface area, tunable porosity, and excellent electronic conductivity. The unique three-dimensional interconnected structure of carbon aerogels provides abundant active sites for oxygen reduction and facilitates efficient diffusion of O_2 and Li^+ ions within the cathode. This architecture also accommodates the deposition of discharge products, mainly lithium peroxide (Li_2O_2), thereby mitigating pore clogging and improving reversible capacity. Moreover, the intrinsic meso-/macroporous framework of aerogels enhances electrolyte accessibility, reduces transport limitations, and enables more uniform Li_2O_2 growth during cycling. However, challenges remain in controlling parasitic reactions arising from the high reactivity of carbon with reactive oxygen intermediates, which can compromise cycle life[17,18,19]. Recent studies have focused on surface functionalization, heteroatom doping, and the integration of catalytic nanoparticles into activated carbon aerogels to improve ORR/OER kinetics and suppress side reactions. These strategies significantly enhance round-trip efficiency and durability compared to conventional porous carbons. Overall, activated carbon-based aerogels represent a versatile platform for tailoring Li-O_2 cathodes, combining lightweight structure with electrochemical performance, and offer a pathway toward practical high-energy rechargeable metal–air systems. In the present work, a simple and sustainable approach was employed to prepare different activated carbon self-standing cathodes for Li-O_2 batteries. In this context, the design of porous carbon-based architectures is crucial, as the interconnected pore network helps to accommodate discharge products, facilitates oxygen diffusion, and ensures efficient electrolyte penetration. Finally, the influence of surface area and pore size distribution of the activated carbon cathodes on their electrochemical behaviour in Li-O_2 batteries is systematically investigated and discussed[20].

2.4. Pullulan as a separator and membrane

The study on investigating and comparing the permeability of several candidate materials for use as Li-air battery membranes[21,22]. In particular, the work focused on membranes fabricated by electrospinning Nylon, cellulose, and pullulan. Pullulan was selected due to its excellent mechanical strength, oxygen

impermeability, and hydrophilic nature. Pullulan is an exopolysaccharide derived from starch by *Aureobasidium pullulans*, consisting of repeating maltotriose units, which endow it with outstanding film- and fiber-forming capabilities. These properties have led to its widespread use in pharmaceutical and biomedical applications, and more recently, in electrochemical energy storage systems such as supercapacitors, as a binder or separator.

2.5. Activated carbon (AC) based electrodes preparation

Materials: Activated carbon(AC) (Honeywell); Poly (ethylene oxide) (PEO) M.W. 100,000 (Aldrich); PTFE (60% wt. dispersion); Tetra ethylene glycol dimethyl ether (TEGDME) (Thermo Fisher); LiTFSI (Sigma-Aldrich); Lithium iron phosphate (LFP) (Aleees); 1-butyl-1-methylpyrrolidium bis-(trifluoromethanesulfonyl)-imidi (PYR); TTH (organic redox active molecule from University of Bari), Pullulan (Thermo Fisher); Glycerol; Commercial PE-PP-PE membrane (Celgard).

Self-standing electrode preparation: Different composition of materials was prepared to obtain a higher capacity of Li-O_2 battery (**Table 2.1**) and the most effective compositions were numbers 5 and 6 are described below:

Composition number	Name	Material	Used ratio
1	CN1	AC : PTFE	9 : 1
2	CN2	AC : LFP : PTFE	9 : 9 : 2
3	CN3	AC : PTFE : PEO : PYR	9 : 1 : 1 : 5
4	CN4	AC : PTFE : PEO : PYR	9 : 1 : 2 : 5
5	CN5	AC : PTFE : PEO : PYR	9 : 1 : 1 : 0.5
6	CN6	AC : PTFE : PEO : PYR + (2 millimolar TTH)	9 : 1 : 1 : 0.5 + (2 millimolar TTH)

Table 2.1: Composite electrode compositions.

CN5 electrode preparation: A total of 100 mg of PEO (molecular weight: 100,000) was dissolved in 10 mL of ethanol under magnetic stirring at 60 °C until the polymer was completely dissolved, which required approximately 15-20 minutes. Subsequently, 50 mg of PYR was added to the solution and stirred for an additional 5 minutes. After that, 900 mg of activated charcoal was introduced and the mixture was stirred for another 5 minutes. Following this, 100 mg (equivalent to 160 mg of a 60% suspension) of PTFE solution was added to the reaction mixture. The solution was stirred continuously until most of the ethanol evaporated, and a jelly-like substance was obtained. This jelly-like substance was then homogenized using a spatula and glass tube, spread evenly, and electrodes with a diameter of 16 mm (φ16) were cut from it (**Fig. 2.3**). Finally, the electrodes were dried at 80 °C overnight in an oven, followed by additional drying at 60 °C under vacuum in a Buchi system for 2-3 hours.

$$Active\ mass\ of\ electrode = mass\ of\ electrode * \frac{18}{23} \qquad \text{(equation 2.2)}$$

Fig. 2.3: Self-standing porous AC electrodes

CN6 electrode preparation: A total of 42.12 mg of PEO (molecular weight: 100,000) was dissolved in 5 mL of ethanol under magnetic stirring at 60 °C until the polymer was completely dissolved, which required approximately 15-20 minutes. Next, 21.06 mg of PYR was added to the solution and stirred for an additional 5 minutes. This was followed by the addition of 107 mg of TTH, and the mixture was stirred for another 5 minutes. Subsequently, 373.37 mg of activated charcoal was introduced and stirred for 5 minutes. After that, 67.57 mg (equivalent to 160 mg of a 60% suspension) of PTFE solution was added to the

reaction mixture. Stirring was continued until most of the ethanol evaporated and a jelly-like substance was obtained. The jelly-like substance was then homogenized using a spatula and a glass tube, spread evenly, and electrodes with a diameter of 16 mm (φ16) were cut from it. Finally, the electrodes were dried at 80 °C overnight in an oven, followed by additional drying at 60 °C under vacuum in a Buchi system for 2-3 hours.

$$Active\ mass\ of\ electrode = mass\ of\ electrode * \frac{63.75}{100} \quad \text{(equation 2.3)}$$

Electrolyte preparation: 1 M LiTFSI in TEGDME was prepared and used for all battery testing.

Coin-cell designing: In the initial phase of testing, commercial coin cells equipped with a grid on the large cap side were employed. However, these cells demonstrated suboptimal electrochemical performance, likely due to limitations in oxygen diffusion across the grid structure. To address this issue, a customized coin-cell configuration was subsequently developed and utilized for all subsequent measurements (**Fig. 2.4**). In this design, a laser-induced perforation with a diameter of 0.25 mm was introduced into the large cap. The purpose of this modification was to provide a more controlled and efficient oxygen ingress pathway, thereby enhancing the cathode's accessibility to oxygen during operation. The customized configuration not only improved the uniformity of oxygen distribution within the cell but also contributed to more stable discharge behaviour, making it more suitable for reproducible electrochemical measurements in Li-O_2 systems.

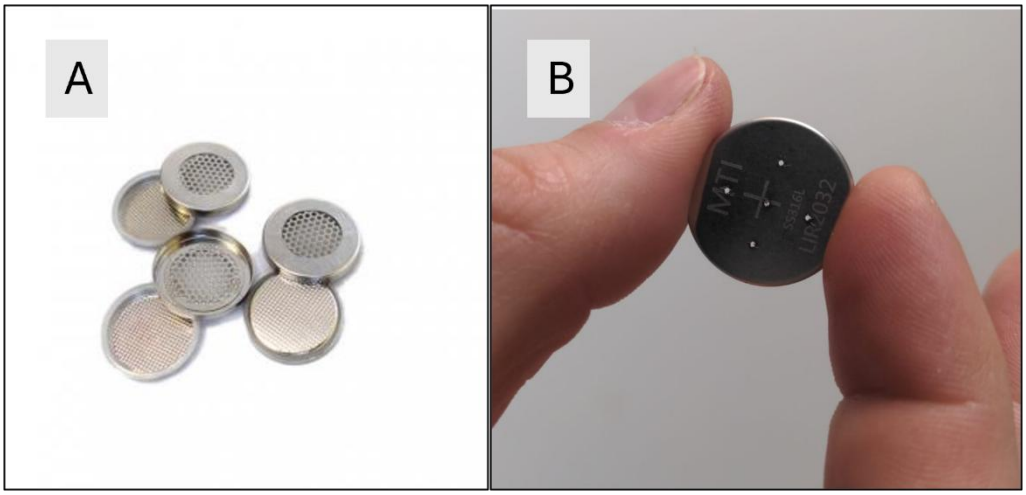

Fig. 2.4: (A) commercial coin cell with grid and (B) coin cell with LASER induced holes.

Pullulan membrane preparation: Membranes with different compositions (**Table 2.2**) were prepared as follows. Pullulan, glycerol, water, and LiTFSI were first mixed under sonication at 60 °C until a homogeneous solution was obtained. The resulting mixture was then cast onto a Mylar substrate using a doctor blade technique. The cast films were initially dried at room temperature for 2 h, followed by further drying in an oven at 60 °C for 4 h. Finally, the membranes were subjected to vacuum drying in a Buchi system at 60 °C for overnight to ensure complete removal of residual solvent (**Fig. 2.5**). Later these membranes were compared with commercial PE-PP-PE separator and further experiments were done with M4, since it has the best ionic conductivity.

Composition number	Name	Material	Used ratio
1	M1	(Pullulan : glycerol) + LiTFSI	(1 : 1) + 5% wt.
2	M2	(Pullulan : glycerol) + LiTFSI	(1 : 1) + 10% wt.
3	M3	(Pullulan : glycerol) + LiTFSI	(1 : 2) + 5% wt.
4	M4	(Pullulan : glycerol) + LiTFSI	(1 : 2) + 10% wt.

Table 2.2: Different compositions of pullulan membrane.

Fig. 2.5: Pullulan membrane.

2.6. Characterization of AC-based Li-O_2 battery

Coin-cell assembly: To provide a detailed account of the procedure followed for assembling the electrochemical cell used in the durability test, the description below focuses on the physical assembly of the electrodes rather than their preparation. The fundamental components of the cell include: two lids ("caps") used to seal the cell; a spring, which maintains constant pressure and ensures proper contact among the anode, electrolyte, and cathode; a spacer, which helps maintain the correct distance between electrodes and contributes, together with the spring, to cell sealing; a lithium metal sheet serving as the anode; an activated carbon self-standing electrode serving as the cathode; and a separator that prevents direct electrical contact between the electrodes**.** For the assembly of Li-O_2 coin cells, various configurations were employed to optimize electrochemical performance (**Table 2.3**). A commercial PP-PE-PP separator was used in all tests. Before cell assembly, the separator was soaked in 1 M LiTFSI dissolved in TEGDME for 2 hours to ensure complete electrolyte impregnation.

Cell assembly type	Cell assembly sequence
T1	Small Cap + Spring + Spacer + Li + Soaked Separator + 1 M LiTFSI + Dry AC electrodes + Big Cap
T2	Small Cap + Spring + Spacer + Li + Soaked Separator + Dry AC electrodes + Big Cap
T3	Small Cap + Spring + Spacer + Li + Soaked Separator + Soaked AC Electrode + Dry AC electrodes + Big Cap
T4	Small Cap + Spring + Spacer + Li + Soaked Separator + Soaked Pressed AC Electrode + Dry Pressed AC electrodes + Big Cap
T5	Small Cap + Spring + Spacer + Li + Soaked Separator + 1 M LiTFSI + Dry Pressed AC electrodes + Big Cap
T6	Small Cap + Spring + Spacer + Li + 1 M LiTFSI + Soaked Separator + Dry Pressed AC electrodes + Big Cap

T7	Small Cap + Spring + Spacer + Li + Soaked Separator +Soaked Pressed electrode + Dry Non-Pressed AC electrodes + Big Cap
T8	Small Cap + Spacer + Li + 1 M LiTFSI + Soaked Separator + Dry AC electrodes + Big Cap
T9	Small Cap + Spacer + Li + 1 M LiTFSI + Soaked Separator + Dry AC electrodes + Big Cap

Table 2.3: Li-O_2 cell configurations.

Among all the tested configurations, **T9** (**Fig. 2.6**) exhibited the best electrochemical performance, and subsequent cell evaluations were carried out using this configuration.

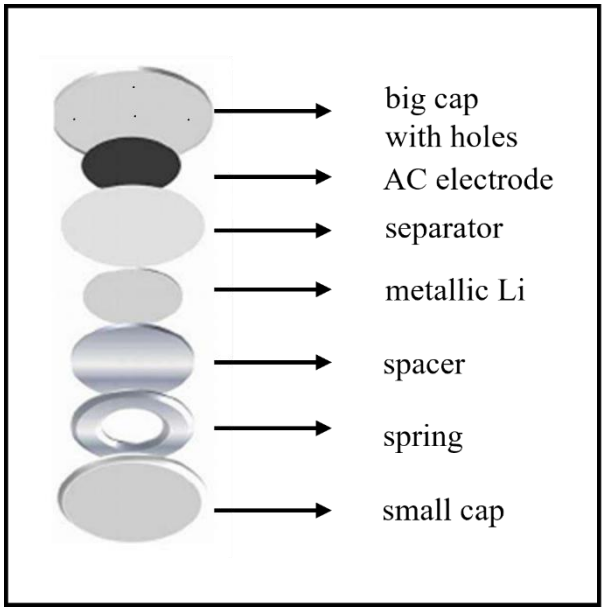

Fig. 2.6: Schematic representation of T9 coin cell.

In T9 coin cell configuration, different amount of electrolyte has significant effect on cell performance.

Coin cell testing: Cell capacity was measured by discharging each cell using a VSP BioLogic potentiostat under a constant current of 0.190 mA (**Fig. 2.7**). All tests were conducted at ambient temperature.

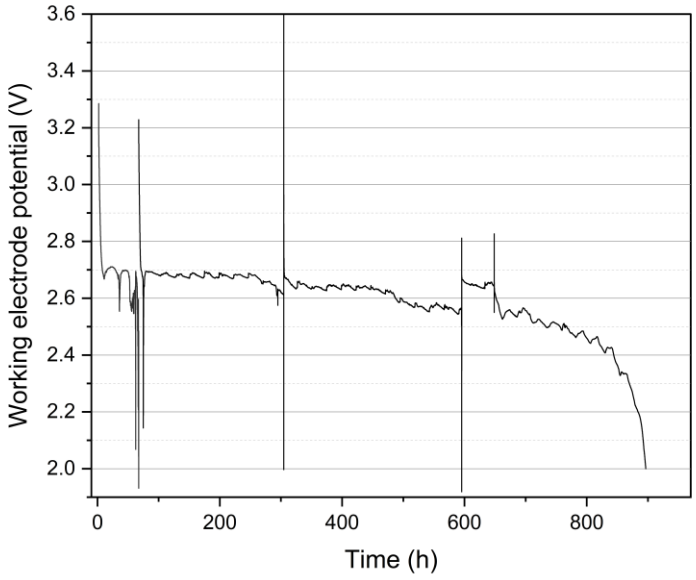

Fig. 2.7: Coin cell discharge profile.

During discharge measurements of Li-O_2 cells, temperature and electrolyte volume (**Table 2.4**) and presence of TTH molecule were (**Table 2.5**) identified as critical parameters that strongly influenced overall cell capacity. Oscillations observed in the discharge profiles were attributed to fluctuations in ambient temperature between day and night. Specifically, higher daytime temperatures led to an increase in cell potential, whereas lower nighttime temperatures resulted in a decrease in potential.

Amount of 1 M electrolyte	Cell capacity (mAh)
50 µL	12.46
75 µL	23.33
100 µL	60.8
150 µL	169.96

Table 2.4: Influence of electrolyte on cell capacity.

Composition number	Cell capacity (mAh)
CN5	169.96
CN6	1334.18

Table 2.5: Influence of TTH on cell capacity.

Postmortem analysis: After the coin cells were fully discharged, they were sealed under vacuum and stored for several days before post-mortem analysis. The cells were then carefully opened, and the used electrodes as well as the separator were imaged using a **Max-see digital microscope**. Upon inspection, a distinct white passivation layer was observed on the surface of the lithium anode facing the separator, while the underlying lithium metal retained its characteristic shiny appearance, indicating incomplete consumption of the metallic Li. The cathode was found to be completely saturated with electrolyte, whereas no residual electrolyte remained in the reservoir region (spring + spacer). These observations suggest significant electrolyte redistribution during cycling, accompanied by interfacial passivation processes at the lithium surface (**Fig. 2.8 & Fig. 2.9**).

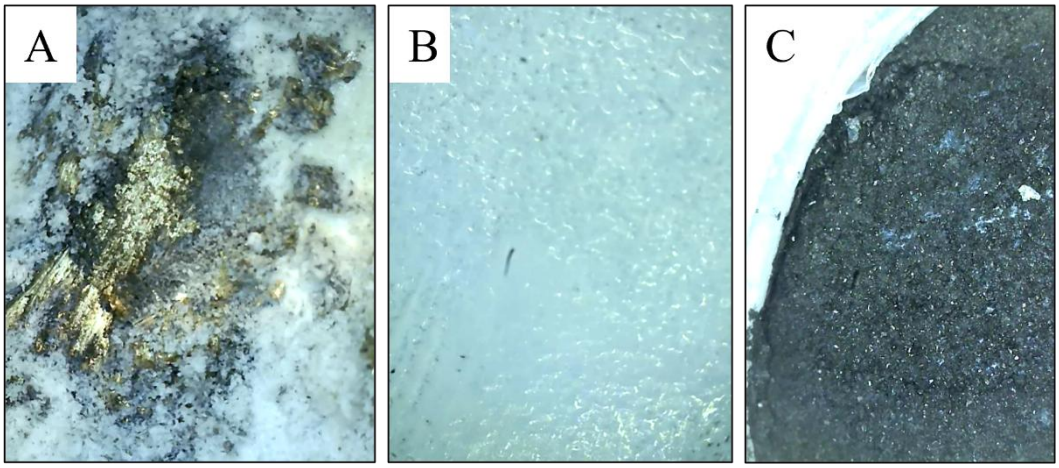

Fig. 2.8: A. Used Anode; B. Used Separator; C. Used Cathode (coin cell without TTH).

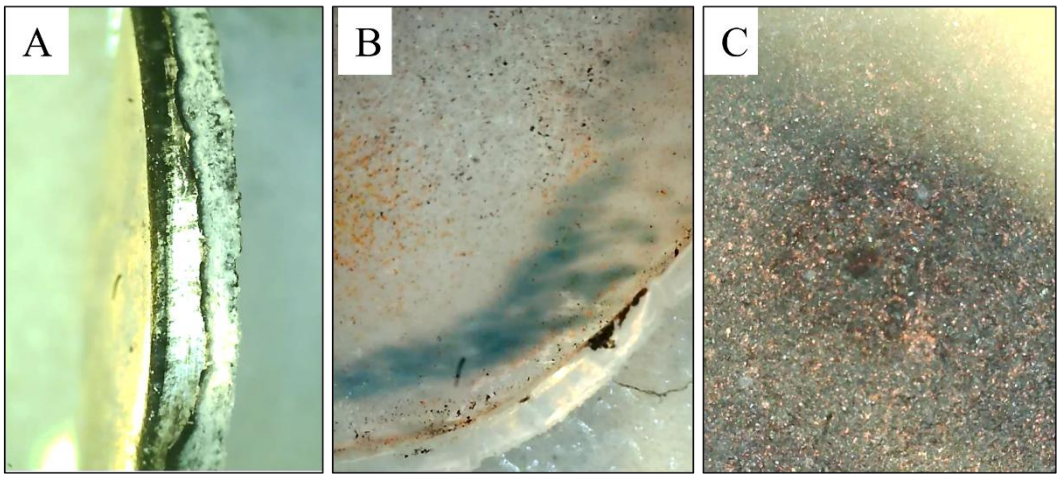

Fig.2. 9: A. Used Anode; B. Used Separator; C. Used Cathode (coin cell with TTH).

X-ray diffraction (XRD) analysis was conducted on the anodes recovered from discharged cells. The results indicated the presence of lithium hydroxide (LiOH) as the dominant crystalline phase, with relative contents ranging from 92% to 98% on the anode surface in contact with the separator. This observation suggests that the separator was not sufficiently effective in preventing moisture ingress from the atmosphere, leading to the formation of LiOH. Consequently, the penetration of trace water through the separator contributed to the development of a passivation layer on the lithium anode (**Fig. 2.10**).

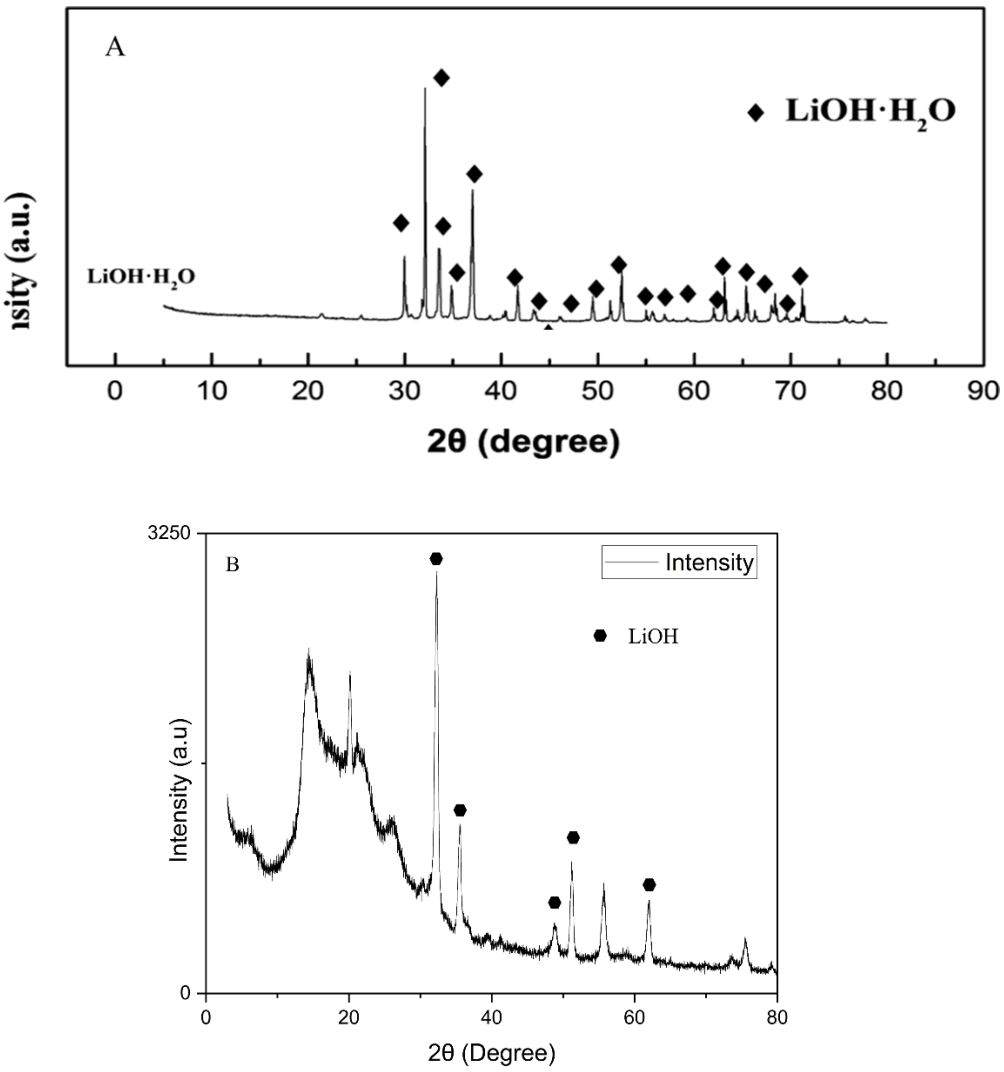

Fig. 2.10: A. Reference XRD data of LiOH[23] and B**.** XRD data of discharged anode.

2.7. Characterization of Pullulan membrane

Conductivity measurement: The ionic conductivity of the pullulan membranes, with a thickness of approximately 25-30 μm, was evaluated using electrochemical impedance spectroscopy (EIS). For this purpose, the membranes were carefully cut into circular disks with a diameter of 10 mm (**Fig. 2.11A**) and subsequently soaked in 1 M LiTFSI electrolyte for 2 h to ensure complete electrolyte uptake and equilibration. After soaking, the membranes were assembled into a two-electrode Swagelok cell configuration (**Fig. 2.11B**), where stainless steel blocking electrodes were employed to prevent faradaic reactions. Impedance measurements were then carried out over a wide frequency range to determine the bulk resistance of the electrolyte-saturated membrane, from which

the ionic conductivity was calculated. This methodology enabled the assessment of the membrane's ionic transport properties under conditions relevant to Li-O_2 cell operation. Equation 2.4 was used to calculate the conductivity of the membranes (**Table 2.6**):

$$Conductivity(S\ cm^{-1}) = \frac{Thickness\ of\ membrane\ (cm)}{Resistance\ (Ohm) * 0.786\ cm^2} \qquad \text{(equation 2.4)}$$

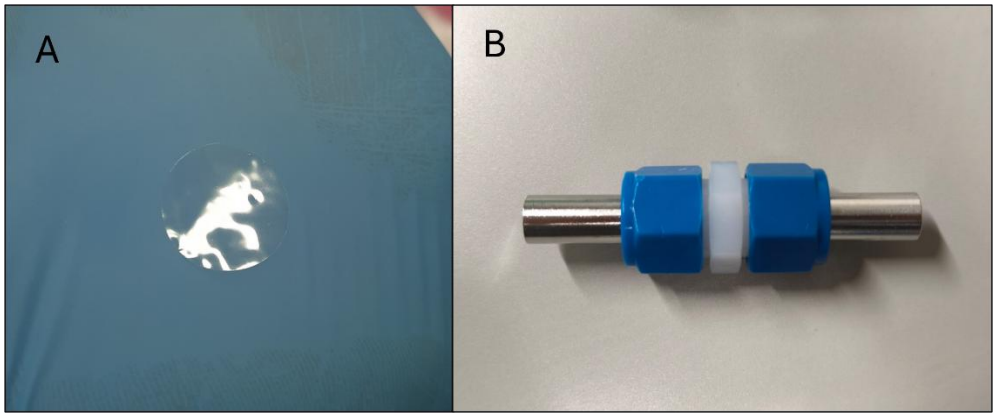

Fig. 2.11: (A) Disk of Pullulan membrane; (B) two-electrode Swagelok cell.

Name of the membrane (Table 2)	Conductivity (S cm^{-1})
Commercial PE-PP-PE	$2.68 * 10^{-4}$
M1	$5.9 * 10^{-5}$
M2	$1.4 * 10^{-5}$
M3	$1.52 * 10^{-4}$
M4	$3.66 * 10^{-4}$

Table 2.6: Conductivity table of membranes.

Oxygen permeability test: Oxygen permeability of the membranes was evaluated using a custom-designed three-electrode H-cell configuration. The membrane sample was mounted at the junction separating the two chambers of the H-cell, ensuring a hermetic seal between compartments. Both chambers were filled with electrolyte to a level sufficient to completely immerse the membrane, thereby eliminating any direct gas–liquid interface other than through the membrane itself.

On the cathodic side of the cell, a conventional three-electrode system was assembled, consisting of a glassy carbon working electrode, a platinum counter electrode, and a graphite reference electrode. To prevent oxygen ingress from the external environment, a continuous argon flow was maintained over the electrolyte surface on this side. This ensured that any oxygen detected electrochemically originated exclusively from permeation through the membrane. In contrast, the opposing chamber was continuously purged with pure oxygen gas, thereby establishing a constant driving force for oxygen diffusion across the membrane (**Fig. 2.12**).

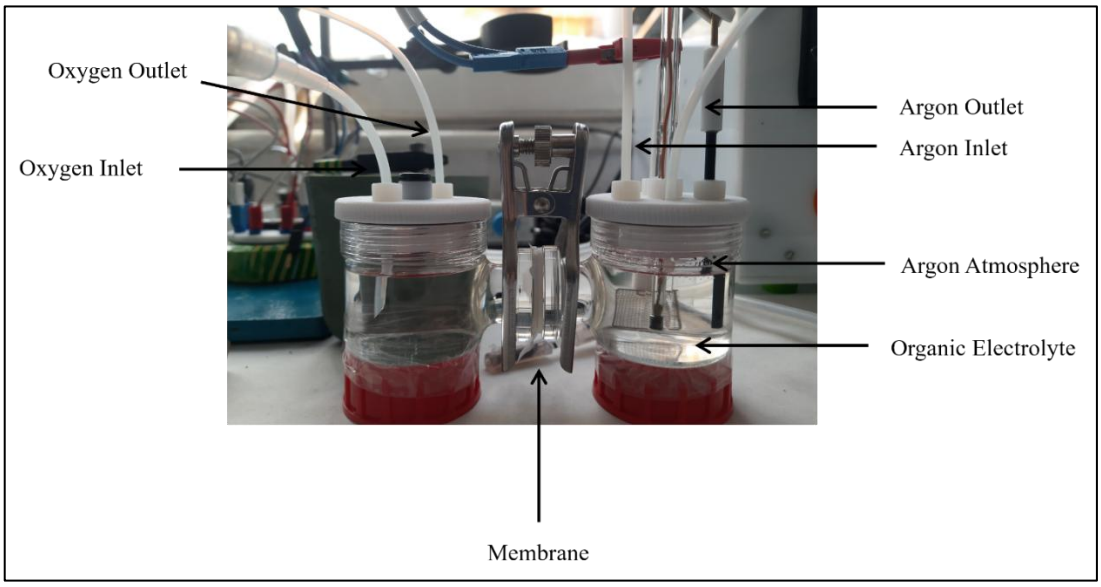

Fig. 2.12: Oxygen permeability experiment setup.

This configuration enabled precise monitoring of oxygen transport through the membrane by recording the electrochemical response at the working electrode, providing a reliable assessment of membrane oxygen permeability under controlled conditions. Periodic cyclic voltammogram (CV) measurements were performed with a scan rate of 50 mV s^{-1}, incorporating a 30-minute interval between successive scans. This protocol was maintained continuously for a duration of two days. The recorded voltammograms revealed the appearance of a distinct reduction peak, indicating electrochemical activity associated with oxygen permeation through the membrane (**Fig. 2.13**). From the CV measurement, it is confirmed that both the pullulan membrane and commercial separator show a

similar pattern and are not very efficient in long-term measurement. Oxygen diffusion happens in both cases.

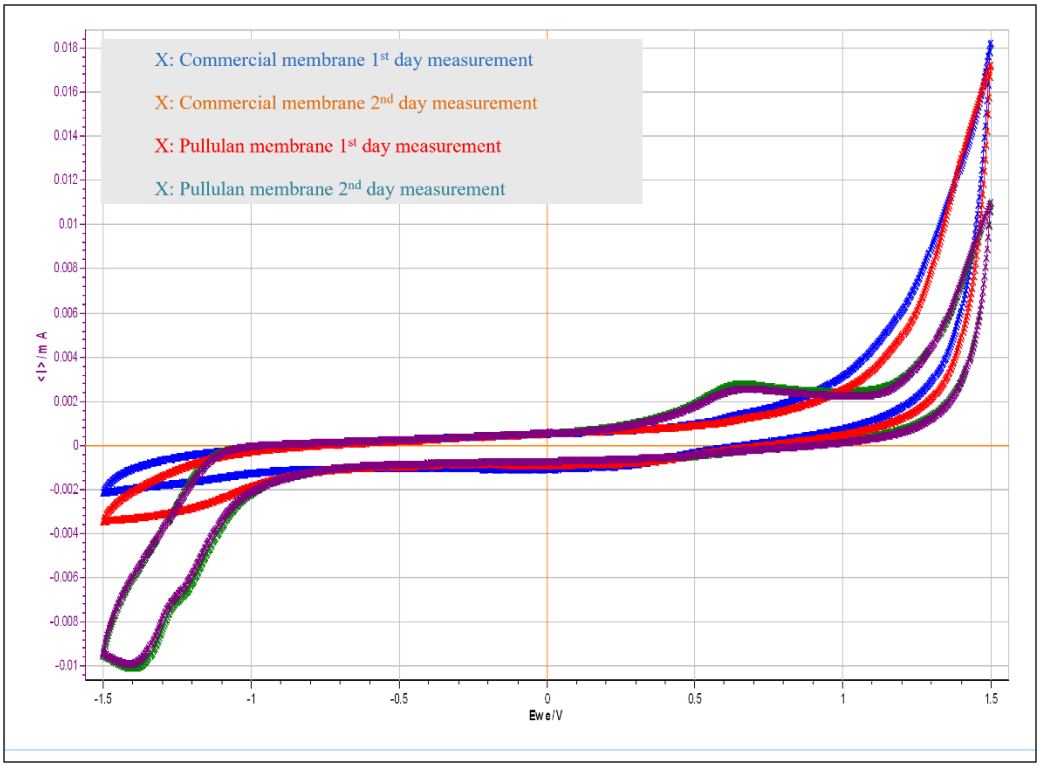

Fig. 2.13: CV measurement of commercial and pullulan membranes.

2.7. Conclusion

The systematic investigation of electrodes and separators in Li-O_2 cells highlights the critical influence of material composition, cell configuration, and environmental conditions on electrochemical performance with battery capacity reaching 170 mAh. Activated carbon cathodes provided a high surface area for discharge product accommodation, while pullulan-based membranes demonstrated promising barrier properties against moisture ingress. However, XRD analysis revealed significant LiOH formation, indicating incomplete protection by the separator. Temperature fluctuations and electrolyte volume further impacted discharge behaviour. Customized coin-cell designs with optimized gas access improved reproducibility. Overall, tailoring both electrode architecture and separator functionality is essential for mitigating parasitic reactions and enhancing durability in Li-O_2 batteries.

2.8. Reference

[1] Bruce, P. G., Freunberger, S. A., Hardwick, L. J., & Tarascon, J. M., Nature Materials, **2012**, 11, 19-29.

[2] Luntz, A. C., & McCloskey, B. D., Chemical Reviews, **2014,** 114(23), 11721–11750.

[3] Abraham, K. M., & Jiang, Z., Journal of The Electrochemical Society, **1996**, 143(1), 1-5.

[4] Christensen, J., & Newman, J., Journal of The Electrochemical Society, **2012,** 159(2), R1-R30.

[5] Kwak, W. J., Sharon, D., Xia, C., et al., Chemical Reviews, **2020**, 120(14), 6626-6683.

[6] Liu, T., Leskes, M., Yu, W., Moore, A. J., Zhou, L., Bayley, P. M., et al., Science, **2015**, 350(6260), 530–533.

[7] Ottakam Thotiyl, M. M., Freunberger, S. A., Peng, Z., & Bruce, P. G., Journal of the American Chemical Society, **2013,** 135(1), 494–500.

[8] McCloskey, B. D., Bethune, D. S., Shelby, R. M., et al., Journal of Physical Chemistry Letters, **2011**, 2(10), 1161–1166.

[9] Crowther, O., Salomon, M., Membranes **2012**, 2(2), 216-227.

[10] Wang, M., Zhuge, X., Liu, T., Jia, S., Luo, K., Ren, Y., Shahzad, A., Liu, X., Adv. Energy Sustainability Res. **2023**, 4, 2300111.

[11] Lei, Z., Liu, B., Koudakan, P. A., Pan, H., Qian, Y., Wang, G., Nano Futures, 2**022,** 6, 012002.

[12] Chen, H., Yang, D., Huang, G., Zhang, X., Acta Phys. -Chim. Sin. **2024**, 40 (7), 2305059.

[13] Jenkins, M., Dewar, D., Lagnoni,L., Yang, S., Rees, G. J., Bertei, A., Johnson, L. R., Gao, X., Bruce, P. G., Adv. Mater. **2024**, 36, 2405715.

[14] Xia, Q., Li, D., Zhao, L., Wang, J., Long, Y., Han,X., Zhou,Z., Liu, Y., Zhang, Y., Li, Y., Adamb, A. A. A., Chou, A., Chem. Sci., **2022**, 13, 2841–2856 | 2841.

[15] Wang, Y., Cho, S. C., Journal of The Electrochemical Society, **2013,** 160(10), A1847-A1855. Chem. Rev. 2020, 120, 14, 6626-6683.

[16] Kwak, W. J., Rosy, Sharon, D., Xia, C., Kim, H., Johnson, L. R., Bruce**,** P. G., Nazar, L. F., Sun, Y. K., Frimer, A. A., Noked, M., Freunberger, S. A., Aurbach, D., Chem. Rev. 2020, 120, 14, 6626–6683.

[17] Thotiyl, M. M. O.; Freunberger, S. A.; Peng, Z.; Chen, Y.; Liu, Z.; Bruce, P. G., J. Am. Chem. Soc. **2013**, 135 (12), 4940-4947.

[18] Saengkaew, J.; Choi, J. W.; Lee, J. H.; Lee, K. H.; Lee, S. H.; Kim, H. J.; Lee, S. H.; Lee, J. H.; Cho, J., J. Phys. Chem. C **2023**, 127 (2), 1234-1242.

[19] Mahne, N.; Schafzahl, B.; Leypold, C.; Leypold, M.; Grumm, S.; Leitgeb, A.; Strohmeier, G. A.; Wilkening, M.; Fontaine, O.; Kramer, D.; Slugovc, C.; Borisov, S. M.; Freunberger, S. A., Nat. Energy **2017**, 2, 17036.

[20] Jo, H. G., Kim, J. H., Lee, H. W., **2020**, Catalysts, 10(11), 1316.

[21]Poli, F., Momodu, D., Spina, G. E., Terella, A., Mutuma, B. K., Focarete, M. L., Manyala, N., Soavi, F., Electrochim. Acta **2020,** 338, 135872.

[22] Spina, G.E., Poli, F., Brilloni, A., Marchese, D., Soavi, F. Natural polymers for green supercapacitors, Energies **2020.** 13, 3115-3131.

[23] Li, S., Huang, H., Li, J., Kobayashi, N., Osaka, Y., He, Z., Yuan, H., RSC Adv., **2018**, 8, 8199-8208.

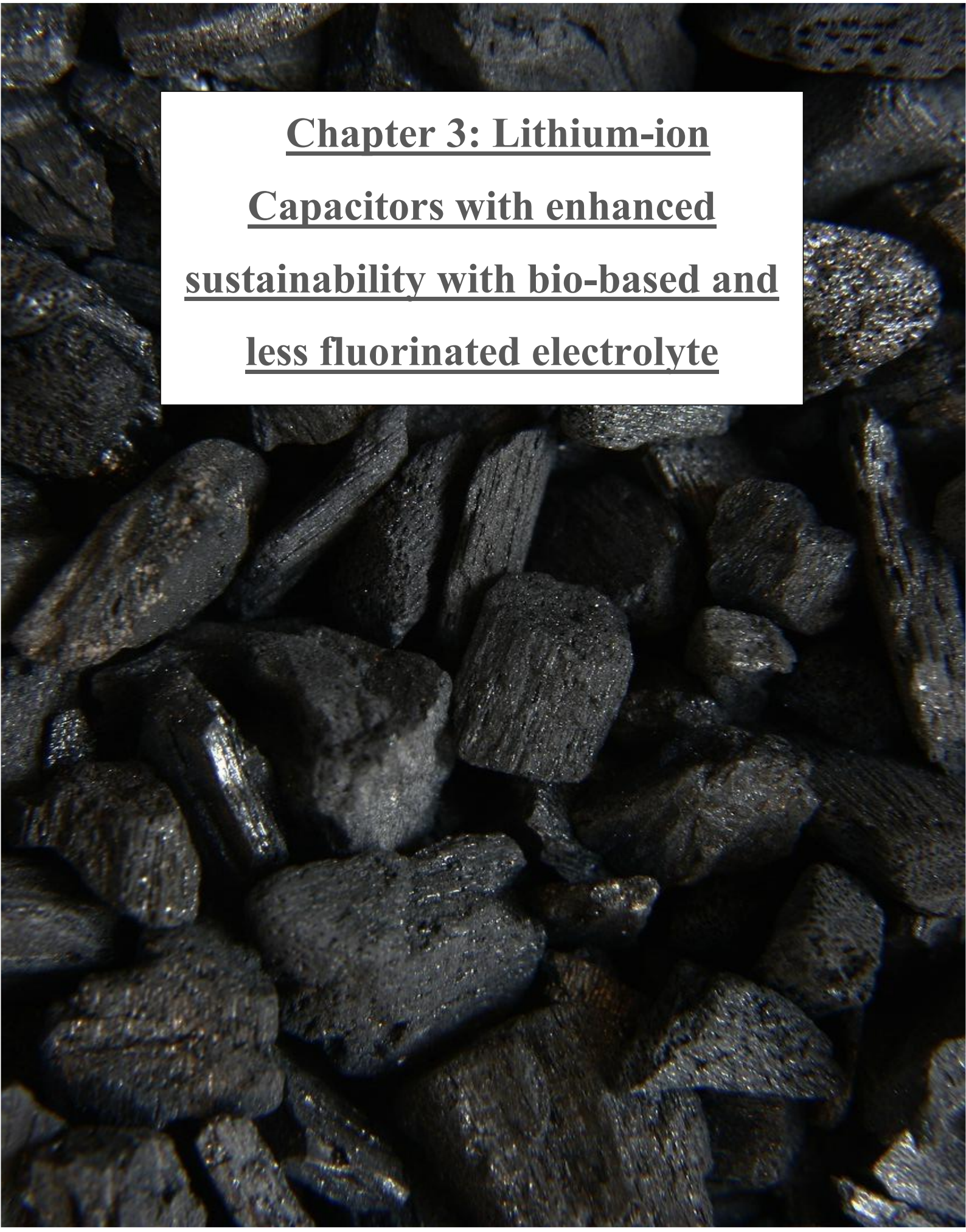

Chapter 3: Lithium-ion Capacitors with enhanced sustainability with bio-based and less fluorinated electrolyte

Index

3.1. Introduction

Metal-ion hybrid supercapacitors combine a battery-type electrode with a capacitive electrode within the same cell. Within this asymmetrical configuration, one electrode stores charge electrostatically (capacitive-type), while the other one (battery-type) undergoes faradaic charge storage[1]. This hybrid design bridges the gap between batteries and conventional supercapacitors, offering intermediate properties that make them attractive for applications requiring moderate energy density alongside high power delivery[2,3].

Among them, lithium-ion capacitors (LICs), first introduced by Amatucci et al. have drawn significant attention due to the synergistic integration of lithium-ion battery (LIB) and electric double-layer capacitor (EDLC) technologies. A LIC typically features a LIB-type negative electrode paired with an EDLC-type positive electrode, both immersed in an organic electrolyte containing a lithium-ion conducting salt. As illustrated in (**Scheme 3.1**), LIC charge/discharge processes combine faradaic and non-faradaic mechanisms: during charging, lithium ions intercalate into the anode, while electrolyte anions adsorb onto the porous surface of the positive electrode; during discharge, these processes reverse spontaneously, generating electric current[5,6].

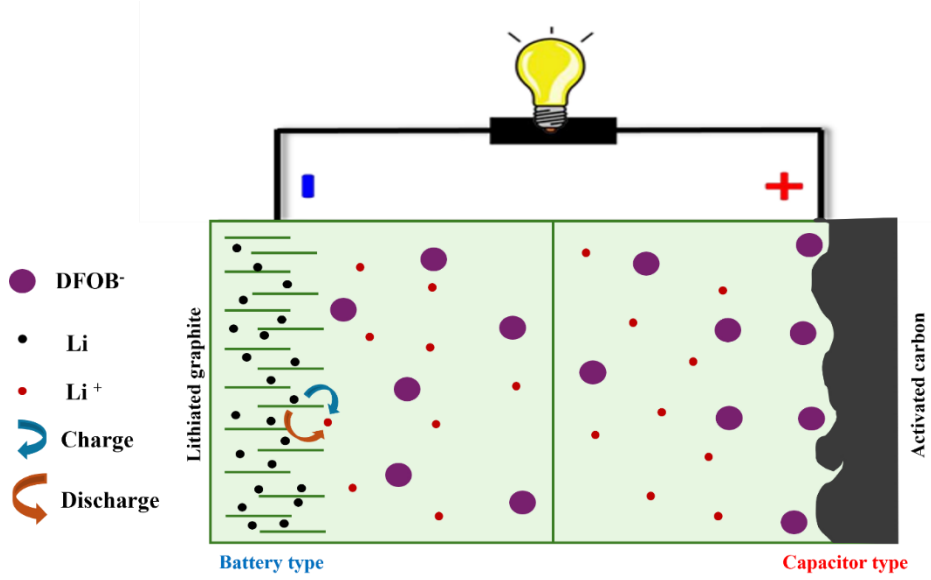

Scheme 3.1: Lithium-ion capacitor operation diagram.

In an ideal LIC, cell voltage shows a linear dependence with time, similar to what occurs in EDLCs. The amount of stored energy is proportional to the capacitance, C and to the square of the operating upper, V^2_{max}, and lower voltages, V^2_{min}, according to the following equation:

$$E = \frac{1}{2} C (V_{max}^2 - V_{min}^2) \quad \text{(equation 1)}$$

Owing to their higher operating potentials compared to EDLCs, LICs achieve significantly greater energy densities. At the same time, the electrostatic charge storage at the positive electrode enables much faster charge-discharge rates than those of LIBs. The key advantages of LICs can be summarized as follows: (i) higher energy density and lower self-discharge (<5% voltage drop at room temperature) relative to EDLCs; (ii) superior power density compared to LIBs; (iii) excellent long-term cycling stability; and (iv) a wide operating temperature range, from -20 to 70 °C[7]. Ragone plots, which represent the relationship between energy density and power density, are commonly employed to benchmark different electrochemical energy storage systems. As illustrated in **Fig. 3.1**, the Ragone plot clearly demonstrates the "bridging" role of LICs between batteries and supercapacitors.

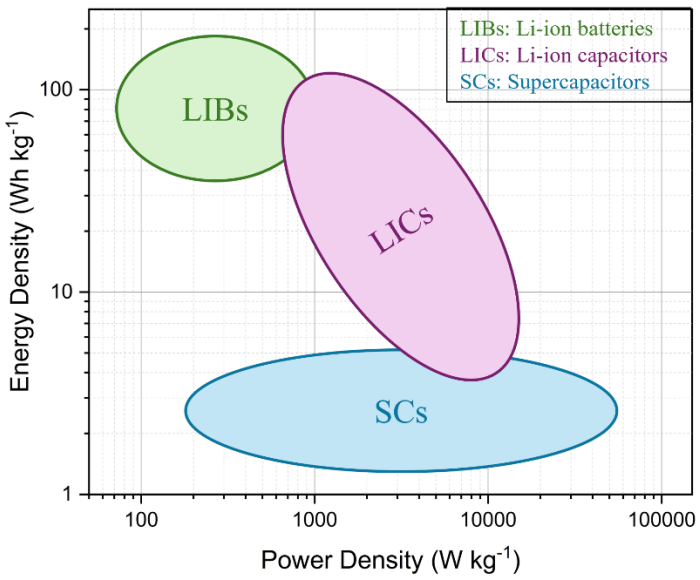

Fig. 3.1: Ragone plot comparing performance of representative energy storage devices.

Although lithium-ion capacitor (LIC) technology has already reached commercialization[8], several challenges remain, the most critical being the kinetic imbalance between the positive and negative electrodes. The overall energy density of LICs is constrained by the limited specific capacitance of the capacitive-type electrode, since the battery-type electrode typically offers much higher specific capacity. Conversely, the power density is restricted by the sluggish kinetics of the battery-type electrode[9].

The electrolyte is another critical component for LIC, as it governs several key performance parameters. It facilitates the formation of a stable solid-electrolyte interphase (SEI) on the anode, which is essential for ensuring long-term cycling stability. In addition, the electrolyte determines the electrochemical stability window, which directly influences the achievable energy density, and its ionic conductivity plays a decisive role in defining the system's power capability.

Typically, an electrolyte consists of a solvent and a lithium salt, both of which strongly affect the interfacial and bulk electrochemical behavior of the device. However, most commercial lithium salts, such as $LiPF_6$ - contain a high proportion of fluorine, which raises environmental and safety concerns due to their potential to release corrosive or toxic fluorinated byproducts. Similarly, the carbonate-based solvents commonly used (e.g., ethylene carbonate, dimethyl carbonate, and propylene carbonate) are derived from petrochemical sources and are not readily biodegradable, thus limiting their sustainability and environmental compatibility. Consequently, there is growing interest in the development of fluorine-reduced salts and bio-based or green solvent systems to enable safer, more sustainable electrolyte formulations for next-generation lithium-ion batteries and capacitors[10, 11].

For the positive electrode, as in EDLCs, activated carbon is the preferred material due to its: (i) high specific surface area, which provides large capacitance; (ii) wide operating voltage window, ensuring high energy density; (iii) excellent electronic conductivity, enabling high power delivery; and (iv) good electrolyte accessibility through its porous network[12].

For the negative electrode, materials derived from LIB anodes are commonly employed. These can be classified based on their Li^+ storage mechanism into: insertion-type (e.g., pre-lithiated carbons or graphite, $Li_4Ti_5O_{12}$, TiO_2),

conversion-type (e.g., SnO_2, Fe_3O_4, Nb_2O_5), and alloy-type (e.g., Si, Sn)[12]. Despite the broad range of materials investigated, dual-carbon LICs (DC-LICs), where both electrodes are carbon-based have demonstrated safer operation, improved long-term cycling stability, greater reliability, and higher power density compared to other LIC configurations[7,13].

However, since both carbonaceous electrodes lack intrinsic lithium, pre-lithiation of the negative electrode is required for DC-LIC operation. This step, while enabling the use of alternative carbons with low initial coulombic efficiency (as irreversible processes such as SEI formation occur during pre-lithiation), also increases manufacturing complexity and cost[14,15].

Another critical challenge, especially at the laboratory scale, is lithium plating. This occurs when the potential of the battery-type electrode drops below 0 V, leading to the deposition of metallic lithium. Such plating not only shortens the device lifespan but also poses severe safety risks. To mitigate this issue, precise control of the pre-lithiation process and careful balancing of electrode kinetics are required to prevent lithium deposition and ensure reliable LIC performance[16].

3.2. State-of-the-art of Li-ion capacitor

In commercial LICs, carbonate-based organic electrolytes-commonly ethylene carbonate (EC), dimethyl carbonate (DMC), and related solvents-are employed in combination with lithium hexafluorophosphate ($LiPF_6$) as the conducting salt. While these electrolytes have enabled the practical deployment of LIC technology, they pose several sustainability and safety concerns. Carbonate solvents are derived from non-renewable sources and present environmental challenges, while $LiPF_6$ requires multiple mined raw materials for production and suffers from limited thermal and chemical stability. These issues highlight the urgent need for more sustainable, safe, and eco-friendly electrolyte systems to advance LIC technology[16].

In recent years, research has increasingly focused on alternative salts and solvents that can improve both performance and environmental sustainability. One promising candidate is lithium difluoro(oxalato)borate (LiDFOB), which offers enhanced stability and reduced fluorine content compared to $LiPF_6$, making it a more environmentally benign option. In parallel, bio-derived solvents have

attracted attention as renewable electrolyte components. Among them, 5-methyl-1,3-dioxolane-4-one (LAHH), synthesized from lactic acid, has emerged as a promising green solvent. Previous studies have demonstrated that LAHH can be effectively applied in both EDLCs and LIBs, owing to its favorable transport and thermal properties[11,18].

Building on this foundation, the present study explores the combined use of LiDFOB and LAHH as an innovative electrolyte system for LICs. The physicochemical properties of this electrolyte, including ion transport and thermal stability, have been systematically investigated. Furthermore, its electrochemical performance has been evaluated in LICs employing graphite as the negative electrode and activated carbon as the positive electrode. The assembled LICs exhibited excellent performance, demonstrating high energy and power delivery. These results suggest that the integration of eco-friendly salts with bio-derived solvents provides a viable pathway toward sustainable and high-performance LIC technology.

3.3. Results and discussions

3.3.1. Physicochemical characterization of the electrolyte

The physicochemical and electrochemical characteristics of the selected electrolyte system were systematically investigated, taking 1 M LiDFOB in LAHH as the standard electrolyte composition for this study. For comparison, the physicochemical response of 1 M LiDFOB in propylene carbonate (PC) electrolyte was also studied, since PC is a conventional electrolyte solvent. The ionic conductivity of the electrolyte was evaluated over a wide temperature range, from -30 °C to 80 °C, while the viscosity was measured between -20 °C and 80 °C, in order to capture both low-temperature and elevated-temperature behavior and it was observed that the electrolytes shows increase of conductivity with the increasing temperature and viscosity trend is the opposite. At 20 °C, the electrolyte demonstrated a viscosity of 4.53 mPa.s and conductivity 2.70 mS cm^{-1} which falls within the typical range reported for advanced lithium-ion battery

electrolytes, whereas PC based electrolyte shows conductivity of 3.91 mS cm^{-1} (**Fig. 3.2A**)[19].

The electrochemical stability window (ESW) was determined by linear sweep voltammetry using a silver reference electrode. The electrolyte exhibited a stable ESW up to 4.8 V vs. Li^+/Li, thereby confirming its suitability for use with high-voltage cathode materials (**Fig. 3.2B**). Such stability is particularly relevant since electrolytes capable of maintaining wide electrochemical windows while ensuring adequate ionic transport are highly desirable for next-generation lithium-ion batteries.

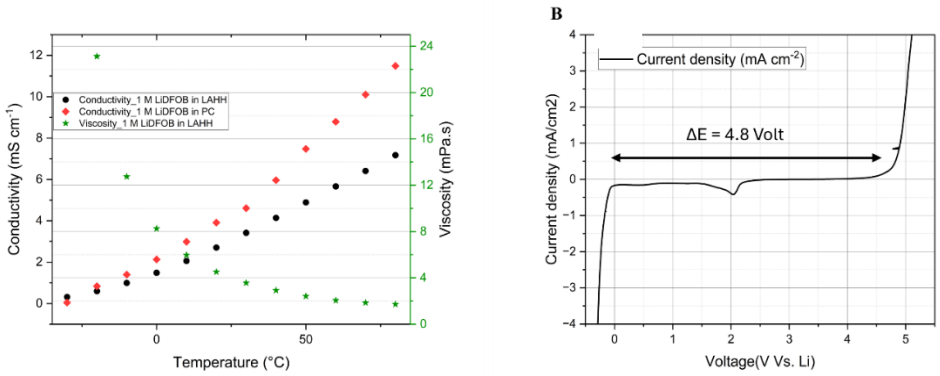

Fig. 3.2: (A) Conductivity between –30 and 80 °C. and viscosity between –20 and 80 °C, (B) The electrochemical stability window shows the stable potential window is 4.8 V. against Li.

3.3.2. Characterization of the negative electrode with graphite half-cell

The electrochemical performance of the 1 M LiDFOB in LAHH electrolyte was preliminarily evaluated using graphite electrodes in a half-cell configuration. During the first galvanostatic discharge, the corresponding differential capacity (dQ/dV) profile revealed a broad peak in the voltage region of 1.70-1.55 V vs. Li^+/Li (**Fig. 3.3**). This feature is commonly attributed to the reductive decomposition of the difluoro(oxalato)borate ($DFOB^-$) anion, which leads to the formation of a solid-electrolyte interphase (SEI) on the graphite surface[20,21].

The formation of such an SEI layer is a critical step for stabilizing the electrode-electrolyte interface, as it helps suppress continuous electrolyte decomposition and contributes to improved cycling stability in subsequent charge-discharge

processes. Similar behaviors have been reported for electrolytes containing borate-based salts, where controlled decomposition at the electrode surface results in the formation of inorganic-rich, ion-conductive interphases that enhance long-term electrochemical stability[22,23,24].

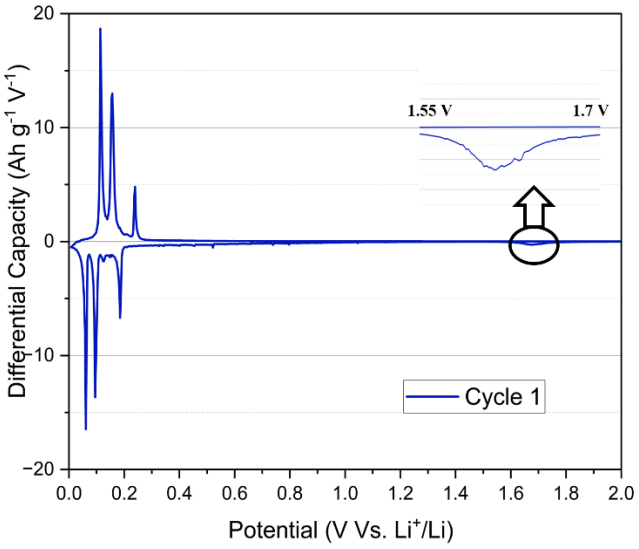

Fig. 3.3: Graphite half-cell differential capacity curve of the first galvanostatic charge/discharge cycle.

The galvanostatic charge-discharge behavior of graphite half-cells containing the 1 M LiDFOB in LAHH electrolyte was systematically examined at varying C-rates in order to evaluate its rate performance. For comparison, the electrochemical response of graphite electrodes cycled in the 1 M LiDFOB in PC electrolyte was also investigated under identical conditions. In both electrolyte systems, the formation of SEI was observed, as evidenced by the hump appearing between 1.70-1.55 V during the first discharge cycle. The SEI primarily originates from the irreversible decomposition of the DFOB anion, leading to a low initial coulombic efficiency. The cells containing 1 M LiDFOB in LAHH and 1 M LiDFOB in PC exhibit initial coulombic efficiencies of 62.84% and 75.26%, respectively (**Fig. 3.4**). However in subsequent galvanostatic cycles at 0.1 C, the reduction peaks associated with SEI formation disappear, and the coulombic efficiency stabilizes above 98% after 5 cycles, indicating a highly reversible electrochemical process after the initial cycles.

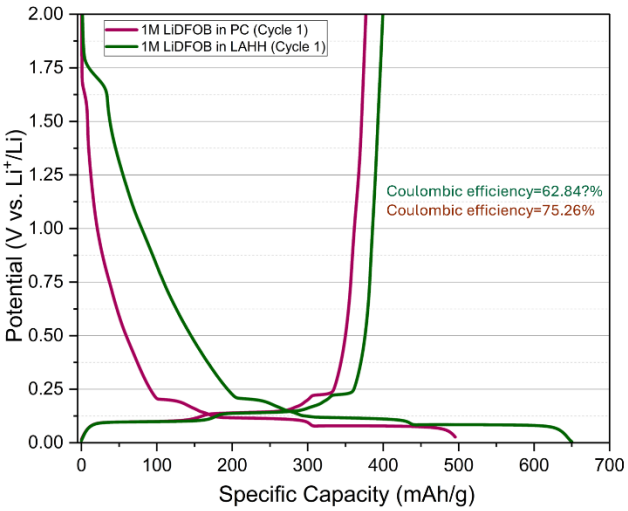

Fig. 3.4: Graphite half-cell first galvanostatic charge/discharge cycle.

After the 1st discharge at C/20, both cells were performed rete capability test at different C-rates and the results clearly indicate that the 1 M LiDFOB in LAHH system delivers a higher capacity across the tested lower current densities compared to the 1 M LiDFOB in PC electrolyte (**Fig. 3.5**). The discharge capacity for both LAHH and PC based cell at 1C was 359.40 mAh g-1 and 315.77 mAh g^{-1} respectively with coulombic efficiency 99.85%. However, at 5C, the cell using 1 M LiDFOB in PC exhibits a higher discharge capacity compared to that using 1 M LiDFOB in LAHH. This difference can be attributed to the ionic conductivity of the two electrolytes (**Fig. 3.2A**). Specifically, 1 M LiDFOB in PC possesses a higher ionic conductivity at room temperature than 1 M LiDFOB in LAHH. At 20 °C the conductivities of both the electrolytes are 3.91 and 2.70 mS cm^{-1} respectively. At elevated C-rates, the ion transport within the electrolyte becomes the limiting factor for capacity; consequently, as the C-rate increases, the available capacity decreases due to insufficient ion supply to sustain the electrochemical reactions.

LAHH has also been investigate as electrolyte solvent for LIB and it combines good ion transport, wide electrochemical stability, safety, and renewability-making it an effective and sustainable electrolyte solvent alternative to conventional carbonates in lithium-ion batteries[18].

These findings demonstrate the potential advantages of LAHH as a solvent matrix for LiDFOB-based electrolytes in high-rate lithium-ion capacitor applications, where both high capacity and fast charge–discharge capability are essential.

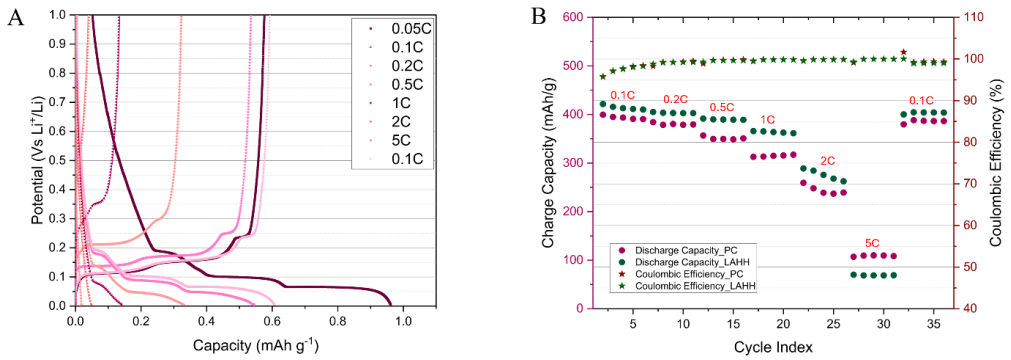

Fig. 3.5: (A) Galvanostatic charge/discharge curves of graphite half-cells at different C-rates for 1 (M) LiDFOB in LAHH, (B) rate capability test.

3.3.3. Characterization of the positive electrode with activated carbon (AC) half-cell

To evaluate the electrochemical behavior of the cathode material, activated carbon (AC) half-cells employing the 1 M LiDFOB electrolyte were studied by cyclic voltammetry (CV) within the potential window of 2.0-4.2 V vs. Li^+/Li. The CV profiles recorded at different scan rates exhibit well-defined rectangular-shaped curves **(Fig. 3.6A)**, which are indicative of an ideal capacitive response, consistent with the surface-controlled charge storage mechanism of porous carbon electrodes.

Importantly, this capacitive profile in CV measurement is preserved even at a relatively high scan rate of 50 mV s^{-1}, demonstrating the excellent rate capability of the AC electrode in the LiDFOB-based electrolyte (**Fig. 3.6A**). Moreover, in the galvanostatic charge-discharge measurements the capacitance retention remains stable under elevated current densities with capacitance 172.5 F g^{-1} at 5 A g^{-1}, suggesting efficient ion transport within the porous structure and minimal

diffusion limitations (**Fig. 3.6B**). Such behavior confirms that the electrolyte provides a favorable environment for maintaining double-layer capacitance over a wide range of operating conditions, thereby highlighting its potential for high-power lithium-ion capacitor applications[25,26].

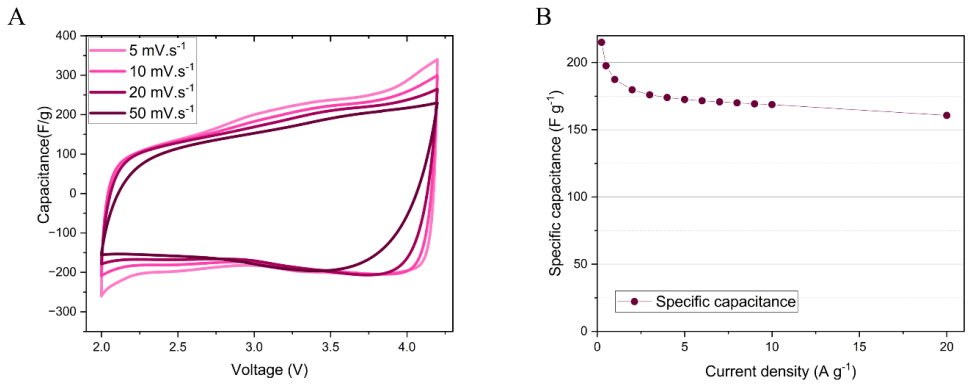

Fig. 3.6: (A) CV measured at different scan rates and (B) Specific capacitance at various current densities of activated carbon vs. Li-metal half cells with 1(M) LiDFOB in LAHH as electrolyte.

3.3.4. Assembly and performance of the LIC

To maximize the energy output of a LIC, careful mass balancing of the electrodes is essential. In principle, the positive and negative electrodes should be designed to store an equal amount of charge in order to ensure efficient operation and to prevent electrode degradation during cycling. Nevertheless, the realization of a proper charge balancing for the electrodes of LICs is quite challenging, mainly due to the kinetics limitations of the negative electrode. Accordingly, most studies focusing on hybrid materials use to employ mass balancing instead. For the present work, initially 1/1.5 mass ratio between the positive and negative electrodes was chosen as a practical compromise, with the aim of tailoring the device for applications requiring charge-discharge durations of approximately 25 seconds, which corresponds to a current density of 2 A g^{-1}.

The graphite electrode underwent a prelithiation treatment prior to full-cell assembly. This step was necessary to incorporate Li to the negative electrode.

Specifically, the electrode was subjected to seven charge-discharge cycles within the potential window of 0.005-2.0 V vs. Li^+/Li at a rate of 0.1C. During the final discharge, the current was reduced and the cutoff potential was adjusted to 50 mV Vs. Li^+/Li, ensuring sufficient lithium insertion and controlled SEI development (**Scheme 3.2A**).

After the prelithiation process, the lithiated graphite was assembled with activated carbon (AC) in a three-electrode Swagelok-type cell, where lithium metal served as the reference electrode to enable accurate monitoring of electrode potentials (**Scheme 3.2B**). In this configuration, the potential of the graphite negative electrode was maintained at 50 mV vs. Li/Li^+, while the AC positive electrode was charged up to 4.15 V vs. Li/Li^+. This deliberate use of different potential ranges for the electrodes effectively broadens the operating voltage window of the LIC, thereby significantly enhancing its energy density and overall performance.

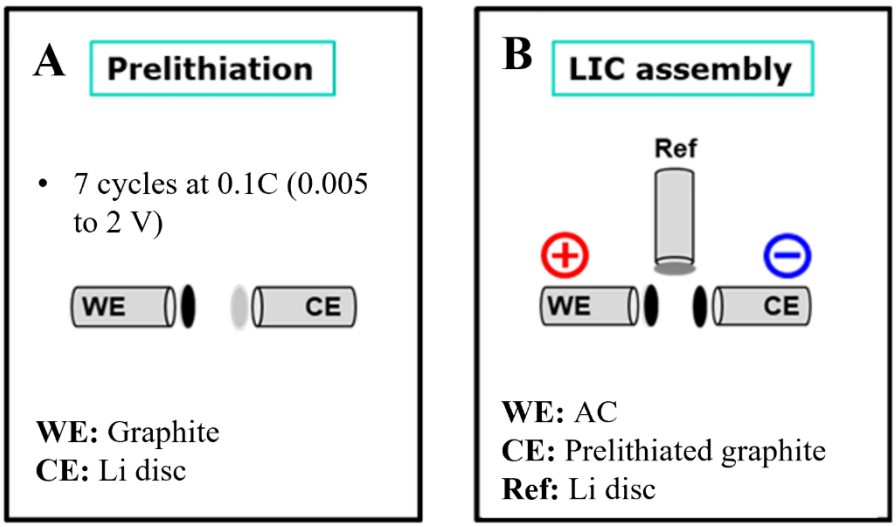

Scheme 3.2: Schematic representation of (A) prelithiation process and (B) LIC assembly.

Following assembly, the LICs were subjected to cycling at selected representative current densities within the 2.0-4.2 V operating voltage range. The corresponding galvanostatic charge–discharge (GCD) profiles (**Fig. 3.7A**) exhibit nearly linear voltage variations during both charging and discharging processes, a

behaviour that is characteristic of the non-faradaic capacitive charge storage mechanism typically observed in double-layer capacitors.

However, a pronounced ohmic voltage drop is evident in the curves, even at relatively low current densities. This feature reflects a considerable internal resistance within the system, which can be attributed to factors such as electrolyte ionic conductivity, interfacial impedance at the electrode-electrolyte interface, or the electronic resistance of the electrodes themselves. Such resistive effects can limit power performance and highlight the need for further optimization of the electrolyte formulation.

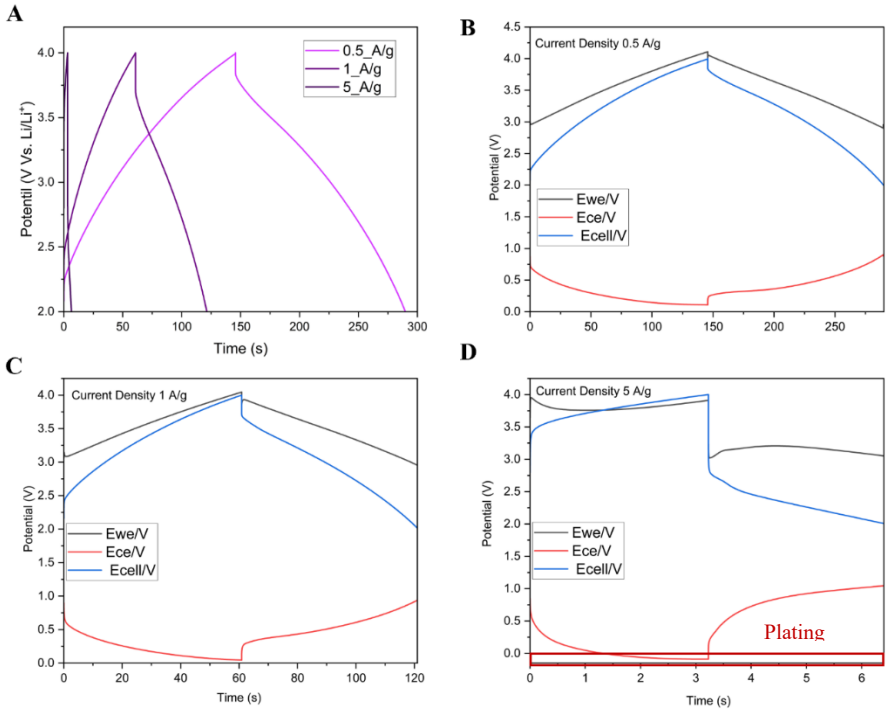

Fig. 3.7: (A) Galvanostatic charge/discharge curve for the LIC measured from 2 to 4.2 V at representative current rates, and galvanostatic charge/discharge profiles registered at 0.5 (B), 1 (C) and 5 A g^{-1} (D) for the LIC (blue), the negative electrode (red) and the positive electrode (black).

To get insight on the contribution of each electrode into the full cell, individual galvanostatic charge/discharge profiles were monitored at representative current rates. It is observed that at 0.5 A g^{-1} (discharge time of 3 minutes, **Fig. 3.7B**), the positive electrode potential swings 2.25 V, while the negative electrode only fluctuates 0.7 V. When current rate is increased over 1 A g^{-1} (**Fig. 3.7C**), the discharge time is reduced to 2 minutes and the potential swing

of the graphite-based negative electrode remains at 0.7 V, while the potential swing of the AC increases to 2.5 V. When current rate is increased over 5 A g^{-1} the potential of the graphite-based negative electrode reaches negative values (**Fig. 3.7D**), which can be risky not only affecting cyclability but also from a safety point of view.

Energy-to-power ratio of the LIC calculated from the galvanostatic charge/discharge curves in the voltage range of 2 - 4.2 V is represented in **Fig. 3.8A**. It can be observed that for a similar power density, the LIC can deliver more than double of the energy corresponding to its EDLC counterpart (0 - 2.5 V), and still shows impressive energy retention (83 Wh kg^{-1} and 3,000 W kg^{-1}) but the cyclic stability of the LIC is very poor, it loses around 70% of capacitance after only 500 cycles (**Fig. 3.8B**) when cycled at 2 A g^{-1} current density.

The observed issue may arise from inaccurate mass balancing between the positive and negative electrodes or from a poorly stable SEI formed on the negative electrode. To address these challenges, further optimization is required. i) Establishing an appropriate mass balance between the positive and negative electrodes is essential to ensure uniform charge storage and minimize irreversible capacity loss, which in turn enhances cyclic stability. ii) Incorporating itaconic anhydride as an electrolyte additive can promote the formation of a more stable and uniform SEI layer on the negative electrode. A robust SEI not only suppresses side reactions and electrolyte decomposition but also improves lithium-ion transport, thereby leading to better capacity retention and overall cycling performance.

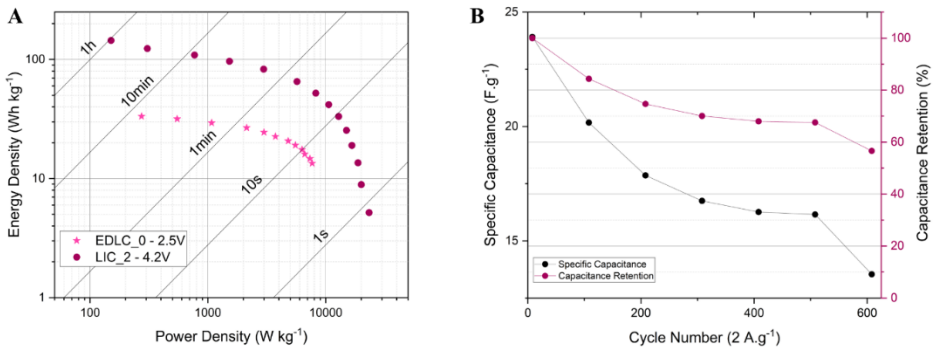

Fig. 3.8: (A) Ragone plot and (B) long-term cycling at 2 A g^{-1}.

3.4. Conclusion

In this work, we introduce the development of a sustainable electrolyte system based on a bio-derived LAHH solvent combined with LiDFOB, a salt with reduced fluorine content, for application in LICs. The formulated electrolyte demonstrates promising physicochemical and electrochemical properties, i) the electrolyte has comparable viscosity and conductivity, at 20 °C viscosity of the electrolyte is 4.53 mPa.s and conductivity is 2.70 mS cm^{-1}, ii) the electrolyte composition shows efficient performance in both graphite and activated carbon half-cells, iii) when implemented in LIC configurations, the system delivers an excellent balance of energy and power output of 83 Wh kg^{-1} and 3,000 W kg^{-1}, whereas EDLC can obtains energy to power ratio of 29 Wh kg^{-1} and 1,076 W kg^{-1}, underscoring its potential as an environmentally friendly alternative to conventional electrolytes.

Looking ahead, continued efforts will focus on the optimization of full-cell architecture and the fine-tuning of operating parameters, with the goal of further enhancing the long-term cycling stability and overall durability of LIC devices. Such improvements will be essential to advance this electrolyte system toward practical and large-scale energy storage applications.

3.5. Reference

[1] Tie, D., Huang, S., Wang, J., Ma, J., Zhang, J., Zhao, Y., Energy Storage Mater., **2019,** 21, 22-40. https://doi.org/10.1016/j.ensm.2018.12.018.

[2] Wang, H., Zhu, C., Chao, D., Yan, Q., Fan, H. J., Adv. Mater., **2017,** 29, 1702093. https://doi.org/10.1002/adma.201702093.

[3] Soltani, M., Beheshti, S. H., J. Energy Storage, **2021,** 34, 102019. https://doi.org/10.1016/j.est.2020.102019.

[4] Amatucci, G. G., Badway, F., Du Pasquier, A., Zheng, T., J. Electrochem. Soc. **2001,** 148, A930. https://doi.org/10.1149/1.1383553.

[5] Lamb, J. J., Burheim, O. S., Energies. **2021,** 14, 979. https://doi.org/10.3390/en14040979.

[6] Li, G., Yang, Z., Yin, Z., Guo, H., Wang, Z., Yan, G., Liu, Y., Li, L., Wang, J., J. Mater. Chem. A. **2019,** 7, 15541-15563. https://doi.org/10.1039/C9TA01246J.

[7] Han, P., Xu, G., Han, X., Zhao, J., Zhou, X., Cui, G., Adv. Energy Mater. **2018,** 8, 1801243. https://doi.org/10.1002/aenm.201801243.

[8] Xu, J., Gao, B., Huo, K., Chu, P. K., J. Nanosci. Nanotechnol. **2020,** 20, 2652 2667. https://doi.org/10.1166/jnn.2020.17475.

[8] Li, B., Zheng, J. Zhang, H., Jin, L., Yang, D., Lv, H., Shen, C., Shellikeri, A., Zheng, Y., Gong, R., Zheng, J. P., Zhang, C., Adv. Mater. **2018,** 30, 1705670. https://doi.org/10.1002/adma.201705670.

[10] Dzmitry Ivanou et al, J. Electrochem. Soc. **2018,** 165, H1040. 10.1149/2.0441816jes.

[11] Teoh, K. S., Melchiorre, M., Magar, S. D., Hermesdorf, M., Leistenschneider, D., Oschatz, M., Ruffo, F., Gómez Urbano, J. L., Balducci, A., Adv. Mater. **2024**, 36, 2310056.

[12] Han, C., Li, H., Shi, R., Xu, L., Li, J., Kang, F., Li, B., Energy Environ. Mater. **2018,** 1, 75 87. https://doi.org/10.1002/eem2.12009.

[13] Zhang, S. S., Batter. Supercaps. **2020,** 3, 1137-1146. https://doi.org/10.1002/batt.202000133.

[14] Jin, L., Shen, C., Shellikeri, A., Wu, Q., Zheng, J., Andrei, P., Zhang, J. G., Zheng, J. P., Energy Environ. Sci. **2020,** 13, 2341-2362. https://doi.org/10.1039/D0EE00807A.

[15] Zhang, J., Liu, X., Wang, J., Shi, J., Shi, Z., Electrochim. Acta. **2016,** 187, 134-142. https://doi.org/10.1016/j.electacta.2015.11.055.

[16] Cappetto, A., Cao, W. J., Luo, J. F., Hagen, M., Adams, D., Shelikeri, A., Xu, K., Zheng, J. P., J. Power Sources. **2017,** 359, 205-214. https://doi.org/10.1016/j.jpowsour.2017.05.071.

[17] Schweigart,P., Eleri, O. E., Nylund, I. E., Lai, S. Y., Lou, F., Svensson, A. M., Batteries & Supercaps **2023**, 6, e202300226 (1 of 15). https://doi.org/10.1002/batt.202300226.

[18] Melchiorre, M., Teoh, K. S., Gómez Urbano, J. L., Ruffo, F., Balducci, A., Green Chem. **2025,** 27, 5040–5050. https://doi.org/10.1039/D4GC05476H.

[19] Xu, K., Chem. Rev. **2004**, 104, 10, 4303-4418. https://doi.org/10.1021/cr030203g.

[20] Dong, Q., Guo, F., Cheng, Z., Mao, Y., Huang, R., Li, F., Dong, H., Zhang, Q., Li, W., Chen, H., Luo, Z., Shen, Y., Wu, Z., Chen, L., ACS Appl. Energy Mater. **2020**, 3, 695-704. http://dx.doi.org/10.1021/acsaem.9b01894.

[21] Song, G., Yi, Z., Su, F., Xie, L., Chen, C., ACS Appl. Mater. Interfaces **2021**,13, 40042-40052. https://doi.org/10.1021/acsami.1c09667.

[22] Xia, L., Lee, S., Jiang, Y., Xia, Y., Chen, G. Z., Liu, Z., ACS Omega **2017**, 2, 8741-8750. http://dx.doi.org/10.1021/acsomega.7b01196.

[23] Jamal, A., Salian, G. D., Mathew, A., Wahyudi, W., Carvalho, R. P., Gond, R., Heiskanen, S. K., Brandell, D., Younesi. R., ChemElectroChem 2023, 10, e202300139. https://doi.org/10.1002/celc.202300139.

[24] Jurng, S., Brown, Z. L., Kim, J., Lucht, B. L., Energy Environ. Sci., **2018**, 11, 2600-2608. https://doi.org/10.1039/C8EE00364E.

[25] Simon, P., Gogotsi, Y., Nature Materials, **2008, 7**, 845-854. https://doi.org/10.1038/nmat2297.

[26] Béguin, F., Presser, V., Balducci, A., Frackowiak, E., Adv. Mater. 2014, 26, 2219-2251. 10.1002/adma.201304137.

[27] Orbay, M., Teoh, K. S., Melchiorre, M., Neumann, C., Ruffo, F., Turchanin, A., Balducci, A., Gómez Urbano, J. L., ChemSusChem, **2025**, 18, e202501134 (1 of 9). 10.1002/cssc.202501134

Appendix

Publications

I. Ragazzini, I., Gualandi I., D'Altri, G., Di Matteo, V., **Yeasmin, L**., Cassani, M. C., Scavetta, E., Bernardi, E., Ballarin, B., Polyaniline/poly (2- acrylamido-2-methyl-1- propanesulfonic acid) modified cellulose as promising material for sensors design, Carbohydrate Polymers, 2023, 316, 121079. DOI: https://doi.org/10.1016/j.carbpol.2023.121079.

II. D'Altri, G., **Yeasmin, L**., Di Matteo, V., Scurti, S., Giovagnoli, A., Di Filippo, M. F., Gualandi, I., Cassani, M. C., Caretti, D., Panzavolta, S., Scavetta, E., Rea, M., Ballarin, B. Preparation and characterization of self-healing PVA–H2SO4 hydrogel for flexible energy storage, ACS Omega 2024 9 (6), 6391-6402. DOI: https://doi.org/10.1021/acsomega.3c05392.

III. Giovagnoli, A., D'Altri, G., **Yeasmin, L**., Di Matteo, V., Scurti, S., Di Filippo, M. F., Gualandi, I., Cassani, M. C., Caretti, D., Panzavolta, S., Focarete, M. L., Rea, M., Ballarin, B., Multi-Layer PVA-PANI conductive hydrogel for symmetrical supercapacitors: preparation and characterization. Gels 2024, 10, 458. DOI: https://doi.org/10.3390/gels10070458.

IV. D'Altri G., Giovagnoli A., Di Matteo V., **Yeasmin L.,** Scurti, S., Gualandi, I., Cassani, M. C., Panzavolta, S., Rea, M., Caretti, D., Ballarin, B., The Influence of DMSO on PVA/PVDF hydrogel properties: from materials to sensor application, *Gels* **2025**, *11*(2), 133, DOI: https://doi.org/10.3390/gels11020133.

V. Yeasmin, L., Giovagnoli, A., Di Matteo, V., Scurti, S., Cassania, M. C., Panzavolta, S., Munir, A., Ragazzini, I., and Ballarin, B., Covalently linked Poplar and Ayous lignin-based hydrogels: sustainable materials for water remediation, ACS OMEGA, 2026 (Manuscript accepted).

VI. D'Altri G., Di Matteo V., Yeasmin, L., Giovagnoli, A., Scurti, S., Gualandi, I., Caretti, D., ., Cassania, M. C., Ballarin, B., PVA-Based Hydrogels with Engineered Surface Roughness for Triboelectric Wearable Sensors, IEEE Sensors Journal 2025, DOI: https://doi.org/10.1109/jsen.2025.3636267.

Laboratory tutor and correlator

I. Laboratory tutor and co-relator of a Master's degree thesis "Corso di Laurea Magistrale" student Angelica Giovagnoli.

II. Laboratory tutor and co-relator of a Master's degree thesis "LOCATE co UNIBO" student Hafsa Munawar.

III. Laboratory tutor and co-relator of Bachelor degree thesis "Corso di Laurea in Scienze Ambientali" Campus Ravenna (UNIBO) student Samuele Marsico.

Summer school and conferences

I. Presented poster at **SUPERCAP** workshop titled *'PVA/H2SO4 hydrogels for all-in-one flexible and wearable supercapacitor: preparation and characterizations'* from 19-20 April 2023 at Bologna, Italy.

II. Summer School of ElectroCatalysis "**ElCats2023**" from 10 to 15 September 2023 at Trento, Italy.

III. Presented our research as oral presentation at **37th ISE Tropical Meeting** titled *'PVA_H2SO4 Hydrogel for wearable devices'* from 9 to 12 June 2024 at Stresa, Italy.

IV. Presented poster at **IUPAC POLYSOLVAT 15** Conference titled '*PVA_H2SO4 Hydrogel for wearable devices'* from 2 to 4 December 2024 at Kolkata, India.

V. Presented poster titled '*Lithium-ion Capacitor with Enhanced sustainability through the implementation of a Lactic acid-derived solvent and a conductive salt with reduced fluorine content'* at **ISE 76th annual meeting** from 7 to 12 September 2025 at Mainz, Germany.

VI. Presented poster titled '*Lithium-ion Capacitor with Enhanced sustainability through the implementation of a Lactic acid-derived solvent and a conductive salt with reduced fluorine content*' at workshop **SPOKE-1** on 29 September 2025 at Bologna, Italy.

Soft skill courses (40h)

I. Create-Protect-Innovate: Bringing ideas to market
II. Design Thinking, Processes and Methods
III. Research integrity
IV. Thinking out of the box
V. Time management

Hard skill courses (175h)

I. SUPERCAP Workshop
II. Sustainable Chemistry
III. ElectroCatalysis
IV. Nano and Molecular Electronics
V. Course on polymer chemistry
VI. Global Bio-geocheical Cycles

Short acronyms

PVA: Polyvinyl alcohol

PANI: Polyaniline

PAMPSA: Poly 2-acrylamido-2-methyl-1 propanesulfonic acid

Cell/PANI_PAMPSA: Cellulose/polyaniline-poly (2-acrylamido-2-methyl-1 propanesulfonic acid)

HySC: Hydrogel based supercapacitor

AC: Activated carbon

PTFE: Polytetrafluoroethylene

PEO: Poly (ethylene oxide)

TEGDME: Tetra ethylene glycol dimethyl ether

LiTFSI: Lithium bis(trifluoromethanesulphonyl)imide

LFP: Lithium iron phosphate

PYR: 1-butyl-1-methylpyrrolidium bis (trifluoromethanesulfonyl)-imidi

TTH: Organic redox active molecule from University of Bari

LIC: Lithium-ion capacitors

LIB: Lithium ion battery

EDLC: Electric double-layer capacitor

SC: Supercapacitor

LIDFOB: Lithium difluoro(oxalato)borate

LAHH: 5-methyl 1,3-dioxolane-4-one

PC: Propylene carbonate

List of schemes

List of figures

List of tables